Search for Relativistic Magnetic Monopoles
with the AMANDA detector

D I S S E R T A T I O N

zur Erlangung des akademischen Grades
doctor rerum naturalium
(dr. rer. nat.)
im Fach Physik

eingereicht an der
Mathematisch-Naturwissenschaftlichen Fakultät I
Humboldt-Universität zu Berlin

von
Herrn Dipl.-Phys. Peter Nießen
geboren am 09.08.1968 in Neuss

Präsident der Humboldt-Universität zu Berlin:
Prof. Dr. Jürgen Mlynek

Dekan der Mathematisch-Naturwissenschaftlichen Fakultät I:
Prof. Dr. Bernhard Ronacher

Gutachter:

1. Prof. Dr. Thomas Hebbeker
2. Prof. Dr. Michael Müller-Preußker
3. Prof. Dr. Paul Buford Price

eingereicht am: 24. November 2000
Tag der mündlichen Prüfung: 26. Februar 2001

Abstract

This thesis describes the search for relativistic magnetic monopoles with the AMANDA detector. The methods of their simulation and their separation from the background are given. No tracks with the signature of a magnetic monopoles are found, resulting in an upper limit on the flux of $0.61 \times 10^{-16}\mathrm{cm}^{-2}\mathrm{sr}^{-1}\mathrm{s}^{-1}$ for monopoles with velocities close to the speed of light. This is better by a factor of 3-4 compared to results from other underground detectors and a factor of 16 below the limit derived from the observed stability of the galactic magnetic fields.

Zusammenfassung

Diese Arbeit beschreibt die Suche nach relativistischen magnetischen Monopolen mit dem AMANDA Detektor.

Paul Dirac hat als erster magnetische Ladungen in die Maxwellgleichungen eingeführt und mit Hilfe eines Quantisierungsansatzes gezeigt, daß die magnetische Ladung μ ein ganzzahliges Vielfaches von $\frac{1}{2\alpha}e \approx (137/2)e$ beträgt. Er erklärte die Nichtexistenz von isolierten magnetischen Ladungen dadurch, daß die Anziehungskraft zwischen einem Nord- und Südpol fast 4700 mal so stark ist wie zwischen zwei entgegengesetzt geladenen elektrischen Teilchen.

Das Interesse für Monopole flammte erst 1974 mit der Formulierung der großen vereinheitlichten Theorien (engl. Grand Unified Theories oder GUTs) auf, als Gerard t'Hooft zeigen konnte, daß immer dann, wenn eine Eichgruppe durch spontane Symmetriebrechung u. a. in eine $U(1)$ Untergruppe zerfällt, in dieser Theorie magnetische Monopole existieren. Weiterhin konnte er angeben, daß die Monopolmasse m_{MP} von der Größenordnung $m_{\mathrm{MP}} \approx \Lambda/\alpha$ ist, wobei Λ die Energieskala der Vereinigung beschreibt. Im einfachsten Fall einer $SU(5)$ Eichgruppe ergibt sich für die Monopolmasse dann $m_{\mathrm{MP}} = 10^{17}$ GeV.

Die Suche nach Monopolen erfolgt hier mit dem AMANDA Detektor. AMANDA steht für Antarctic Muon And Neutrino Detector Array und ist ein Neutrino Čerenkov Teleskop. Es befindet sich in unmittelbarer Nähe des geographischen Südpols. Die primäre Aufgabe ist die Suche nach kosmischen Neutrinoquellen aus deren Studium man sich Erkenntnisse über die Beschleunigungsmechanismen kosmischer Strahler erhofft. Dabei wird ausgenutzt, daß hochenergetische Neutrinos, deren Flugbahn in der Nähe des Detektors vorbeiführt, sich (mit einer wenn auch geringen Wahrscheinlichkeit) in einer geladenen schwachen Wechselwirkung in Myonen umwandeln. Die Myonen wiederum erzeugen im antarktischen Eispanzer mittels des Čerenkoveffektes Licht, das mit einer Anordnung von Photovervielfachern nachgewiesen wird.

Ein Monopol sendet ebenfalls Čerenkovlicht aus, allerdings ist wegen der magnetischen Ladung die Lichtemission bis zu 8300 mal höher als für mimimal ionisierende elektrisch geladene Teilchen. Diese Eigenschaft dient zum Nachweis der Monopole.

Die zur Erzeugung des Čerenkovlichts in Eis oder Wasser nötige Geschwindigkeit des Monopols von $\beta = v/c > 0.75$ kann gemäß aktuellen Beschleunigungsmodellen erreicht werden, falls die Monopolmasse sich in der Gegend von 10^{11} GeV bewegt. Hierzu existieren ebenfalls teilchenphysikalische Modelle, die diesen Wert vorhersagen.

Um die Reaktion des Detektors beim Passieren von Monopolen zu untersuchen, wurde die Simulationssoftware, die nur Teilchen beschreibt, die sich mit Lichtgeschwindigkeit bewegen, entsprechend erweitert. Es wurde getestet, wie groß die Fläche sein muß, auf der Monopole generiert und zum Detektor geschickt werden. Die Winkelabhängigkeit der Detektorsensitivität wurde ebenfalls betrachtet.

Es kann vorkommen, daß Multi-Myonen-Bündel, die in atmosphärischen Wechselwirkungen aus der kosmischen Strahlung entstehen, ein Signalmuster bewirken, das dem von Monopolen vergleichbar ist. Da Myonen jedoch eine Reichweite von höchstens einigen Kilometern Wasseräquivalent haben, nutzt man die Erde als Abschirmung und sucht nach Spuren, die von unten in den Detektor eintreten.

Dazu wird ein Verfahren benötigt, das aus den von den Photomultipliern gemessenen Zeiten eine Richtungsinformation errechnet. Eine solche Rekonstruktion wurde auf die experimentellen Daten, die Simulation des atmosphärischen Hintergrunds und das erwartete simulierte Monopolsignal angewendet. Vorher müssen jedoch diejenigen Treffer im Detektor entfernt werden, die nicht von Spuren erzeugt worden sind oder die von stark gestreutem Licht stammen. Dazu wurden unter anderem die Signalamplituden der Photovervielfacher studiert. Vorhergehende Untersuchungen hatten ergeben, daß die vom Photomultiplier gemessene Lichtmenge nicht mit der tatsächlich eingetroffenen Anzahl Photonen übereinstimmt. Deshalb wurden die Kalibration der Sensoren in der durch die Messdaten nahegelegten Weise variiert, um Übereinstimmung zwischen Simulation und Experiment zu erzielen. Die Abhängigkeit des Resultats von der Art der Kalibration ist jedoch unbedeutend.

Trotz dieser Aufbereitung der Detektordaten für die Rekonstruktion ergibt sich jedoch ein gewisser Anteil von Fehlrekonstruktionen, d.h. Spuren, die von oben in den Detektor eindringen, aber als von unten kommend rekonstruiert werden. Um diese Falschereignisse zu verwerfen, werden Qualitätskriterien untersucht. Das sind aus Zeitverhalten und Signalmuster gewonnene Observablen, wie z.B. die Anzahl der getroffenen Kanäle.

Um schließlich eine Auswahl an Ereignissen zu finden, die nur die gewünschten Signalereignisse enthält, wurden Schnitte auf ausgewählte Observablen angewandt. Diese Schnitte wurden auf einer kleinen Anzahl Ereignisse entwickelt. Um die Mächtigkeit dieser Schnitte in bezug auf die Zurückweisung von Falschereignissen vorherzusagen, wurde mittels eines neuronalen Netzes eine Prozedur definiert, die die Anzahl der Falschereignisse als Funktion der Schnittparameter vorhersagt. Dies war nötig, da die Beschreibung der ausgewählten Observablen durch die Simulation nicht immer genau genug war. Die Vorhersage der Ereignisanzahl durch das neuronale Netz wurde durch Anwendung der aus einer geringen Datenmenge gewonnenen Funktion auf die sechsfache Datenmenge überprüft.

Nach Anwendung aller Schnitte auf die gesamte zur Verfügung stehende Datenmenge des Jahre 1997 wurden 3 Ereignisse gefunden. Diese konnten jedoch als elektronische Artefakte identifiziert werden. Damit verblieb kein Ereignis in der Analyse.

Das Ergebnis wurde deshalb durch eine obere Flußgrenze ausgedrückt. Es ergibt sich ein maximaler Fluß von $0.61 \times 10^{-16} \mathrm{cm}^{-2}\mathrm{sr}^{-1}\mathrm{s}^{-1}$ für Monopole, die den Detektor mit Lichtgeschwindigkeit passieren. Dieser Fluß liegt um einen Faktor 16 unterhalb der sogenannten Parkergrenze, die aus dem Energieentzug des galaktischen Magnetfeldes durch Monopole abgeleitet wird und um einen Faktor 3-4 unter den Flüssen, die gegenwärtig

von anderen Experimenten für relativistische Monopole angegeben werden.

Contents

List of Figures

List of Tables

Chapter 1

Introduction

The subject of this thesis is the search for magnetic monopoles. Electric monopoles are part of our daily life and show up e.g. as the unit charge of the electron and the proton. Opposed to these particles, indications for magnetic monopoles have only been found once in an unconfirmed experiment [Cabrera, 1982].

The existence of magnetic monopoles would establish symmetry between the electric and magnetic part of the Maxwell equations. Restoring this symmetry and using quantum mechanical principles, Dirac was able to determine the quantity of the magnetic charge and at the same time to show that the quantisation of electric charge is connected to the existence of magnetic charges. He found that the magnetic charge is $1/(2\alpha) \approx 68.5$ times that of the electric charge in Gaussian units (α is the electromagnetic coupling constant).

Monopoles have been searched for for a long time - in underground experiments, at accelerators or using ancient Mica. All these searches had negative results and the interest in the subject died down. Monopoles became interesting again when, in 1974, it could be shown that monopoles are ingredients of Grand Unified Theories (GUT) in conjunction with a phase transition in the early Universe.

The monopole abundance is limited by the fact that a) the monopole mass density must not overclose the universe and b) that monopoles cannot short-circuit the cosmic magnetic fields beyond their current strength. Condition (b) is stronger than (a) and puts an upper limit on the monopole flux of about $10^{-15} \text{cm}^{-2}\text{s}^{-1}\text{sr}^{-1}$. Present limits obtained by the underground experiments MACRO, Orito and Baksan reach down to $2.5 \times 10^{-16} \text{cm}^{-2}\text{s}^{-1}\text{sr}^{-1}$. The methods used will be described in more detail in chapter 2.

The amount of Cherenkov radiation from monopoles in ice/water would exceed that of single charged electrical particles by a factor of 8300, see chapter 2. This fact makes it promising to perform a search with under-water/under-ice detectors.

The detector used here is the AMANDA telescope. AMANDA is a joint American-European project to build a neutrino telescope at the geographical South Pole, which started with feasibility studies in 1992. Complementary to the astronomy performed with other telescopes so far, i.e. the observation of photons and charged particles, it is able to detect high energy neutrinos (> 100 GeV) and will open a new window to the skies.

This thesis consists of the following parts: In chapter 2, the theory and possible detection mechanisms of monopoles will be discussed in detail. Since AMANDA's principal goal is neutrino detection, a short overview of the mechanisms involved will be introduced in chapter 3. It will be followed by a description of the AMANDA detector in chapter 4. The next chapters 5, 6 and 7 deal with the data processing chain. This includes the simulation of monopole events, the calibration of the detector and the reconstruction of tracks. This will be made use of in chapter 8, where a monopole flux limit will be derived. The results will be summarised in chapter 9 and an outlook to possible future development will be given. The appendices deal with properties of the ice at the South Pole, neural networks, some considerations on detector dead time and the technicalities of the analysis.

Chapter 2

Magnetic monopoles

2.1   A brief history of magnetism

Since magnetism was discovered in the early ages, probably by Chinese scientists around the 26th century BC, magnetic charges have been observed only in pairs as dipoles. In fact, the word "pole" was first mentioned by the medieval crusader and engineer Petrus Peregrinus de Maricourt, in his "Epistola de Magnete"in 1296. He placed a thin iron sheet on a lump of magnetite and marked the lines along which it oriented itself. Then he observed that these lines would intersect each other at 2 points he called "poles"[EB1, 1991]. Ever since, these poles have been observed only in pairs and never isolated. This is manifest in Maxwell's equations, where there are no terms for a magnetic charge and current:

$$\nabla \cdot \vec{E} = 4\pi \rho_e \tag{2.1}$$

$$\nabla \cdot \vec{B} = 0 \tag{2.2}$$

$$\nabla \times \vec{B} - \frac{1}{c}\frac{\partial \vec{E}}{\partial t} = \frac{4\pi}{c}\vec{j}_e \tag{2.3}$$

$$-\nabla \times \vec{E} - \frac{1}{c}\frac{\partial \vec{B}}{\partial t} = 0 \tag{2.4}$$

However, there is no theoretical necessity for these quantities to vanish and one might substitute

$$\nabla \cdot \vec{B} = 4\pi \rho_m \tag{2.5}$$

$$-\nabla \times \vec{E} - \frac{1}{c}\frac{\partial \vec{B}}{\partial t} = \frac{4\pi}{c}\vec{j}_m \tag{2.6}$$

3

2.2 The Dirac monopole

Inserting magnetic charge and current terms into the Maxwellian equations does not give the magnitude of these quantities. Nor does it tell whether some quantisation is to be expected. By considering quantum mechanical wave functions, Dirac was able to derive a basic unit of magnetic charge [Dirac, 1931]. He noted that the phases of wave functions ψ_n are arbitrary, only the phase difference in two different space points is of physical relevance. Even more general, the phase need not be integrable, i.e. going from one point to another using different paths yields different shifts in the phase. All that needs to be fulfilled is that the observable quantities, such as probability amplitudes like

$$\int \mathrm{d}^3x \, \phi_m^\dagger \psi_n \tag{2.7}$$

are well defined. In order to achieve this, the phases should cancel in the above expression and since this has to be true for all wave functions, the change in phase around a closed loop has to be the same for all wave functions.

If the wave function is represented as $\psi = \psi_1 e^{i\beta}$ where an arbitrary phase β is separated from the rest of the wave function ψ_1, the change in phase around a closed loop is given by a line integral along the derivatives of β.

$$\int \mathrm{d}\vec{s} \, \vec{\kappa} \tag{2.8}$$

where the four-vector $\kappa_\mu = \partial_\mu \beta = (\kappa_t, \vec{\kappa})$ and $\mathrm{d}\vec{s}$ is the 3-dimensional line element of the loop. Because the integral is required to have the same values for all wave functions, the derivative κ must be definite.

Regarding the derivatives appearing in the Dirac equation $((i\hbar\gamma_\mu\partial^\mu - m)\psi = 0)$ one sees that

$$-i\hbar\partial_\mu\psi = e^{i\beta} \left(-i\hbar\partial_\mu + \hbar\kappa_\mu \right) \psi_1. \tag{2.9}$$

If ψ satisfies a wave equation involving the energy and momentum operators $\vec{P} = -i\hbar\nabla$ and $\mathbf{E} = i\hbar\partial/\partial t$, then the same wave equation will be fulfilled by ψ_1 if the operators are replaced by $\vec{P} + \hbar\vec{\kappa}$ and $\mathbf{E} - \hbar\kappa_t$ respectively. If ψ describes a free particle, ψ_1 describes a particle with charge e in an electromagnetic field given by the potentials $\vec{A} = \hbar c/e \cdot \vec{\kappa}$, $\phi = -\hbar/e\kappa_t$. Thus the non-integrability of the phases has gained a physical meaning.

Some new notion comes in by observing that the phase does not change when adding an integral multiple of 2π, and the change in phase around a closed loop may differ by this amount. Consider a small loop along which the wave function is evaluated. Since the wave equation requires the wave function to be steady, the change in phase has to be small as well and cannot be a multiple of 2π. However, when a wave function vanishes, there is a different situation, since then the phase has no meaning. Since the wave function is complex, it takes two separate conditions (for the real and the imaginary part) to be fulfilled, hence the wave function vanishes along a line, called "nodal line". If such a nodal

line passes through the small loop, the loop cannot be contracted to be arbitrarily small and considerations of continuity no longer hold. The change in phase is now

$$2\pi n + \int \mathrm{d}\vec{s}\,\vec{\kappa} \tag{2.10}$$

$$= 2\pi n + \int \mathrm{d}\vec{S}\,\nabla \times \vec{\kappa} \tag{2.11}$$

$$= 2\pi n + e/\hbar c \cdot \int \mathrm{d}\vec{S}\,\vec{B} \tag{2.12}$$

where Stoke's integral theorem was applied and $\vec{B} = \nabla \times \vec{A}$ is the magnetic field. $\mathrm{d}\vec{S} = (\mathrm{d}y\mathrm{d}z, \mathrm{d}x\mathrm{d}z, \mathrm{d}x\mathrm{d}y)$ is the vector of area elements. The integer n is a characteristic of the nodal line. A large surface is composed of many small surfaces, thus the change in phase will become

$$2\pi \sum n + e/\hbar c \cdot \int \mathrm{d}\vec{S}\,\vec{B} \tag{2.13}$$

where the integration is taken over the whole surface and the summation is over all nodal lines passing through. Expression 2.13 gives the change in phase around a closed loop bordering a surface. The expression then vanishes if the surface has no border, e.g. in the case of a sphere. Thus, the sum $\sum n$ taken over all nodal lines crossing the surface must be equal to $-e/2\pi\hbar c$ times the total magnetic flux penetrating the surface. $\sum n$ will not vanish if the nodal lines end in the volume enclosed by the surface. Lines entering and exiting the volume will contribute equal and opposite signed values and will not appear in the net result. The total magnetic flux crossing the surface is thus

$$4\pi\mu = 2\pi N\hbar c/e \tag{2.14}$$

where N is the sum of the characteristics of nodal lines ending in the volume. At the endpoint of the nodal lines there is then a magnetic pole with strength

$$\mu = 1/2N\frac{1}{\alpha}e \tag{2.15}$$

where $\alpha = e^2/\hbar c \approx 1/137$. This means that the magnetic charge is quantised.

Finally, in the conclusion of his paper Dirac notes that the formalism of quantum mechanics does not require a change in the case monopoles exist and "one would be surprised if Nature had made no use of it". As an explanation for the non-observation of such objects he noted that the attractive force between a monopole and an anti-monopole would be 4700 times that of the force between proton and electron, and thus monopoles have never been observed separated.

The numerically large charge of a monopole has important consequences for the detection mechanism used in water/ice Cherenkov telescopes. As ionisation losses are proportional to the square of the charge (Bethe-Bloch formula), the interaction will be increased by $1/(2\alpha)^2 \approx 4700$. When calculating the Poynting flux from a monopole passing through a medium with refractive index n, it is seen that the Cherenkov radiation is enhanced

6

by a factor of $(\mu/e \cdot n)^2$ [Tompkins, 1965, Kolokolov et al., 1999]. This will result in a light yield increased by approximately 8300 compared to a minimal ionising muon if a refractive index $n = 1.33$ of the medium (water, ice) is assumed.

2.3   The 't Hooft/Polyakov monopole

While quantum mechanics can be used to predict the charge of the magnetic monopole, statements about its mass are not possible within this framework. This is only possible within the context of Grand Unified Theories (GUTs). It was shown ['tHooft, 1974, Polyakov, 1974] that in all those gauge theories in which the electromagnetic group $U(1)$ is taken to be a subgroup of a larger group with a compact covering group, such as $SU(3)$, genuine magnetic monopoles can be created as regular solutions of the field equations. In this scenario, the monopole enters within the framework of the Higgs-Kibble mechanism as a particle bearing a charge of a Dirac monopole and is assigned a mass m_{MP} connected to the grand unification scale Λ by

$$m_{\mathrm{MP}} = \Lambda/\alpha. \qquad (2.16)$$

The masses predicted for monopoles vary over several orders of magnitude, depending on the model. A lower limit is given by requiring Λ to be at least of the order of the electroweak unification at 250 GeV, leading to a monopole mass of 4×10^4 GeV. A value of $m_{\mathrm{MP}} = 10^{17}$ GeV is obtained from an $SU(5)$ model GUT scale of $\Lambda = 10^{15}$ GeV. Other possibilities inspired by superstrings give masses of 10^{16} GeV [Lazarides et al., 1987]. A more phenomenological approach is given by [Kephart and Weiler, 1996, Weiler and Kephart, 1996] using the so called Parker limit (see below) resulting in a mass of 10^{11} GeV. Other symmetry groups like $SU(15)$ lead to masses of 10^8 GeV. A mass of 10^9 GeV is obtained from lowering the unification scale in a modified $SU(5)$ model [Kephart and Weiler, 1996].

A schematic drawing of a GUT monopole is shown in figure 2.1. In the innermost region up to 10^{-29} cm, the full GUT symmetry is conserved, indicated by the corresponding GUT X boson. It can induce transitions between the different flavours of quarks and leptons. This property gives rise to nucleon decay. The outer layers reflect the transition to the electroweak phase. The outer layer consists of fermion-anti fermion pairs [Boerner, 1988]. These play a role in enhancing the nucleon catalysis cross section in processes like e.g. $p + M \rightarrow M + e^+ \pi^0$.

2.4   Generation of monopoles in the early universe

Objects with masses of the order just mentioned can only be created in the early universe and not in today's particle accelerators. After a phase transition, monopoles are created in large abundance. It can be shown that annihilation of monopole-antimonopole pairs is
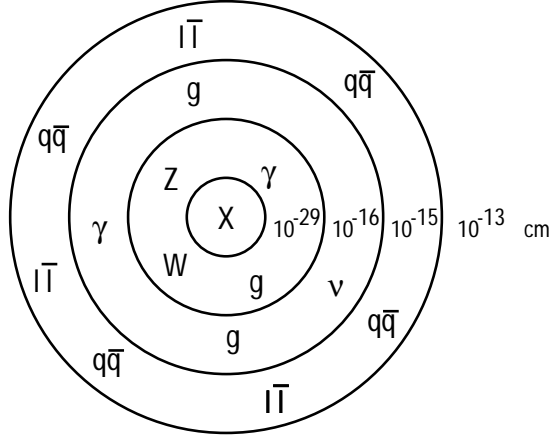
Figure 2.1: Possible structure of a GUT monopole, according to [Boerner, 1988].

negligible [Preskill, 1979]. The resulting monopole density in our epoch is then given by

$$n_{\mathrm{MP}} \sim 10^{-7} \times \left(\frac{\Lambda}{10^{15}\,\mathrm{GeV}}\right)^3 \times \left(\frac{l_H}{\xi_c}\right)^3 \mathrm{cm}^{-3} \qquad (2.17)$$

[Kibble, 1980]. The quantity l_H is the horizon size, i.e. the maximum distance a particle can travel since the big bang. The correlation length ξ_c is the maximum distance over which the Higgs field can be correlated, which cannot be bigger than the horizon size. The ratio l_H/ξ_c at the time of phase transition thus is ≥ 1. This leads to a mass density relative to the closure value of the universe of

$$\Omega_m \sim 10^{15} \times \left(\frac{m_{\mathrm{MP}}}{10^{17}\,\mathrm{GeV}}\right) \times \left(\frac{\Lambda}{10^{15}\,\mathrm{GeV}}\right)^3 \times \left(\frac{l_H}{\xi_c}\right)^3 \mathrm{cm}^{-3} \qquad (2.18)$$

which over-closes the universe by 15 orders of magnitude. This difficulty can be solved by assuming an inflationary phase in the early universe [Guth and Weinberg, 1983] or the temporary breaking of the $U(1)$ group to allow for the creation of strings which connect the monopoles and anti-monopoles leading to their annihilation [Langacker and Pi, 1980].

Other constraints on the monopole flux arise from the fact that the monopole density must not be so high that the magnetic fields in the universe collapse faster than they can be regenerated by their dynamo mechanisms. This flux, called Parker limit, was calculated to be $\Phi_{\mathrm{Parker}} \leq 10^{-15}\mathrm{cm}^{-2}\mathrm{sr}^{-1}\mathrm{s}^{-1}$ [Turner et al., 1982]. The isotropic monopole flux can be calculated from equation 2.17:

$$\Phi_{\mathrm{MP}} = \frac{c \times n_{\mathrm{MP}}}{4\pi} \sim 10^{-4} \times \left(\frac{m_{\mathrm{MP}}}{10^{15}\,\mathrm{GeV}}\right)^3 \times \left(\frac{l_H}{\xi_c}\right)^3 \mathrm{cm}^{-2}\mathrm{sr}^{-1}\mathrm{s}^{-1}. \qquad (2.19)$$

Comparison with Φ_{Parker}, assuming that $M_{\mathrm{MP}} = \Lambda/\alpha$, yields an upper mass limit of

$$m_{\mathrm{MP}} \leq 10^{11}(\xi_c/l_h)\mathrm{GeV}. \qquad (2.20)$$

8

Accelerator	B/μG	L/Mpc	μBL/GeV	Ref.
normal galaxies	3-10	10^{-2}	$(0.3-1)\times 10^{12}$	1.
star-burst galaxies	10-50	10^{-3}	$(1.7-8)\times 10^{11}$	2.
AGN jets	~ 100	$10^{-4}-10^{-2}$	$1.7\times(10^{11}-10^{13})$	3.
galaxy clusters	2-30	$10^{-4}-1$	$3\times 10^{9}-5\times 10^{16}$	4.
extragal. sheets	0.1-1	1-30	$1.7\times 10^{13}-5\times 10^{14}$	5.

Table 2.1: Monopole kinetic energy achieved by different acceleration sources. References: 1. [Beck, 1996], 2. [Kronberg et al., 1981], 3. [Kellermann and Pauliny-Toth, 1981], 4. [Enßlin et al., 1997], 5. [Ryu et al., 1998].

$E_{\max}/m_{\mathrm{MP}}$	$\beta_{\max}$
0.1	0.417
1.0	0.866
10.0	0.996

Table 2.2: Achievable speeds ($\beta_{\max}$) for different energy to mass ratios.

2.5 Relativistic monopoles

The AMANDA telescope detects particles by their Cherenkov light. Monopoles have to move faster than light in the ice medium in order to emit Cherenkov radiation. The speed of light c_n in a medium whose refractive index is n is related to the vacuum light speed c by $c_n = c/n$; thus the speed of the particle β has to be greater than c_n. For ice with a refractive index of $n = 1.33$ this means $\beta \geq c_n = c/1.33 = 0.75$ (c is set to 1). Just like electrically charged particles are accelerated along the electric field lines, the monopoles are accelerated along the magnetic field lines of cosmic objects. The maximum kinetic energy $E_{\max}$ of a monopole which travels over a distance L in a field of strength B is given by

$$E_{\max} = N \times 6 \times 10^{10}\text{GeV} \times \left(\frac{B}{3\mu\text{G}}\right) \times \left(\frac{L}{300\text{pc}}\right) \tag{2.21}$$

where N is the monopole charge in units of $\mu = \frac{e}{2\alpha}$. The maximum achievable speed resulting from this energy is mass dependent and given by

$$\beta = \frac{p}{E} = \sqrt{1 - \left(1 + \frac{E_{\max}}{m_{\mathrm{MP}}}\right)^{-2}}. \tag{2.22}$$

Thus, monopoles with a mass up to 10^{15-16} GeV can be accelerated to relativistic speeds given the scenarios in table 2.1. Table 2.2 shows the achievable speeds given by equation 2.22 for different ratios of $E_{\max}/m_{\mathrm{MP}}$, where $E_{\max} = \mu BL$.

The idea of relativistic monopoles has also been supported by lack of other explanations for very high energy cosmic rays [Kephart and Weiler, 1996]. Protons at these energies are decelerated by scattering off the 3K cosmic background radiation and produce $\Delta^\star$ resonances, which decay into nucleons and pions. This mechanism is called GZK cut-off [Greisen, 1966, Zatsepin and Kuzmin, 1966] and limits the energy of the protons to 5×10^{19} eV, resulting in a mean free path length of about 6 Mpc, which means that these protons should come from a nearby source or have an energy far above 10^{20}eV. Nevertheless, no (local) sources of protons have been identified, and mechanisms accelerating protons above 10^{17} eV are speculative [Elbert and Sommers, 1995, Sigl et al., 1994].

Monte Carlo studies comparing proton primaries and heavy nuclei primaries to the 3×10^{20}eV Fly's Eye's experiment's event tend to favour heavy nuclei. But since the energy in the frame of the nucleus in that region is close to the nuclear binding energy of 7MeV/nucleon, the nucleus will be photo-dissociated by the 3K photon background. Additionally, it was found by the Fly's Eye collaboration that above 10^{18}eV the fraction of protons increases and the fraction of heavy nuclei decreases [Gaisser et al., 1993].

Once again, comparing the Fly's Eye events with Monte Carlo, it was found that the time development in the detector is not in agreement with a high energy gamma-ray primary, since the gamma-induced shower peaks low in the atmosphere [Halzen, 1999]. A similar argument applies also to a neutrino as primary. The Fly's Eye event occurs high up in the atmosphere, but the expected rate for high altitude events originating from neutrinos is lower than that observed by six orders of magnitude. There is also the problem of how to obtain the gammas and neutrinos, because they are thought to originate from the decay of 10^{20}eV pions.

In contrast, monopoles would not suffer energy losses from scattering with the 3K and diffuse photon background, since the scattering cross-section for monopoles is just that of classical Thompson scattering, $\sigma_{\mathrm{Thompson}} = 8\pi\alpha_{\mathrm{MP}}/3M^2 \approx 2 \times 10^{-43}(M/10^{10}\mathrm{GeV})\mathrm{cm}^2$. This is a value orders of magnitude below the pion photo-production cross-section which is responsible for the GZK cutoff.

2.6 Review of monopole search experiments

Many experiments have been searching for monopoles, either by observing the change in flux induced by a monopole passing through a super-conducting coil, detecting ionisation or Cherenkov light in a suitable medium. Whereas these experiments search for monopoles of cosmic origin, accelerator experiments have been performed also.

2.6.1 Induction experiments

This sort of experiment makes direct use of the magnetic charge. The magnetic flux of a monopole with single Dirac charge is given by $4\pi\mu = hc/e$. A super-conducting loop compares this flux with the elementary flux quantum $\phi_0 = hc/2e$, where the factor 2

arises from the electrons appearing as Cooper pairs. In fact, one monopole candidate was observed on February 14th, 1982 [Cabrera, 1982] with the apparatus sketched in figure 2.2.

The major background for these experiments are small changes in the Earth's magnetic field. A relative change of 10^{-11} will produce the same signal as a magnetic monopole. The shielding of the ambient field has to be done with some diligence, leading to high costs for detectors with large surveillance areas. One either searches for cosmic monopoles passing through the coil or passes materials thought to have accumulated monopoles, such as iron, mangane nodules and lunar rocks through the loops. However, apart from the single observation in 1982, all these searches have had negative results.

2.6.2   Ionisation experiments

The limitation in the area is overcome by ionisation experiments. Here effective areas of several 100 m^2 can be reached. As an example, the MACRO (Monopole Astrophysics and Cosmic Ray Observatory) experiment [Ahlen et al., 1993] shown in figure 2.3 will be discussed.

MACRO is located below the Gran Sasso mountain in central Italy and was built to search for massive monopoles (10^{17} GeV) in the velocity range of $10^{-4} < \beta < 10^{-3}$. The idea is to detect tracks of monopoles and to confirm the observation by measuring the speed of the candidate particle of its ionisation rate.

The detector consists of twelve so-called supermodules which are built in layers, see figure 2.3. On top, a liquid scintillator is sandwiched between two streamer chambers. Then, three alternating layers of concrete ($\sim$ 50 cm) and streamer chambers follow. Below the third of these layers, a layer of track etch material is installed (Lexan and CR-39). The track etch detector is followed by 4 layers of streamer chambers and concrete alternating. Below the last concrete layer, another sandwich of streamer and liquid scintillator is located.

Monopoles in the velocity range of $10^{-4} < \beta < 10^{-3}$ will not be detected by direct ionisation because the monopole speed is close to that of the orbiting electrons of the atoms in the detection material. One ingredient of the Bethe-Bloch formula, i.e. considering the orbiting electrons as resting and free, is not valid anymore; moreover, the effect of the magnetic field on the atomic levels has to be considered. Thus the so-called DKPMR mechanism [Drell et al., 1983] is used: the streamer chambers are run on a mixture of Helium and n-Pentan. A monopole which passes through the gas will perturb the energy levels in the Helium and excites it to 20 eV. This energy is passed onto the n-Pentan in collisions which will be ionised and start the streamer. This technique results in a very low energy threshold for the detection of monopoles, which will result in a detection efficiency which is almost independent of the monopole speed.

The track etch detector is composed of a layer of Lexan, aluminium foil and CR-39. After some exposure, the streamer tube data is searched for particles which move at $\beta = 10^{-4}$ and consequently need 150 μs to pass through the super module. This information is

Figure 2.2: Sketch of the Cabrera experiment [Groom, 1986]. The detecting spool is shielded from external magnetic fields by a mu-metal and a superconducting shield. The gauge spool is used to calibrate the detector sensitivity.

used to determine the position of the monopole in the track etching layer. The composition allows the distinction of slow and fast monopoles, because slow monopoles will only be registered in the CR-39, since Lexan needs a higher activation. Monopoles passing through

Figure 2.3: A cross section end view (not to scale) of the lower part of a MACRO super-module. The height is approximately 4.7 m. Taken from [Ahlen et al., 1993].

will damage molecular bounds, the amount of damage reflects the speed of the monopole and can be measured by the diameter of a hole which develops after the material is etched. Thus, also relativistic monopoles can be searched for, however, the speed measurement from this is very coarse, giving the order of magnitude only.

After some exposure time, the scintillator data is scanned for tracks which penetrated the detector with a speed between $10^{-4} < \beta < 10^{-3}$. Subsequently, the streamer chambers and the track etching layers are examined for confirmation of the events.

Another sort of ionisation experiment is the study of ancient (5×10^8 yr) mica [Price, 1984]. One searches for defects in the molecular structure of the material caused by the propagation of a monopole. The limits achieved reach down to $\Phi \leq 10^{-17} \text{cm}^{-2} \text{sr}^{-1} \text{s}^{-1}$ in the velocity range around $\beta = \mathcal{O}(10^{-4})$ [Price, 1984].

A compilation of results is shown in figure 2.4. It shows the limit obtained from the combination of induction experiments. As said above, these have only small detection areas and thus give the least restrictive limits. The SOUDAN detector, located below Soudan, Minnesota at 2100 m of water equivalent, is a fine-grained, tracking calorimeter primarily designed for nucleon decay [Thron et al., 1989]. To detect particles, drift tubes are used whose pulse durations are used to measure the deposited energy. The same principle is applied in the UCSD II array [Buckland et al., 1990]. Here however, the array is operated at sea level with no earth cover and rejection of cosmic-ray muons is performed electronically by measuring the speed of the passing particle.

The Orito experiment uses 2000 m² of track etching detector (CR-39), located in the Ohya stone quarries 100 km north of Tokyo [Orito et al., 1991]. The exposure extended between September 1986 and February 1990, after which the material was etched, but no monopoles were found.

The strong speed dependency of the track etch technique is due to the fact that the ionisation power of particles is strongly speed dependent. In case of the Orito experiment, the sensitivity of the material has been measured using heavy ion beams. In comparison, the drift tube technique using the mechanism described for the MACRO experiment above will result in small velocity dependence only, as there will be a detectable signal emitted by the tube no matter what the actual speed of the particle is.
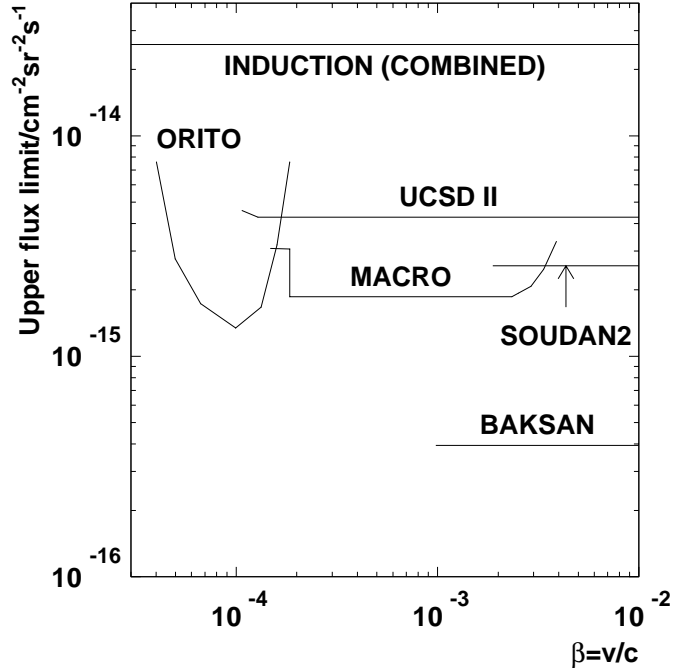
Figure 2.4: Compilation of monopole flux limits (90% C.L.) in 1994. Taken from [Hung, 1994].

2.6.3 Accelerator experiments

Present accelerators have beam energies of about 1 TeV. Thus, it is not possible to search for GUT monopoles. Nevertheless, searches are performed to set upper limits on cross sections and lower limits on monopole masses. The channels used are

$$
\begin{aligned}
e^+ + e^- &\rightarrow M + \bar{M} \\
p + p &\rightarrow M + \bar{M} \\
p + \bar{p} &\rightarrow M + \bar{M}
\end{aligned}
$$

or the production of virtual monopole loops [Abbott et al., 1998] which lead to the production of two photons in the final state (figure 2.5). Usually one tries to detect monopoles in the final state; this is done by looking for the defects a monopole will produce when traversing plastic material such as Lexan or CR-39 which is wrapped around the
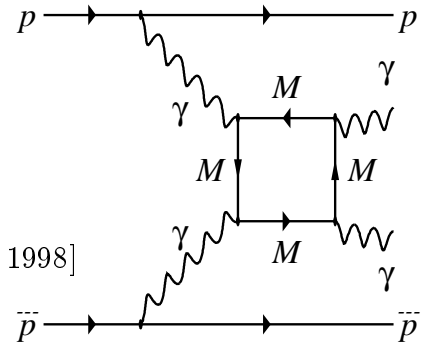
Figure 2.5: A virtual monopole loop in a $p\bar{p}$ reaction.

14

$\sigma_M[\text{cm}^2]$	$m_M[\text{GeV}]$	Beam	$\sqrt{s}[\text{GeV}]$	Events	Reference
$< 2 \cdot 10^{-35}$	> 1	p	6	0	[Bradner and Isbell, 1959]
$< 1 \cdot 10^{-35}$	> 3	p	28	0	[Fidecaro et al., 1961]
$< 2 \cdot 10^{-40}$	> 3	p	30	0	[Purcell et al., 1963]
$< 5 \cdot 10^{-42}$	> 13	p	400	0	[Carrigan Jr. et al., 1974]
$< 4 \cdot 10^{-38}$	> 10	e^+e^-	400	0	[Musset et al., 1983]
$< 3 \cdot 10^{-32}$	> 800	$p\bar{p}$	34	0	[Price et al., 1987]
$< 1 \cdot 10^{-38}$	> 17	e^+e^-	1800	0	[Braunschweig et al., 1988]
$< 1 \cdot 10^{-37}$	> 29	e^+e^-	$50 - 61$	0	[Kinoshota et al., 1989]
$< 2 \cdot 10^{-34}$	> 850	$p\bar{p}$	1800	0	[Bermon et al., 1990]
$< 7 \cdot 10^{-33}$	> 44.9	e^+e^-	$89 - 93$	0	[Kinoshota et al., 1992]
$< 3 \cdot 10^{-37}$	> 45	e^+e^-	$88 - 94$	0	[Pinfold et al., 1993]
$< 8 \cdot 10^{-38}$	$> 610 - 1850$	$p\bar{p}$	1000	0	[Abbott et al., 1998]

Table 2.3: Results from accelerator experiments.

interaction point and exposed for some time, typically a few months. Then the plastic is etched; the molecular bounds are broken along the monopole paths and little holes develop. These are searched for with a microscope. However, no monopoles have been observed so far, yielding the cross section limits given in table 2.3.

2.7 Monopole detection with Water/Ice Cherenkov telescopes

Under-water/-ice Cherenkov telescopes offer several possibilities to detect monopoles. In water or ice light is emitted from processes stimulated by monopoles: Cherenkov light emission, δ-ray production, radio luminescence and nucleon decay. This light allows for the search for monopoles over a wide range of speeds [Djilkibaev and Spiering, 1998].

2.7.1 Cherenkov light

In a transparent medium, characterised by a refractive index n, charged particles emit photons if they move with a speed $\beta = v/c$ higher than the group velocity $c_n = c/n$ of light in the medium. Here c is the vacuum light speed. The photons are emitted coherently under a fixed angle θ_C given by

$$\cos(\theta_C) = \frac{1}{\beta n}. \tag{2.23}$$

For water or ice with a refractive index $n \approx 1.33$, the Cherenkov angle θ_C is $\approx 41.2°$ if the particle moves at the vacuum light speed. The number of photons emitted per track

length dx and wavelength interval $d\lambda$ is given by

$$\frac{\mathrm{d}^2 N}{\mathrm{d}x\,\mathrm{d}\lambda} = \frac{2\pi\alpha z^2}{\lambda^2}\left(1 - \frac{1}{\beta^2 n^2}\right) \tag{2.24}$$

where α is the electromagnetic fine structure constant, z is the charge number of the particle and λ is the wavelength of the emitted photons. This results in a light output in the visible range of 300 nm $< \lambda <$ 650 nm, as shown in figure 2.6. This light emission is caused by the energy transfer from the charged particle to the electrons of the nuclei of the surrounding medium. The energy transfer is mediated by the particle's electric field. By virtue of its motion, the monopole will acquire an electric field similar to that of a moving electric charge [Jackson, 1975].

When formula 2.24 is evaluated for monopoles [Tompkins, 1965, Kolokolov et al., 1999], the charge number z^2 has to be replaced by $(\mu/en)^2 = 8300$, where n is the refractive index of the medium. This will result in a light output of about 10^6 photons per cm in the wavelength interval between 300 nm and 600 nm. The threshold in speed above which radiation can be produced is given by $\beta > 1/n \approx 0.75$.
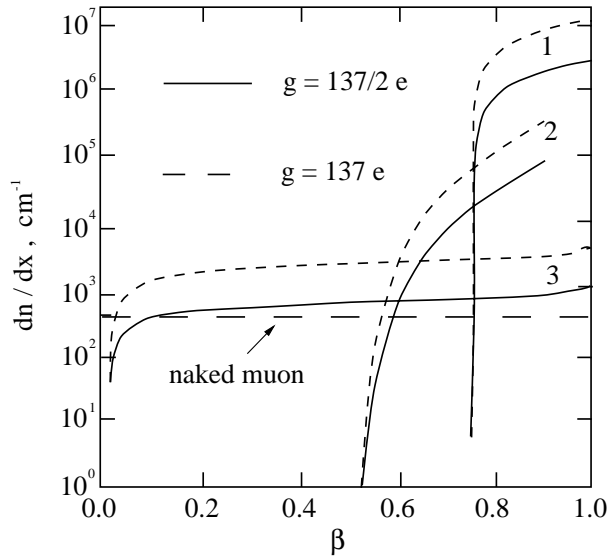
Figure 2.6: Number of Cherenkov photons generated between 300 nm and 650 nm per centimetre track length for various mechanism. 1: Cherenkov radiation, 2: δ electrons, 3: Radio luminescence. Taken from [Djilkibaev and Spiering, 1998]. The light output for doubly charged monopoles predicted e.g. by [Lazarides and Shafi, 1983, Lazarides and Shafi, 1984] is also given.

2.7.2 Production of δ-electrons

In the velocity range of $0.5 < \beta < 1$, part of the monopole's energy loss (~ 1 GeV/cm) is transformed into kinetic energy of δ-electrons. Their maximum kinetic energy is given

by [Domogatsky and Zheleznykh, 1969]

$$E_\delta = 0.69 \times 2 \times m_e(c\beta_{\mathrm{MP}}\gamma_{\mathrm{MP}})^2 \qquad (2.25)$$

where $m_e(c\beta_{\mathrm{MP}}\gamma_{\mathrm{MP}})^2$ is the kinematic limit for the energy transferred to the electron. The factor 0.69 arises from the fact that there is a lower limit of the impact parameter due to the extension of the electron wave function in the atom. The Cherenkov threshold for the δ-electrons of 0.264 MeV requires monopoles moving at a speed of at least $\beta = 0.52$.

A monopole generates the following number of δ-electrons per energy and track interval:

$$\frac{\mathrm{d}n_e}{\mathrm{d}E_e\,\mathrm{d}x} = \frac{4\pi N_e}{E_m} \times \left.\frac{\mathrm{d}\sigma}{\mathrm{d}\Omega}\right|_{\mathrm{R}} f_\Omega(\psi) = \frac{2\pi N_e e^2 g^2}{m_e c^2 E_e^2} f(E_e), \qquad (2.26)$$

where

$$f(E_e) = f(E_e(\psi)) = \left.\frac{\mathrm{d}\delta}{\mathrm{d}\Omega}\right|_{\mathrm{R}} \Big/ \left.\frac{\mathrm{d}\delta}{\mathrm{d}\Omega}\right|_{\mathrm{KYG}}. \qquad (2.27)$$

Here, $\mathrm{d}\sigma/\mathrm{d}\Omega|_{\mathrm{R}}$ is the classical Rutherford cross section for scattering a free electron off a fixed monopole and $\mathrm{d}\sigma/\mathrm{d}\Omega|_{\mathrm{KYG}}$ is a quantum mechanical cross section [Kazama et al., 1977]; ψ is the scattering angle. The factor $f_\Omega(\psi)$ varies between 1 and 2, but it becomes important only at angles above 70 degrees. This is the case for high energy transfers ($E_e/E_m \geq 0.3$) to the electron. The number of photons radiated from the electron is given by

$$\frac{\mathrm{d}n_\gamma}{\mathrm{d}x} = \int_{E_e}^{E\mathrm{max}} \mathrm{d}E_0 \frac{\mathrm{d}^2 m_e}{\mathrm{d}E_0\,\mathrm{d}x} \int_{E_e}^{e_0} \mathrm{d}E \frac{\mathrm{d}n_e}{\mathrm{d}x_e} \left|\frac{\mathrm{d}E_e}{\mathrm{d}x}\right|^{-1}. \qquad (2.28)$$

Here, $\mathrm{d}E_e/\mathrm{d}x$ is the ionisation loss of electrons in water, more specifically

$$\frac{\mathrm{d}E_e}{\mathrm{d}x} = \frac{2\pi r_e^2 mc^2}{\beta_e^2}\left(\lg\frac{2mc^2 W\mathrm{max}\beta_e^2}{I^2(1-\beta_e^2)} - \beta_e^2\right), \; W\mathrm{max} = \frac{m(c\beta_e\gamma)^2}{2(1+\gamma)}. \qquad (2.29)$$

The number of Cherenkov photons $\mathrm{d}n_\gamma$ emitted per unit path length $\mathrm{d}x_e$ in the wavelength interval between λ_{min} and λ_{max} amounts to

$$\frac{\mathrm{d}n_\gamma}{\mathrm{d}x_e} = 2\pi\alpha\left(\frac{1}{\lambda_{\mathrm{min}}} - \frac{1}{\lambda_{\mathrm{max}}}\right)\left(1 - \frac{1}{n^2\beta_e^2}\right). \qquad (2.30)$$

For the wavelength interval between 300 nm and 650 nm, the number of photons produced rises from 10/cm at $\beta_{\mathrm{MP}} = 0.52$ to 10^4/cm at $\beta_{\mathrm{MP}} = 0.75$. However, this number is so small compared with the Cherenkov light produced directly by the monopole that the production of δ-electrons will be neglected in the simulation of monopoles.

2.7.3 Radio-Luminescence of monopoles in water

Above $\beta_{\mathrm{MP}} = 0.01$, monopoles in water can stimulate molecular excitations. These can dissipate part of their energy also in the form of light into the surrounding medium. Using

a 5 MeV α particle source, the light generation was determined in the Baikal experiment to be

$$G \approx 2 \cdot 10^{-7} \gamma/\text{eV} \tag{2.31}$$

This number gives a conservative estimate for the light output caused by a monopole passing through water [Trofimenko, 1992]. The radiation thus would be sufficient to register monopoles in the velocity range between $\beta_{\text{MP}} = 0.01$ to 0.03. A graphical comparison to the other mechanisms is given in figure 2.6.

2.7.4 Nucleon decay

The possible structure of a GUT monopole shown in figure 2.1 suggests that the gauge boson X contained within can mediate transitions between hadrons and leptons, so a monopole can induce proton decay. The cross section can be estimated geometrically to be $\sigma \approx R^2 \sim M^{-2} \sim 10^{-56} \text{cm}^2$ [Kolb and Turner, 1990]. This cross section is much too small to result in observable events. However, the fermion-anti fermion condensates which are present in the outer layer of the monopole, will enhance the cross section to the order of the strong interaction ($\sigma \approx 10^{-26} \text{cm}^2$)[Callan, 1982, Rubakov, 1982]. For very small monopole speeds β_{MP}, the velocity dependence is given by

$$\sigma = \frac{1}{\beta_{\text{MP}}} \left(\frac{\sigma_0}{E_0^2} \right) \tag{2.32}$$

with E_0 of the order of the proton mass (1 GeV). The uncertainty in the dimensionless number σ_0 is quite large; the preferred value is 10^{-4}, but it extends from 10^{-6} to 1. Some typical decays would be

$$p + M \quad \rightarrow \quad M + e^+ + \pi^0 \tag{2.33}$$

$$n + M \quad \rightarrow \quad M + e^+ + \pi^- \tag{2.34}$$

$$p + M \quad \rightarrow \quad M + e^+ + \mu^+ + \mu^- \tag{2.35}$$

$$p + M \quad \rightarrow \quad M + \mu^+ + K^0 \tag{2.36}$$

$$p + M \quad \rightarrow \quad M + \mu^+ + K^0 + \pi^- \tag{2.37}$$

Monopole catalysis would be very effective for the generation of energy in stars. Whereas the pp solar cycle converts only 0.7% of the rest mass into energy, the monopole catalysis would be able to achieve almost 100% conversion efficiency. Only about 10^{28} monopoles would be necessary to produce the Sun's current luminosity. On the other hand, the neutrino flux expected in this production (from the decay of the pions) is in disagreement with measurements from neutrino detecting experiments using Gallium [Hampel et al., 1996].

When a monopole causes a nucleon decay, a quark in a proton is converted to a lepton, but the monopole also interacts with the rest of the nucleon. This has to be taken into account by a factor $F(\beta)$ enhancing the cross section of equation 2.32. E.g. for oxygen and free protons, the corresponding values are $F(\beta) = 2.4 \cdot 10^7 \cdot \beta^{3.1}$ and $F(\beta) = 0.17 \cdot \beta^{-1}$

18
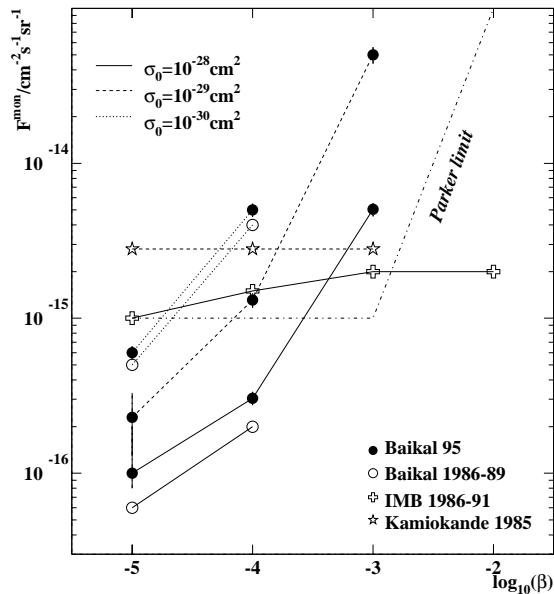
Figure 2.7: Upper limits (90 % C.L.) on the flux of magnetic GUT monopoles as a function of their velocity β for different catalysis cross sections σ_0 [Belolaptikov, 1994].

respectively. In water, a slowly moving monopole ($\beta < 10^{-3}$) should induce proton decays with a cross section of

$$\sigma^p_{\text{cat}} = 0.17 \times \left(\frac{\sigma_0}{E_0}\right) \times \beta^{-2}. \tag{2.38}$$

From this, one can calculate the mean distances and mean time differences between two decays:

$$\Delta\lambda_{\text{cat}} = 5.9 \times \beta^2 \times \left(n_N \frac{\sigma_0}{E_0}\right)^{-1} \tag{2.39}$$

$$\Delta\tau_{\text{cat}} = 5.9 \times \beta \times \left(cn_N \frac{\sigma_0}{E_0}\right)^{-1} \tag{2.40}$$

where $n_N = 6 \cdot 10^{23} \text{cm}^{-3}$ is the proton density in water. After the decay, the energy ($m_p c^2 = 938$ MeV) is distributed among the fragments (δ-electrons, e^+-e^--pairs, ...) of the proton. All of them will emit Cherenkov light. The decay channel given by equation 2.33 yields $1.1 \cdot 10^5$ photons per centimetre in the wavelength range between 300 nm and 650 nm.

For the other channels, the light output is lower, since other secondaries, such as neutrinos, carry away energy that is not turned into Cherenkov radiation; or particles with speeds below the Cherenkov threshold are emitted. The faintest light is produced by the channel shown in equation 2.37 ($3 \cdot 10^4$ photons/cm). The signature of a monopole with $\beta < 10^{-3}$ would be bursts of light along the path of the monopole separated by time intervals on a μs to ms scale. Monopoles in the velocity regime of $\beta = 0.5 - 1$ would primarily cause the decay of oxygen ($\sim \beta^{3.1}$) and emit a bright trace along the whole track.

The former would be measured by monitoring the counting rate of the array, the latter by the reconstruction of slow tracks. Such a search has been performed in the BAIKAL experiment, giving the results shown in figure 2.7.

2.8   Monopoles passing through the Earth

When a search for monopoles is performed which is based on the Cherenkov principle, the speed of the monopoles has to be higher than the light speed in the surrounding medium. At the same time, Cherenkov detectors are buried deep underground to reduce background from atmospheric processes, which produce particles, mostly muons, reaching the detector from above, see chapter 3. Thus, two searches for the upper and the lower hemisphere will be performed. For the lower hemisphere, the muonic background is small and the sensitivity is better. However, monopoles will have to cross the Earth. For the upper hemisphere, background is larger but monopoles reaching the detector can have a much smaller mass:

Consider the search for monopoles from below. In order to be detectable by Cherenkov light, the monopole has to cross the Earth and still be relativistic after this. A monopole looses energy by interaction with atoms and molecules when the electronic levels are disturbed by the magnetic field of the monopole. Above velocities of $\beta > 0.1$ the energy loss is given by the Bethe-Bloch formula adapted by Ahlen [Abbes et al., 1996]:

$$\frac{\mathrm{d}E}{\mathrm{d}x} = \frac{4\pi N_e \mu^2 e^2}{m_e c^2} \left[\lg\left(\frac{2 m_e c^2 \beta^2 \gamma^2}{I}\right) - \frac{1}{2} + \frac{k}{2} - \frac{\delta}{2} - B_m \right]. \tag{2.41}$$

Here, N_e is the electron density, μ the magnetic charge and I the mean ionisation potential. Additionally, the density correction δ, the QED correction k and the Bloch correction B_m are taken into account. The Earth's mantle consists mostly of silicon and the core of iron, and the energy losses for these elements were calculated by [Derkaoui et al., 1998]. For a monopole with single Dirac charge, the energy loss was predicted to be ~ 30 GeV/cm for silicon and $\sim 80 - 100$ GeV/cm for iron in the velocity regime $\beta > 0.75$. A monopole traversing the Earth's diameter ($\sim 1.3 \cdot 10^9$ cm) will thus loose between $4 \cdot 10^{10}$ GeV and $1.3 \cdot 10^{11}$ GeV. However, this is a pessimistic estimate, because on average the monopole will only traverse a thickness of material

$$\langle r \rangle = \frac{\int_{-1}^{0} \mathrm{d}\cos\theta \, r(\cos\theta)}{\int_{-1}^{0} \mathrm{d}\cos\theta} = \frac{1}{2} D \tag{2.42}$$

where $r = D \times \cos\theta$ is the path travelled through the Earth in dependence on the zenith angle θ, with D the Earth's diameter.

In the following, the speed of the monopole after traversing the Earth is calculated. The total energy of a monopole with speed $\beta = v/c$ is given by

$$E = m_0 \gamma \tag{2.43}$$

with the Lorentz factor $\gamma = 1/\sqrt{1 - \beta^2}$. The kinetic energy is obtained by subtracting the rest mass m_0:

$$E_{\text{kin}} = E - m_0 = m_0(\gamma - 1) \tag{2.44}$$

Crossing the Earth leads to a reduction in energy of $\Delta E = 2 \times R_E \times dE/dx$ with R_E the radius of the Earth. After traversing the Earth, the monopole has a kinetic energy $E_k' = E_k - \Delta E$, resulting in a Lorentz factor

$$\gamma' = \frac{m_0(\gamma - 1) - \Delta E}{m_0} + 1. \tag{2.45}$$

This leads to the following relation between the Lorentz factors before and after traversing Earth:

$$\gamma - \gamma' = \frac{\Delta E}{m_0}. \tag{2.46}$$

If one demands $\beta' > 0.75$, the following relation is obtained:

$$\frac{m_0}{\Delta E} > \frac{1}{1/\sqrt{1 - \beta^2} - 1/\sqrt{1 - 0.75^2}}. \tag{2.47}$$

This is visualised in figure 2.8. Outside the shaded area, monopoles can experience an
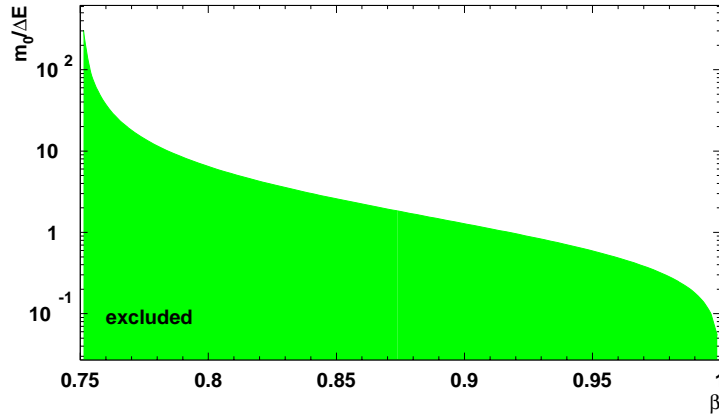
Figure 2.8: Region in the $m_0/\Delta E - \beta$ plane for which monopoles will be relativistic ($\beta' > 0.75$) after loosing ΔE.

energy loss ΔE and still be fast enough to produce Cherenkov light. As the ratio $m_0/\Delta E$ is approximately 1 at $\beta = 0.9$, the mass must be at least the amount of the energy loss:

$$m_0 \geq \Delta E \approx (4 \cdot 10^{10} - 1.3 \cdot 10^{11})\text{GeV}, \tag{2.48}$$

if the monopole goes through the Earth along its axis. For monopoles reaching the detector from close to below the horizon, approximately 200 km of rock and ice will

be passed by and the energy loss will be around 10^{8-9} GeV. The more conservative assumption made in equation 2.48 is comparable to $m_{\mathrm{MP}} = 10^{11}$ GeV as predicted in [Kephart and Weiler, 1996, Weiler and Kephart, 1996]. The lighter (10^9 GeV) $SU(15)$ monopoles would be able to cross the Earth only with a β close to 1 which they could achieve in the field of galaxy clusters, leading to $\gamma = 10^{16}\mathrm{GeV}/10^9\mathrm{GeV} = 10^7$, resulting in $\beta = 1 - 10^{-4}$.

For monopoles from above (i.e. a zenith angle below 90°), the maximal path length for travelling through the ice is about 180 km (for a detector depth of 2000 m). In ice, a monopole will lose approximately 12 GeV/cm, leading to a total energy loss of 2.2×10^8 GeV. Thus, searching in the upper hemisphere would allow the detection of monopoles with a mass as low as 2.2×10^8 GeV. The lightest possible observable mass is given by approximately 10^6 GeV when the monopole enters the ice above the detector and goes down perpendicularly.

What is the influence of the Earth's magnetic field on the monopole? The energy change suffered by a monopole when travelling through a magnetic field B for a distance L is given by

$$\Delta E = 10^{14}\mathrm{GeV} \times \frac{B}{\mu\mathrm{G}} \times \frac{L}{\mathrm{Mpc}} \tag{2.49}$$

Using the Earth's magnetic field of 59 μG [Barton, 1997] and the Earth's diameter of 4.3×10^{-16} Mpc, the change in energy for a monopole would be 0.2 MeV. From this one can conclude that the local magnetic field is of minor influence.

Chapter 3

Neutrino physics and detection mechanism

The detector which will be used in the analysis, AMANDA, is an ice Cherenkov telescope. The primary physics goal of this class of experiment is the detection of neutrino sources in the universe.

Neutrinos in the cosmos are thought to be produced by the collision of matter accelerated in sources with the surrounding medium ("cosmic beam dump"). In the collisions, pions and kaons emerge which in turn decay into leptons and neutrinos. Among the possible sources are X-ray star binaries, active galactic nuclei and young supernova remnants [Gaisser et al., 1995, Halzen and Zas, 1997]. Neutrinos reaching the Earth may eventually undergo a charged current reaction, which again produces leptons of different flavours, depending on the flavour of the neutrino. If the secondary muons travel through a transparent medium faster than light propagates in it, they emit Cherenkov radiation, which is detectable with photomultipliers.

3.1 Muon neutrino detection

Since the cross section for the neutrino reactions is very small, a large volume of transparent target matter has to be provided in order to get a significant number of events, making oceans, lakes or glaciers a natural choice. In the target matter, neutrinos are subject to neutral or charged current processes, yielding muons if the current is charged. In case of high energy neutrinos, the resulting muons travel a length $R_\mu \sim E_\mu$ below 10 TeV and $\sim \log E_\mu$ above. At muon energies of 10-100 TeV, R_μ is in the order of 1000 m. The angle between the neutrino and the muon is given by $1.5° \times \sqrt{E_\nu/\text{TeV}}$ [Dalberg, 1999]. These facts can be used in an underwater detector and will increase the volume in which particles can be detected well beyond the instrumented volume (figure 3.1). The neutrinos which will be detected are of extraterrestrial or terrestrial origin (figure 3.1, right, 1 and 2). The terrestrial neutrinos are produced by reactions of the cosmic radiation in the atmosphere

23
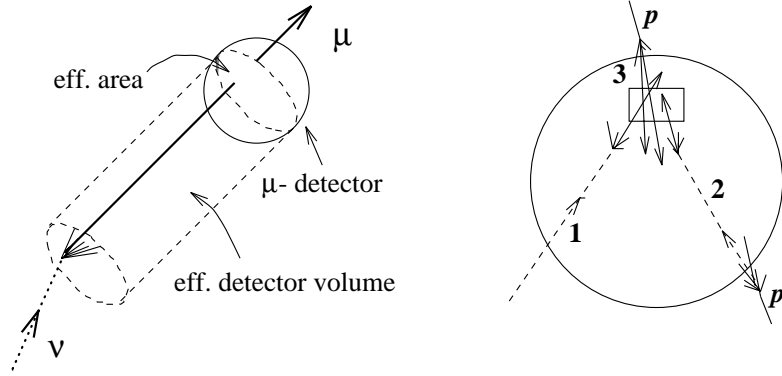
Figure 3.1: Left: A neutrino converts into a muon. The muon travels in the medium and is finally detected. Right: The possible signal sources: 1. An extraterrestrial neutrino is converted into a muon close to the detector. 2: A terrestrial neutrino, generated by cosmic rays in the atmosphere. 3: Muons generated by cosmic radiation reaching the detector from above.

and can cross the earth. Muons generated in this case can reach the detector from above (3) only, as the range of muons in rock is 7-8 km only. The ratio of downward/upward muons is depth dependent, going down from 10^{11} at sea level to 10^6 at 1000 m.w.e. (meter water equivalent) and to 10^4 at 4000 m.w.e. [Biron et al., 1997]. Thus, one will look for tracks coming from the lower hemisphere to suppress the muonic background.

3.1.1 Detection of muon tracks

The muons produced from neutrinos emit Cherenkov radiation in the ice, which can be recorded by a grid of photomultiplier tubes, mounted into pressure tight spheres. This is the basic building block of a Cherenkov telescope and is called an optical module or OM for short. The arrival time of the Cherenkov wave front (emitted at 42°) can be used to reconstruct the muon track and thus the neutrino track, see figure 3.2. The number of photons emitted per cm in the wavelength interval 300-600 nm is about 330. The muons undergo continuous (ionisation loss) and statistical energy losses (bremsstrahlung, pair production, ...). The total energy loss can be described by $-dE_\mu/dx = a + b \times E_\mu$ where a and b represent the continuous and statistical processes, respectively. The stochastic losses contribute to the light output, too, and lead to a rise of the effective area with the muon energy. The flux of muons passing through the detector depends on the neutrino flux itself and the conversion probability $P_{\nu \to \mu}$, which depends again on the neutrino energy E_ν, the cross section and the density of the medium. The numerical value for 1 TeV neutrinos at the AMANDA specific detection threshold of some 10 GeV is $P_{\nu \to \mu} \approx 10^{-6}$.
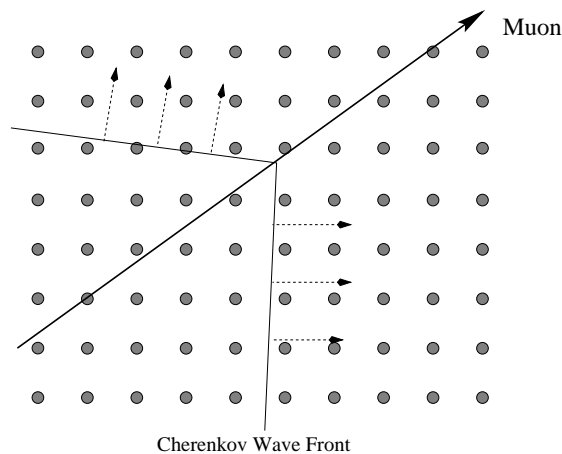
Figure 3.2: A muon traversing a grid of photo multipliers. Light emitted from the track propagates along the Cherenkov wave front.

3.2 Other physics

3.2.1 Detection of showers

With a sufficiently dense grid of photo multipliers, quasi point-like events like electromagnetic or hadronic showers can be detected. In contrast to the track like emission of light like in the case of muons, the light emerges from a relatively small, spherical volume. This is illustrated in figure 3.3. The detection efficiencies here are strongly dependent on
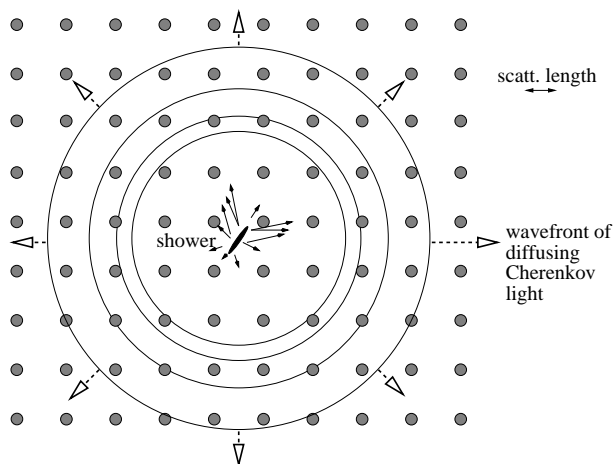
Figure 3.3: A shower leads to spherical emission of light.

the spacing. The reconstruction gets better the higher the photo multiplier density and the longer the photons can travel before they are absorbed by the medium. If the free

path between two scatterings decreases, the energy reconstruction is enhanced because scattering isotropises the light, leading to its containment in a certain volume.

The importance of this method lies in the possibility to detect PeV electron neutrinos produced in proton gamma interactions in AGNs. The detection would take place by observing the Glashow resonance:

$$\bar{\nu}_e + e^- \rightarrow W^- \rightarrow \text{shower}$$

It is also possible to detect isolated TeV showers from ν_e and neutral current ν_μ reactions, although the accuracy will be worse than for PeV showers.

3.2.2   Counting rate monitor

The explosion of a Supernova of type II or Ib leads to the emission of a huge flux of neutrinos. Actually, more than 99% of the Supernova's energy is released in neutrinos of all flavours and types where the energy is distributed over all of these. Their thermal energy is approximately 4 MeV. The cross section of the electron anti-neutrinos is the highest leading to the production of positrons via

$$\bar{\nu}_e + p \rightarrow n + e^+.$$
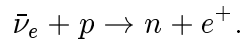
The average energy of the positrons is 20 MeV. The flux of neutrinos from a supernova is high enough to copiously produce positrons which radiate a detectable amount of Cherenkov light (figure 3.4). The detection is done by adding the counting rates of all modules in the array. The duration of one such event is of the order of 10 s [Burrows et al., 1992]. The production of copious numbers of positrons of about 20 MeV energy in the interaction of $\bar{\nu}_e$ with hydrogen will suddenly yield signals in all OMs for the 10 s duration of the burst.
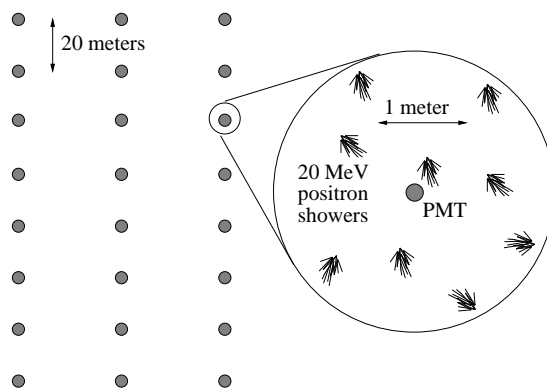
Figure 3.4: Operation of the array as counting rate monitor.

3.3   Overview over planned and existing Cherenkov telescopes

The first attempt to build a neutrino telescope was DUMAND [Grieder et al., 1990, Wilkes, 1994], a project in 4.8 km depth off the coast of Hawaii. Unfortunately, this project has been terminated, but a lot of the R & D work and experience can be used in the design and construction of the present generation of neutrino telescopes.

The first array to take data was the BAIKAL telescope [Balkanov et al., 1999b] located in the Siberian Lake Baikal. Currently, 192 modules are arranged on 8 strings. BAIKAL demonstrated the feasibility of reconstructing and separating up going muons. Currently the experiment identifies 1-2 up going events per week.

The ANTARES detector [Hubbard, 1999] already deployed a demonstrator string off the coast of Toulon. The next stage detector will be a 13 string device.

Another project, NESTOR [Bottai, 1999], is to be started at 3.8 km depth in the Mediterranean off the coast of Pylos, Greece. A 12-floor tower supporting the OMs in hexagonal arrays is planned.

A description of AMANDA will be given in the following chapter.

Chapter 4

The AMANDA Detector

In the last chapter, the basic detection mechanism for neutrinos was discussed, namely the inelastic scattering of muon neutrinos from which a muon emerges, i.e. $\nu_\mu + N \rightarrow \mu + $ anything. However, the cross section for this process is small (10^{-38}cm$^2 - 10^{-33}$cm^2 for neutrinos in the energy range of 1 GeV to 10 TeV [Gandhi et al., 1991]), a large detection volume is required to obtain the desired event rates. In the future, one would like to detect a few neutrinos per day.

As it is not the neutrino which will be detected, but the Cherenkov light emitted by the muon which emerges in the reaction, it is necessary to determine its direction with high efficiency and precision. This sets the requirements to the detection medium, i.e. that it should be available in large volumes and have suitable optical properties. The former leads to the use of water, which is abundant in the oceans and glaciers, the latter leads to the location.

The optical properties are characterised by the so called scattering length and the absorption length. The absorption length λ_{abs} describes after which distance the number of photons injected at a point is reduced to $1/e$, whereas the scattering length λ_{scatt} describes the mean distance between scatterings of the photon. To take into account the scattering angle Θ and thus compare media which differ in this parameter, one introduces the effective scattering length λ_{eff} which is defined by $\lambda_{\text{eff}} = \lambda_{\text{scatt}}/(1 - \langle \cos \Theta \rangle)$, where $\langle \rangle$ indicates averaging.

To detect the muon's Cherenkov light undisturbed, the light sensing devices should be not further away from the muon than λ_{eff}, which fixes the grid width of the detector array. The optical properties will be discussed further in the following section 4.1.

Another consideration to be made is the sky coverage of the device. As there already existed a working telescope in the northern hemisphere and DUMAND was also planned for the northern hemisphere, AMANDA was chosen to be located in the southern hemisphere.

It was thus natural to use the glacier of central Antarctica and use the already existing infrastructure at the Amundsen-Scott South Pole station. During the Austral winter a group of about 40 people stays at the station two of which service the detector or act

on requests from the outer world. Communication is possible via three satellites, which ensure a connection during half of the day; so far, all-day communication has not been possible because of the shadowing of the South Pole from the orbit of the satellites. The firm surface of the central Antarctic glacier serves as a stable platform for the installation of the data acquisition system.
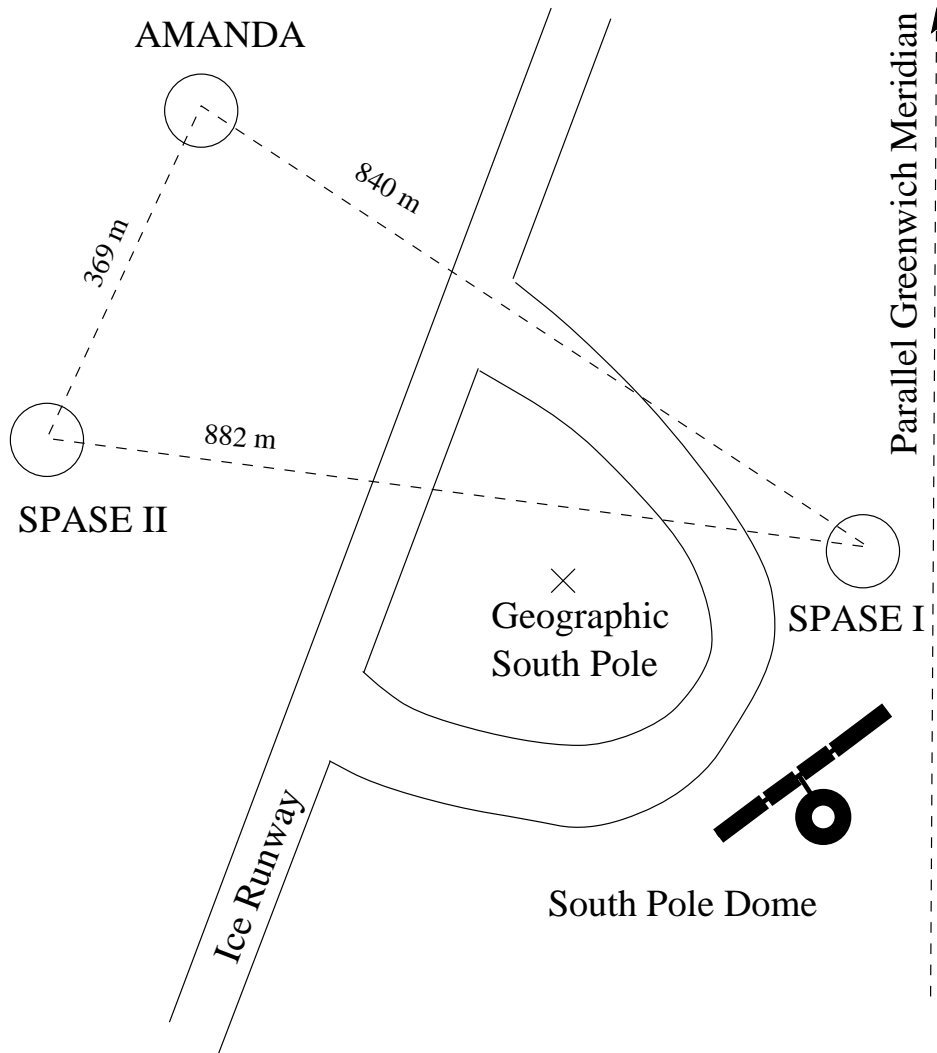
Figure 4.1: Location of the AMANDA detector at the Amundsen-Scott South Pole station. The position of the surface air shower arrays SPASE-I and SPASE-II is also given.

The ice has a thickness of approx. 3000 m. Since it is not known how strong the shear forces at the bedrock are, the maximum depth of instrumentation is 2350 m. AMANDA was built successively in stages during several Austral summer seasons. During the 1994/1995 season, four strings were deployed at a depth between 810 m and 1000 m
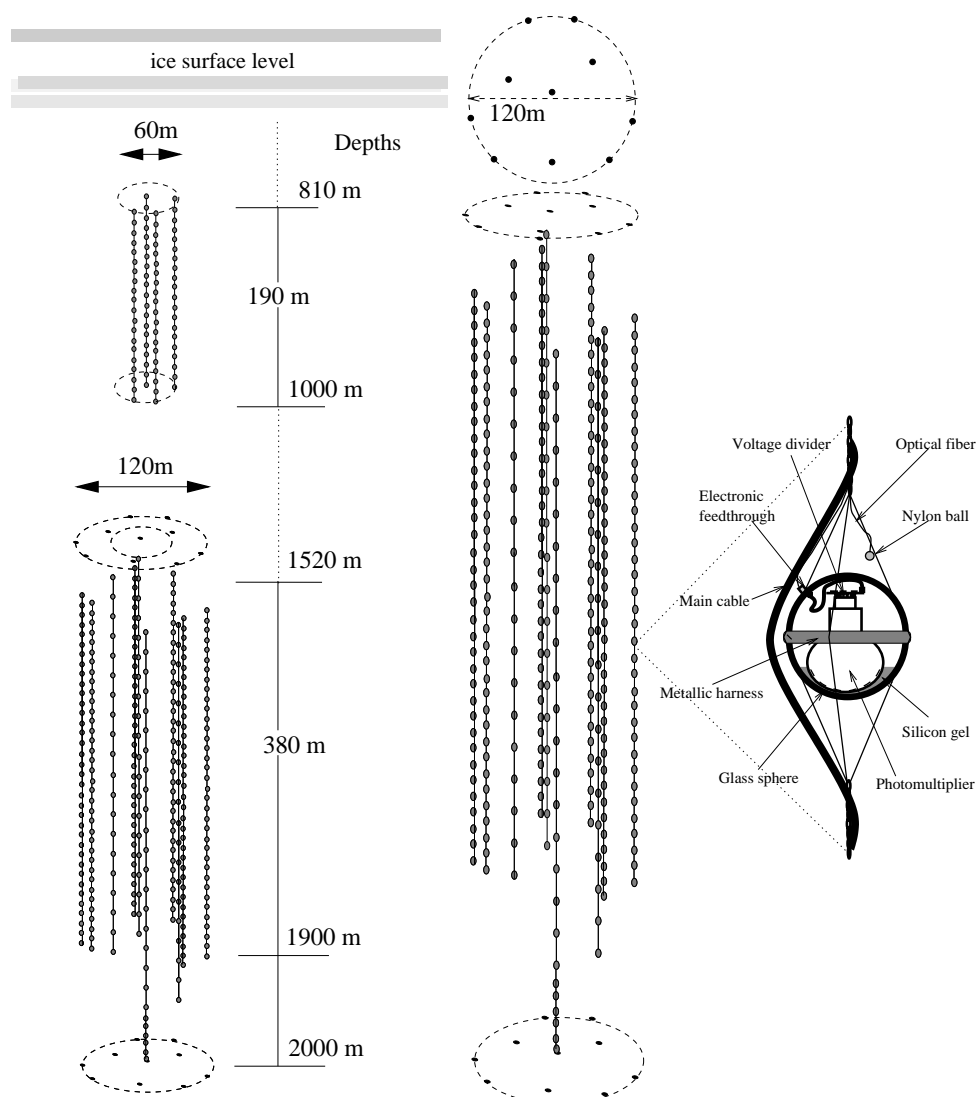
Figure 4.2: Sketch of the AMANDA detectors. AMANDA-A is located between 810 m and 1000 m depth. AMANDA-B consists of 10 strings at depths between 1520 m and 2000 m depth.

depth (AMANDA-A).

However, it turned out that the ice at this depth has unsatisfying optical properties. Light is scattered to a great amount and the Cherenkov wave front is destroyed, inhibiting the reconstruction of tracks. Thus in the 1995/1996 season four strings were deployed at a depth of 1520 m to 2000 m (AMANDA-B4). Here the ice is clear enough to allow efficient reconstruction. During the 1996/1997 season AMANDA-B4 was augmented by 6 strings to AMANDA-B10. The position and depth of AMANDA are shown in figures 4.1 and 4.2 respectively. During the 1997/98 season, the detector was extended by 3 strings and the

final extension of the 19 string AMANDA-II detector was reached during the 1999/2000 season by installing another 6 strings.

At the surface above the AMANDA detector, two air shower arrays (SPASE-1 [Smith et al., 1989], SPASE-2 [Dickinson et al., 2000], "South Pole Air Shower Experiment") are installed which can be run in coincidence with AMANDA, defining a "test beam" of atmospheric muons.

4.1 Ice properties

The light propagation between the light source and the optical module is governed by the properties of the ice. The scattering and absorption of photons varies with the depth. Inhomogeneities are present because the formation of the Antarctic ice did not take place in an even way: various climates resulted in different ice properties by admixture of dust and aerosols present in the atmosphere. In order to determine these properties, a solid core should be drilled at the South Pole and its properties determined. This was already planned for the Deep Ice project, which has not been approved. Instead, since the ice at the Pole is some 10000 years old, the measurements taken from a core drilling at the Russian Vostok station were used and extrapolated to the South Pole. These estimates lead to the assumption that the dust concentration will be lowest in a depth between 1500 m and 2000 m. Above and below this region the dust concentration rises strongly.

After precipitation the snow is loosely packed and contains much air between the crystals. As more snow falls and compresses the lower layers, a phase transition eventually occurs where the air is built into the ice crystals (clathrate), leaving a very clear ice, starting at a depth of about 1200 m. The distances between the modules were thus chosen to be in the order of the scattering length of about 20-30 m, see figure 4.3.

The ice properties have to be considered separately for the so called bulk and hole ice. The ice which is generated by the re-freezing of water in the hole after deployment will be referred to as hole ice, whereas the ice undisturbed by the drilling which surrounds the holes is called bulk ice. The absorption and scattering are described by the absorption length λ_{abs} and the scattering length λ_{scatt} and its scattering angle distribution. An effective scattering length λ_{eff} can be defined by

$$\lambda_{\mathrm{eff}} = \frac{\lambda_{\mathrm{scatt}}}{1 - \langle \cos(\theta) \rangle}. \tag{4.1}$$

The advantage of the effective scattering length is that it makes it possible to compare media with different distributions of the scattering angle.

The inverse of the effective scattering length has been measured using the various devices described in section 4.2. The result is shown in figure 4.3. The figure includes the scattering ($b_e = 1/\lambda_{\mathrm{eff}}$) and the absorption properties. The measurements of the absorption are compared to a model by [He and Price, 1998]. The measurement of the scattering was performed for one wavelength only. One sees that these properties depend on the
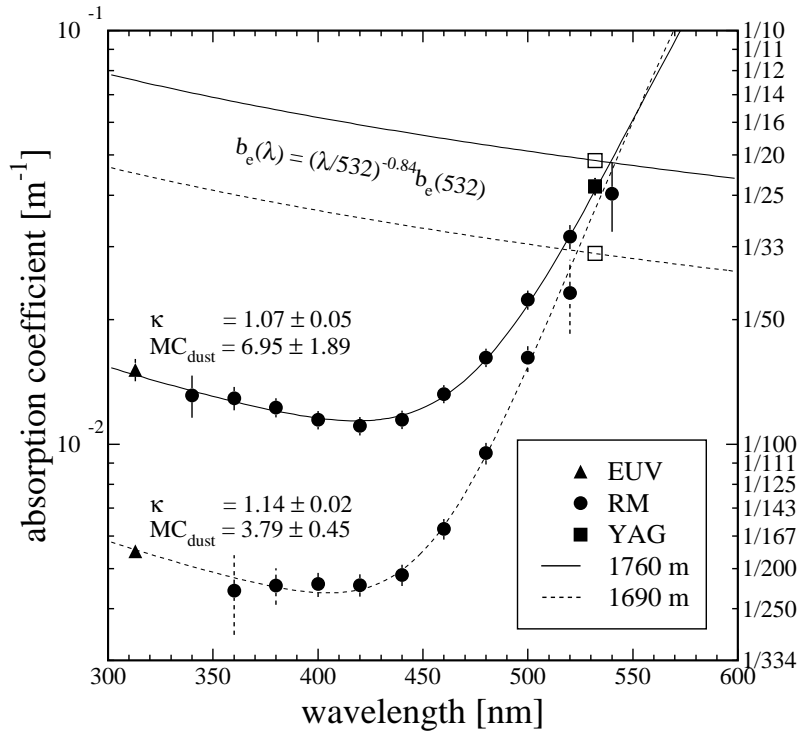
Figure 4.3: Scattering ($b_e = 1/\lambda_{\text{eff}}$) and absorption ($1/\lambda_{\text{abs}} = f(\kappa, \text{MC}_{\text{dust}})$) as a function of wavelength for two depths, 1760m and 1690 m. The unit of the absorption coefficient is the same as the scattering coefficient b_e. The lines represent the prediction from the model by [He and Price, 1998], parametrised by κ and MC_{dust}. Measurements have been performed using a DC halogen lamp with a λ=313 nm filter (EUV), a YAG laser which is tuneable with a dye ("Rainbow Module"), and a high intensity YAG laser (YAG).

depth. A thorough survey of the ice has been made in [Woschnagg, 1999]. This leads to the implementation of layers of ice with different properties in the detector simulation which is currently used.

The properties of hole ice were examined by various methods. It is e.g. possible to consider the response of the detector to atmospheric muons, especially the light arrival times in neighbouring modules. This will be discussed in appendix A. The scattering length in the hole was determined to be λ_{eff}=63 cm. This result will be made use of in the simulation in chapter 6.

4.2 Deployment

The deployment of the detector takes place in several stages. For each string of OMs a hole has to be drilled in the ice. Because of the large diameter of the optical modules

(about 43 cm) the diameter of the hole should be 50 cm at least to prevent modules from getting stuck. Because drilling a solid core of this size is expensive and time-consuming, hot water drilling using an 1.9 MW boiler is used. The ice is melted and the drill head sinks further down at a speed of approximately 1 cm/s. The water does not re-freeze before about 30 h, leaving enough time for the deployment of the string. During the 1997/98 season, one string was equipped with a camera to observe the re-freezing. It was found that the ice does not regelate homogeneously, but air bubbles form. The effect of these was investigated in the framework of this thesis and is summarised in appendix A.

The drill head is equipped with tilt-meters measuring the inclination of the head and thus provides a survey of the hole. Getting down to 2 kilometres takes about 3 and a half days. As soon as the required depth is reached, the string deployment starts. As the main cable is lowered down the hole and a connector passes the top of the hole, an optical module is attached to the cable. During deployment, the cable attenuation is measured by a transient data recorder (TDR) and the resistance of the photo multiplier tube is measured to find bad connections between the modules and the main cable.

Additionally, thermometers and pressure gauges are deployed in order to measure the reached depth and monitor the re-freezing process. As the ice passes its minimal density at -4 degrees, the pressure reaches a maximum of about 460 atm but decreases to half of this value as the ice re-freezes and the pressure will drop to the hysdrostatic pressure, which is 200 atm in 2 km depth. After re-freezing, thermodynamical equilibrium is not reached before several months. Then, the temperature at the surface is about -55 °C and -30 °C at the bottom. The re-freezing process is the most critical phase in deployment because it puts the highest mechanical stress on the components; however, the failure rate is low (10% for AMANDA-B4 and 3% for the 6 other string of AMANDA-B10). So far, only one module has been lost after the re-freezing process.

For calibration purposes of the array, light emitters are also deployed. Two optical fibres run along the cable to each optical module. One is a single mode fibre, with an FWHM time resolution of ≈ 7 ns at 530 nm, the other is a multi mode fibre with an FWHM resolution of ≈ 15 ns at the same wavelength. At the surface they are connected to a YAG and a dye laser, whose light they guide down to a nylon ball diffuser 50 cm below the module.

This arrangement allows for time calibration of the modules in the following way: from an optical transient data recorder (OTDR) measurement one knows the time it takes a light pulse to travel from the laser to the nylon ball. The photo multiplier inside the module converts laser light into an electric signal, whose time delay is measured. This is done using the high resolution single mode fibre for each individual optical module, which are operated at a gain of 10^9. Thus, the light output of the diffuser does not need to be high. However, the laser can reach a maximum light output of 10^8 photons/pulse at the surface. Using the multi mode fibre, one can illuminate neighbouring strings and perform a position calibration and determine ice properties at different wavelengths. In addition, several DC halogen lamps allow the measurement of light absorption in the ice between the string. A lamp is installed into an aluminium cylinder in a pressure sphere.

The cylinder's lid has an opening of approximately 5 cm diameter. In front, there is a broadband and an interference filter and an isotropising foil. Two types of lamp modules with a wavelength of 350 nm and 380 nm are available, too.

4.3   Strings

As mentioned before, the AMANDA-B detector consists of 302 modules arranged in ten strings. The detector centre is at 1750 m below the surface.

- **String 1:** Consists of 20 Hamamatsu photo multiplier tubes (PMT). It extends from 185 m above to 195 m below the detector centre. All optical modules (OM) look down with the exception of the uppermost (OM 1) and the middle (OM 10) ones. LED emitters ("beacons") are placed above module 1 and below modules 7, 12 and 19. A nitrogen laser-module is placed 10 m below OM 16.

- **String 2:** Also consists of 20 Hamamatsu PMTs. The extension is from 184.7 m above to 196.3 m below the detector centre. The top and middle ones (OM 1 and 10) look upward. LED modules are placed under the modules 1, 7, 13 and 19 and a DC halogen lamp is located 10 m below OM 16. A frequency doubler is also installed.

- **String 3:** 20 PMTs, number 1 and 2 are of Thorn EMI 9353 type, the others are built by Hamamatsu. Extension reaches from 132.3 m above to 247.7 m below the detector centre. OM 1 and 10 look upward and a DC halogen lamp is placed below module 16.

- **String 4:** 26 PMTs from 154.1 m above to 305.3 m below the detector centre. Modules 1, 10, 20, 21, 23, and 25 look downward. LED modules are installed above modules 1 and 10. The lowest six modules 21 to 26 are connected by twisted pair instead of coaxial cable. This was done as a test for the next six strings with 36 modules, where a cable containing 36 coax cables would become too thick and unfit for deployment.

- **Strings 5 to 10:** These were deployed in the 1996/1997 season. Thanks to the experience gathered from strings 1 to 4, it was possible to deploy 6 strings with 36 modules each. The spacing between the modules has been reduced from 20 m to 10 m and the instrumented length is approximately 350 m. All face down and are equipped with Hamamatsu 5912-2 PMTs. The electrical readout is done via twisted-pair cables. 21 of the OMs are equipped with a LED, which is driven by the anode current of the PMT. The LEDs light output is coupled to a fibre. This allows a very precise timing because of the small FWHM time of 4 ns. Two OMs are designed for digital readout. A 1-ns wave form digitiser processes the PMT signal

and the binary information is sent to the surface via twisted pair cable. Additionally, the following devices were installed [Lowder, 1997]:

1. Laser diode pumped YAG laser at the surface. It emits photon pulses with 532 nm at a repetition rate of 10 kHz with an energy of 0.1 mJ per pulse.

2. YAG laser and dye at the surface. It emits at wavelengths between 475 nm and 610 nm and allows redundant measurements.

3. Blue LED beacons at various depths emit light at 390 nm and 450 nm. They can be operated in DC and pulsed mode at a repetition mode of 500 Hz to 5000 Hz.

4. DC halogen lamps at various depths. They are visible up to more than 200 m. The emitted light is of broad band type or filters can be used to obtain 313 nm, 350 nm and 380 nm. One lamp is tunable between 350 nm and 650 nm.

5. Nitrogen lasers at 1800 m depth. The output rating is 0.1 mJ per pulse and the visibility is greater than 200 m.

6. Thermistors register the temperature and allow observation of the onset of re-freezing.

7. Pressure sensors determine the string depth and monitor the pressure during re-freezing.

8. Inclinometers allow the assessment of shear forces on the cables over time.

9. Devices which measure the transparency of ice and water in the drill-hole.

4.4　The optical module

The light sensing in AMANDA is performed by so called optical modules (OM). These consist of a photo multiplier tube (PMT) housed in a glass pressure sphere, as shown in figure 4.4. Optical contact between the sphere's surface and the photo cathode of the multiplier is established using optical silicon gel. The pressure sphere also houses the voltage divider for the PMT. The tube's signal is transmitted to the outside of the sphere via a pressure tight GISMA/Diamond connector.

The PMT itself is a Hamamatsu R5912-2 model. Based on the R5912 model, the number of dynodes was increased from 12 to 14 in order to yield signals strong enough (amplification is 10^9) to be sent over $\sim$2 km of cable. The bialkali photo cathode has a diameter of 100 mm seen from the front on a sphere with a curvature radius of 131 mm. The sensitivity covers wavelengths between 300 nm and 650 nm and peaks with 23% at 420 nm (see figure 4.4).

Between the cathode and the first dynode a grid focuses the electrons in order to get high efficiency and good timing. The voltage divider was designed to give high sensitivity, however, this limits the dynamic range of the tube to $\sim$10 pe. Timing and amplitude
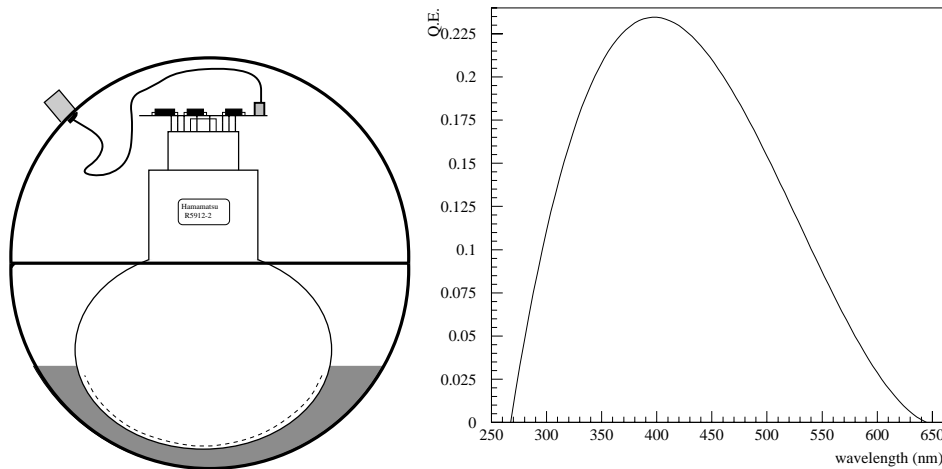
Figure 4.4: Arrangement of the photo multiplier tube in the glass pressure sphere (left). To the right, the quantum efficiency as a function of wavelength is shown.

properties were determined in the lab and at the Pole after deployment. In the lab, a transit-time jitter of 3 ns FWHM was measured. This increases to 4 ns - 5 ns after transmission over 1.6 km - 2.0 km of cable. At the same time the amplitude is attenuated from 1 V at the tube to several mV at the end of the cable. The rise time is increased to 180 ns and the time-over-threshold to 550 ns. This makes it impossible to count single photons by counting leading edges at the surface. As was shown in the lab by using a 2 km long cable, there is linearity between the number of photo electrons (pe) and the amplitude [Öhrmalm, 1997]. The peak to valley ratio of the 1 pe peak at 10^9 gain is 1.5.

Slowly drifting remaining gas ions between the cathode and the dynode can cause afterpulses. The timing and probability of these were determined in the lab with a threshold set to 1/4 pe using a short cable. Afterpulses were observed at 2 μs and 7 μs after a pulse caused by a photon and the probability was found to be between 5% and 30% for different PMTs, see figure 4.5.

The influence of the magnetic field on the properties of the PMT were found to be small [Öhrmalm, 1997]. The geomagnetic field at the South Pole has a strength of 57 μT and an inclination of 17°. The influence of the field on the PMT depends on the orientation of the latter, but it was found that, integrated over the whole photo cathode, the effect on the collection efficiency is at most 2%. Both transit time and jitter are changed by about 1 ns. The effect increases from the centre of the cathode towards the edge.

The PMTs' noise rates are between 0.5 kHz and 1.5 kHz when measured in the lab but drop to between 0.3 kHz and 0.5 kHz in strings 1 to 4 and to 1.2 kHz in strings 5 to 10 due to lower thermionic emission. The higher frequency in strings 5 to 10 is due to the fact that the pressure sphere in strings 5 to 10 has a higher K^{40} content[1] than the spheres

---

[1]The spheres were originally designed aiming at mechanical stability which is achieved by adding potassium to the glass, introducing the K^{40} contamination.
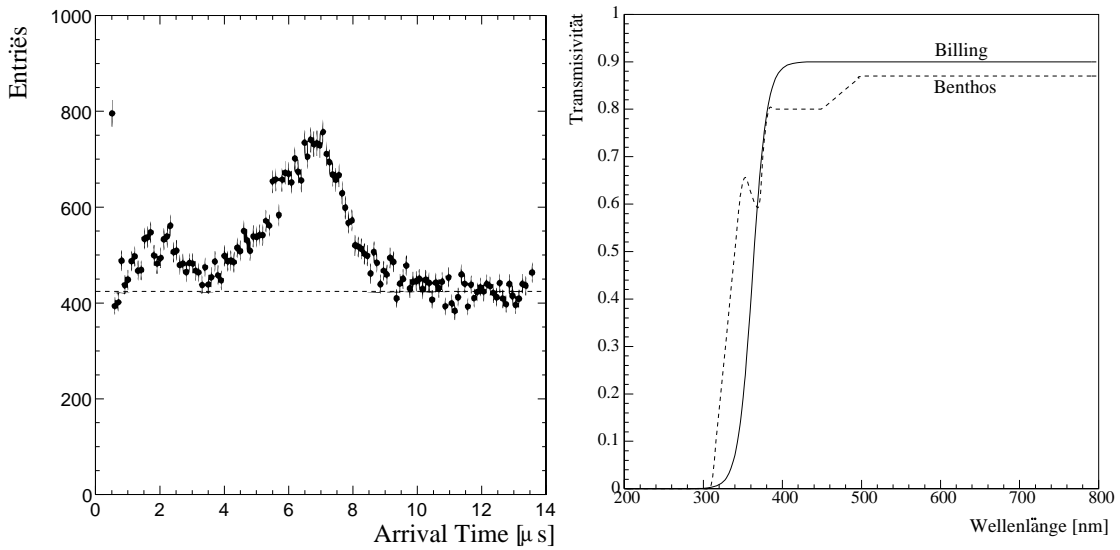
Figure 4.5: Left: Timing and frequency of after pulses, taken from [Hundertmark, 1999]. Right: Transmissivity of glass spheres as a function of wave length.

used in string 1 to 4.

The pressure spheres used for strings 1 to 4 were made by the company Billings. The diameter is 30.5 cm and the thickness 9 mm. In strings 5 to 10, spheres made by the manufacturer Benthos (same dimensions) were used. Benthos spheres had already been used in AMANDA A, but the spheres needed to house the larger Hamamatsu PMT were not available at AMANDA B4 deployment time. The transmissivities of both types are seen in picture 4.5 (right). The Billings sphere has a slightly higher transmissivity above ~ 380 nm, but the Benthos sphere can transmit shorter wavelengths down to 334 nm. It is desirable to have a good transmissivity at low wavelengths because of the $1/\lambda^2$ shape of the Cherenkov light emission spectrum. One possibility to avoid this problem would be the application of wave length shifters. The problem of making a durable layer on the glass has not been solved yet, but studies are underway [Biron et al., 1997, Bauleo et al., 2000].

The optical contact between the PMT and the sphere is established by an optical silicon gel. In the arrangement used in 1997, the PMT and the voltage divider circuitry are the only electronic components. Thus all other sensitive devices can be positioned at the surface where maintenance is no problem.

In order to measure the angular sensitivity of an OM, a sample was placed into a water tank and illuminated under various angles by an LED [Wiebusch, 1996]. Unfortunately, it is difficult to perform a similar experiment with deployed modules using the installed light sources. However, it is assumed that the angular acceptance is isotropised by the presence of bubbles forming in the hole as the water re-freezes. The optical properties of the ice in the hole are discussed in detail in appendix A.

4.5 Electronics and DAQ

Basically, the electronics and DAQ have the task to assemble the information gathered by all OMs into a meaningful event which allows reconstruction of a particle track. The available information consists of the leading and trailing edges of the PMT signal and of its amplitude. Here leading and trailing edge times are defined as the time when the signal increases above or drops below a threshold. A maximum of eight leading/trailing edge pairs are recorded. A trigger is formed after collecting N_{hit} hits on N_{string} strings within a 2 μs wide sliding window. This value is due to the fact that it takes a particle $t = s/c \approx 600$m$/0.3$m$/$ns to transverse the detector (s is the size of the detector, c the speed of light used to approximate the particle speed).

In the ideal case the number of hits should be at least five to allow reconstruction of the five parameters of a track, and at least 3 strings are needed to avoid ambiguities connected to the Cherenkov cone. In order to keep the data rate manageable, to reduce ambiguous solutions and to enrich the sample with well-reconstructible events, N_{hit} was set to 16, N_{string} was set to 1 in order to allow for vertically upward moving muon tracks close to a single string. As the analysis in this work will use events from the high multiplicity regime, the effects of the trigger threshold are negligible.

AMANDA B10 can also be triggered by external detectors such as AMANDA A and SPASE making it e.g. possible to select a certain direction of incoming particles defined by the relative position of AMANDA B10 and the external detector.

The electronics consist of the following components (see figure 4.6):

- **Amplifier:** The supply voltage for the PMTs is generated by two LeCroy 1440 units. The high voltage is connected through the SWAMP (SWedish AMPlifier, [Thollander,]) down to the PMT. As photons arrive at the PMT, the tube draws some current and as a consequence, there is a slight drop in the high voltage. This drop is picked up by a DC-blocking high pass filter which is linear in the bandwidth of the pulses reaching the surface (0.1 MHz - 10 MHz) and subsequently fed into two separate amplifiers with an amplification between 2 and 200. In order to filter out noise from the lab environment at the South Pole, the lower end of the filter has to be quite high, causing a large overshoot in the signal. The first amplifier (called "A") is set to 100 and the second (called "B") is set to 25. The "A" signal is available after a threefold fan out, the "B" signal is delayed by 2 μs. 16 SWAMPS are built into one module which is inserted into a 9U-Euro crate.

- **Discriminators:** The "A" channels of the SWAMP are used for trigger and timing purposes and are discriminated using a LeCroy 4413 type producing ECL signals. The threshold is common to all 16 inputs and was set to 100 mV yielding 90% efficiency. The high-voltage on each PMT was set such that the 1 pe peak was at 400 mV after the SWAMP. The resulting voltages around 1700 V operate the PMT at a gain of around 10^9 [Lowder et al., 2000].

- **MADD Trigger Logic** will generate the trigger for the experiment. One SWAMP "A" output is fed into the so called MADD (Multiplicity ADDer) module. It is composed of several MULT20 modules and one ADDER module housed in an 6U-Euro crate [Gustafsson et al., 1996]. The MULT20 converts the ECL signals from the discriminator and stretches them over the trigger window time of 2 μs. The stretched signals are added and put into binary format, which is sent to the ADDER, which sums up the input from all the MULT20 modules. The sum is compared to the set channel multiplicity; from this a trigger decision is made. The total conversion time for the process is 100 ns with a jitter of 10 ns [Gustafsson et al., 1996]. The trigger decision is then sent to a NIM trigger logic which also takes into account the external triggers from AMANDA A, SPASE and GASP.

- **Time to digital converters (TDC):** The TDC is a 32 channel device, which can record 16 hit times with 0.5 ns resolution per channel, making it possible to store 8 leading edge- trailing edge pairs. The buffer used to store times has a width of 32 μs and is operated in common stop mode, which means that after the stop signal the last 32 μs are read out. This stop signal is generated by one of the "A" outputs of the SWAMP.

- **Analog-Digital Converters (ADC):** The "B" channel of the SWAMP is connected to a Philips 7164 16 channel peak sensing ADC. The large overshoot of the pulse prohibits the use of a charge sensing ADC.

The data acquisition is based on a CAMAC bus, which is operated by a Hytec LP1341 list processor from a Jorway 73A controller. The controller is connected to a MacIntosh PowerPC 7200 via the SCSI bus. The software used for DAQ is written in the KMAX language. It starts the readout and stores the events in a 32 kB buffer. Every 600 ms this buffer is read out in a single block transfer. The data is then directly written to an NFS mounted disk. The block transfer as well as the writing of the data imposes dead time on the system.

When a trigger is formed, a veto, which inhibits the acceptance of further triggers during readout, is set. In order to read out the amplitudes, a gate and stop signal is sent to the ADCs and TDCs to start the conversion. A GPS latch is operated, which makes the event time available on the CAMAC bus. Since a single CAMAC cycle via the SCSI bus is very time consuming (12 ms /cycle) a list processor takes away this task from the DAQ PC. After the data has been read out, the veto is cleared again and the DAQ is ready for the next event.

4.6   Description of the experimental data used

The data used in this analysis was taken throughout the year 1997. Apart from the normal muon data, all events with a channel multiplicity bigger than 100 were extracted and stored separately. The data is organised into runs, runs are divided into several
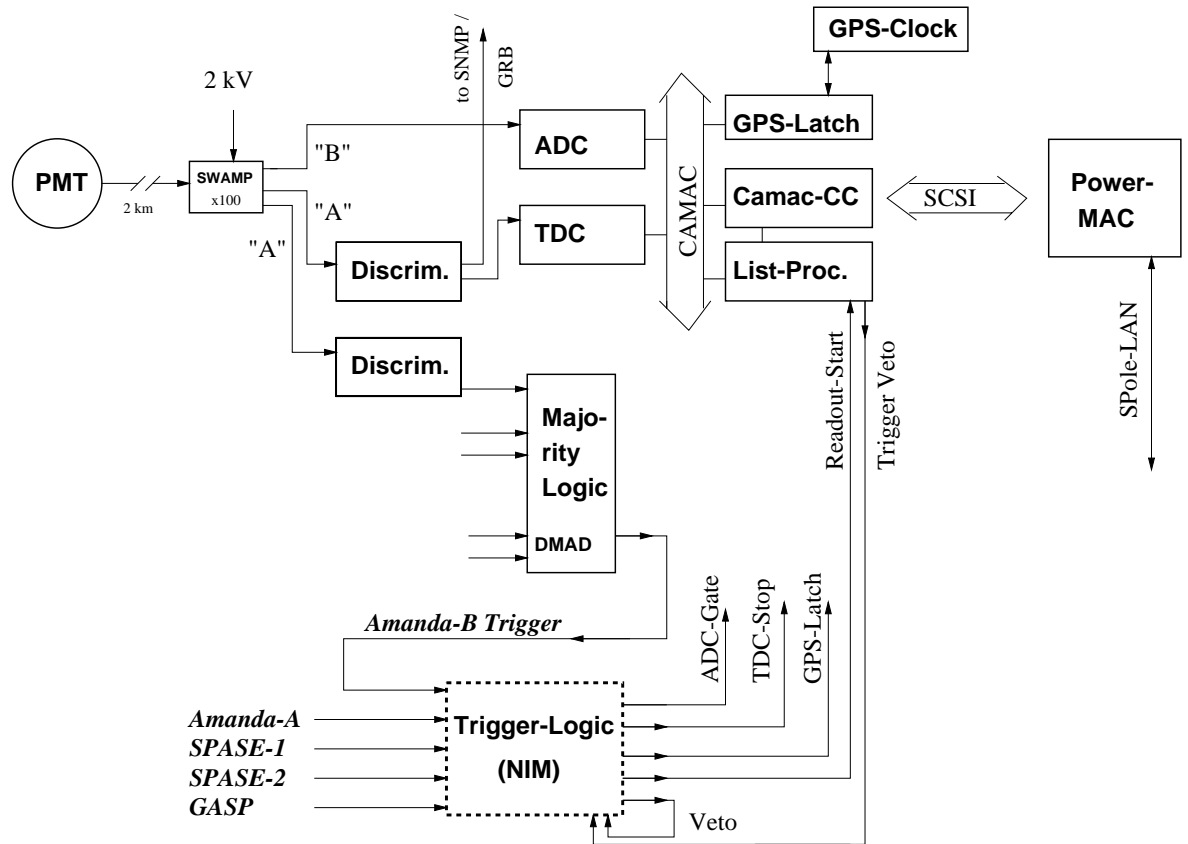
Figure 4.6: Schematic of the AMANDA-B DAQ during 1997.

files, where each file contains approximately 20 to 60 minutes of operation time (called T hereafter). After hit cleaning and reconstructing these files (see chapter 7), the rate was extracted from each file by dividing the number of events by the time of the first and last event. This method does not take into account if there are longer intervals (typically above 30 s) between events in a file, however, this rarely happens and will not affect the rates by more than a few percent. Plotting the rates vs. start time of each file yields figure 4.7.

Data taking actually starts before day 95, but there the number of operative OMs is 25 only [Biron et al., 1999]. Most of the time, the data rate is between 0.35 Hz and 0.5 Hz. One notices that towards the end of the season the rate increases after passing a minimum around day 220. This will be discussed later. The other striking feature are groups of files having a frequency below 0.1 Hz. For these files, the event multiplicity was found to drop dramatically. One of the causes was found to be a gradual phasing out of strings 8-10 in run 1116, day 316, file 41. Over its duration of approx. 1 hour, the contribution of strings 8 to 10 decreases continuously. This is yet to be explained, since an electronics failure would lead to a sudden breakdown of the strings. The strings 8 to 10 also fail on days 260 to 270 and 295 to 300. The low rate between days 180 and 190 was found to be

caused by failure of strings 1 to 4.

Another file had a rate of 2.4 Hz on day 104, caused by high noise on strings 8 to 10. The rest of the points off the bulk are caused by short runs with a few ten events, which introduce some fluctuation into the measurement. As has been described in [Bouchta, 1999],
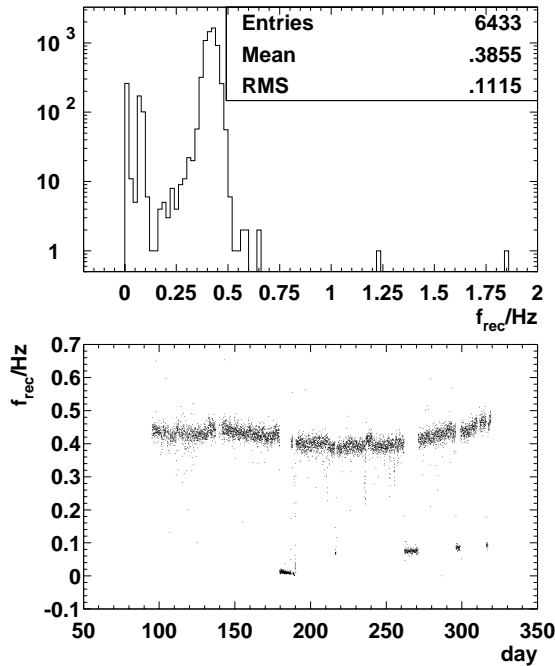
Figure 4.7: Rates for individual files histogrammed and drawn vs. time.

the reason for the rate variation over time is the change in thickness of the atmosphere above the Pole caused by temperature variation. In order to investigate this, weather data provided by the Antarctic Meteorology research Center (AMRC) and the Antarctic Support Associates (ASA) was used. Every day at the South Pole, a balloon is launched carrying a set of sensors measuring among other things temperature and pressure. During its flight, the device's height and direction are recorded as it transmits its data to the station. It can get up to heights of 40 km before the balloon bursts. Each flight thus yields a temperature and pressure profile of the atmosphere. In the Austral winter, around day 200 (mid July) the temperature is low, the atmosphere contracts. Thus the probability of a cosmic particle hitting an air molecule and produce short range secondaries is higher than in the summer, where the cosmic particles have a higher chance to decay into long ranging muons which will trigger the detector [Barrett et al., 1952]. A relation between the muon rate and an effective temperature was given by [Ambrosio et al., 1997]:

$$\frac{\Delta R_\mu}{\langle R_\mu \rangle} = \alpha_T \frac{\Delta T_{\text{eff}}}{\langle T_{\text{eff}} \rangle} \qquad (4.2)$$

where the effective temperature T_{eff} describes the averaging of the temperature T as a function of the atmospheric depth X, taking into account the pion and nucleon decay lengths Λ_π and Λ_N:

$$T_{\text{eff}} = \frac{\int_0^\infty \frac{\mathrm{d}X}{X} T(X) (\exp\{-X/\Lambda_\pi\} - \exp\{-X/\Lambda_N\})}{\int_0^\infty \frac{\mathrm{d}X}{X} (\exp\{-X/\Lambda_\pi\} - \exp\{-X/\Lambda_N\})}. \tag{4.3}$$

In equation 4.2, the relative variation of the rate and the effective temperature against their average values $\langle R_\mu \rangle$ and $\langle T_{\text{eff}} \rangle$ are related by the effective temperature coefficient α_T. In [Bouchta, 1999], the effective temperature coefficient was determined to be $\alpha_T = 0.86 \pm 0.05$ compared to the theoretical prediction of 0.9 [Barrett et al., 1952, Ambrosio et al., 1997]. The relation between the relative temperature change and the relative rate change is shown in figure 4.8. The observed high correlation leads to a
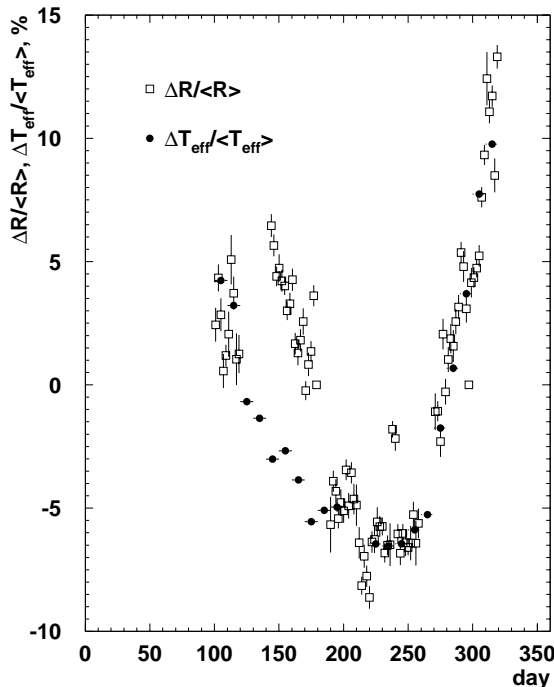
Figure 4.8: Relative variation of rate and temperature over the year 1997 for a sub-sample of $nch \geq 100$ events.

value of α_T close to one, compatible with the values mentioned above. However, between day 140 and 180, the high rate of the detector is not compatible with the expectation based on the temperature. This has already been observed in [Jacob, 1998]. There, the standard trigger (i.e. $nch > 16$) events were considered. Whereas the seasonal variation for $nch \geq 16$ is visible only after careful cleaning of the data, it becomes visible in the $nch \geq 100$ sub-sample which has been investigated in this work already after a minimal cleaning. The runs in the range with too high trigger rate were kept in the analysis.

4.7 Determining the fraction of observable events

When calculating a flux limit, the exposure time of the experiment has to be known. The exposure time is calculated from the operation time T the experiment actually runs, multiplied by the fraction of observable events (FOE). Since the detector and electronics has to perform the triggering, analog to digital conversion, event building and so on, it will be blind for a short time after a triggered event. This leads to a loss in the FOE η, defined as

$$\eta = \frac{N_d}{N_0} \tag{4.4}$$

where N_0 is the number of events which hit the detector and N_d is the number of events actually seen. The fraction η is a function of the rate f with which the events reach the detector and of the dead time τ it takes the detector to perform the actual readout of the event. In appendix D it is shown that η depends of f and τ like this:

$$\eta = \frac{1}{f \times \tau} \times (1 - \exp\{-f \times \tau\}) \tag{4.5}$$

For a practical determination of the FOE, Poisson statistics $P(n, \mu) = \mu^n/n! \exp\{-\mu\}$ is
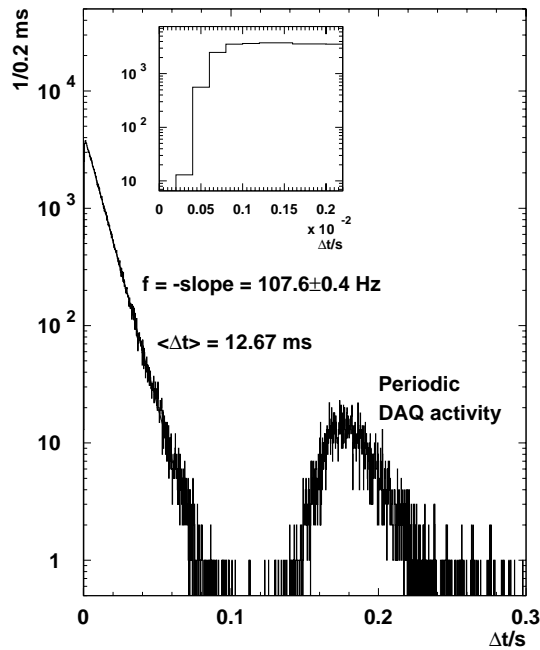
Figure 4.9: Distribution of time intervals between subsequent events Δt, taken from run 700 on day 141. The region between 0 and 2 ms is zoomed in.

used, where P is the probability to observe n events per time interval when on average μ events are observed in this time interval. Since the probability to observe no events for a given time Δt is proportional to

$$P(0, f \times \Delta t) = \exp\{-f \times \Delta t\}, \tag{4.6}$$

the slope of the distribution in logarithmic scale of time intervals between subsequent events gives the rate f of particles impinging on the detector. For a file from run 700 on day 141, all these time differences were plotted, resulting in the right frame of figure 4.9. Besides from the Poissonian distribution with the expected behaviour proportional to $\exp\{-f \times \Delta t\}$, some periodic activity is observed. Its period is distributed around a central value of 0.18 s. The reason is a periodic activity of the DAQ, namely the writing of a buffer to disk.

The time it takes to process an individual event which causes a short time of detector blindness can be measured from the inset plot, which shows the Δt distribution between 0 and 2 ms. For an ideal detector, there would be no decrease towards $\Delta t = 0$. In reality, the detector cannot see events separated by less than 0.5 ms on average. Applying this value to equation 4.5 yields a value of $\eta = 0.97$. However, this does not take into account the accumulation of Δt around 0.18 s. Thus the fraction of events has to be determined in another way. This can be done by comparing the number of events expected to the number of events observed. The number of expected events is given by the particle rate hitting the detector, $n_{\text{expected}} = f \times t_{\text{obs}}$. The number of measured events is given by the number of entries in the Δt histogram. The observation time is the sum of all times between the events, which can be expressed by means of the average $\langle \Delta t \rangle = \sum \Delta_t / n_{\text{obs}}$ with $\sum \Delta_t = t_{\text{obs}}$. Thus

$$\eta = \frac{n_{\text{obs}}}{n_{\text{expected}}} \tag{4.7}$$

$$= \frac{t_{\text{obs}} / \langle \Delta t \rangle}{f \times t_{\text{obs}}} \tag{4.8}$$

$$= \frac{1}{f \times \langle \Delta t \rangle} \tag{4.9}$$

From the above data sample with $f = 107.6$ Hz and $\langle \Delta t \rangle = 0.0127$ s, one obtains

$$\eta = 0.73. \tag{4.10}$$

The product $T \times \eta$ will be called live time of the detector. The rate for the high multiplicity $nch > 100$ events was measured in the same way, the corresponding plots are shown in figure 4.10. The rate is about 0.41 Hz.
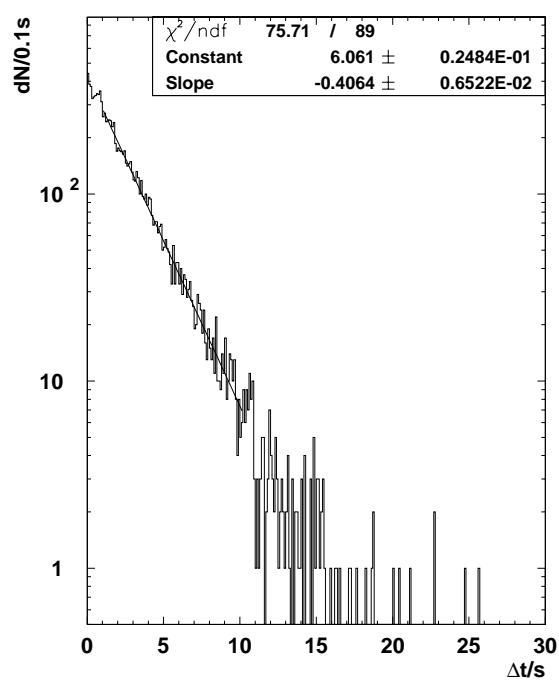
Figure 4.10: Time difference distribution between subsequent events, before processing.

Chapter 5

Calibration

The calibration of the timing and amplitudes takes into account the propagation time along the cable and converts the output of the recording electronics ("bins") into more meaningful quantities such as seconds for times or photo electrons for amplitudes. The following prescriptions are applied:

$$ t = t_{\text{TDC}} \times \beta_{\text{T}} - t_0 - \frac{\alpha}{\sqrt{A_{\text{raw}}}} \tag{5.1} $$

$$ A_{\text{pe}} = (A_{\text{raw}} - A_{\text{ped}}) \times \beta_{\text{A}} \tag{5.2} $$

The first equation relates the time t_{TDC} at which the signal from the OM reaches the TDC (see section 4.5) to the leading edge time t at which the Cherenkov light actually hit the detector. The time calibration constants β_{T}, t_0 and α allow a conversion between TDC bins and time (ns), and a subtraction of the propagation time in the cable t_0 and correction of the time slewing (see figure 5.1 and below). The second equation relates the ADC recording A_{raw} to units of photo electrons where the constants A_{ped} and β_{A} represent the pedestal and a conversion factor.

5.1   Time calibration

The leading edge time, i.e. the time at which the amplitude rises above a certain threshold, depends on the overall size of the pulse and on the pulse shape, as illustrated in figure 5.1. The effect is of the order of approximately 20 ns for the given example. The form of the correction term in 5.1 is motivated by assuming that the amplitude rises as the square of the time, $Amp \sim t^2$. Some pulses used in the simulation are shown in figure 5.2. Note that the twisted pair pulse (left, bottom) is shorter than the coaxial pulses. The leading edge time vs. $1/\sqrt{ADC/\text{mV}}$ is shown in the right part of the figure. When the amplitude of the pulse gets too low, the assumption of a quadratic behaviour of the leading edge upon the amplitude does not hold any longer, thus there is a deviation starting from $1/\sqrt{ADC} \sim 0.06$. A linear fit is done between 0.027 and 0.06, the calibration parameter α is then given by the parameter $A1$ in the fit.

45
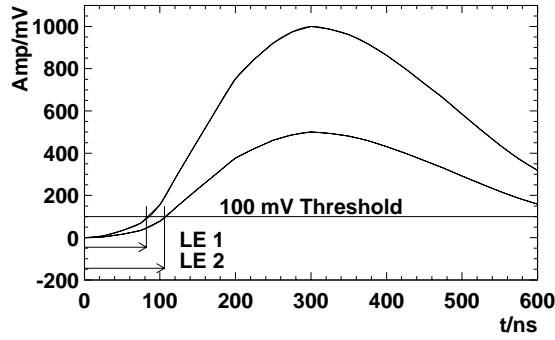
Figure 5.1: Time slewing: two identical pulse shapes with different amplitudes. If a fixed threshold is applied, the leading edge time LE, i.e. the time to cross the threshold, depends on the amplitude. The pulse is a B4 coax pulse, taken from [Hundertmark, 1999].
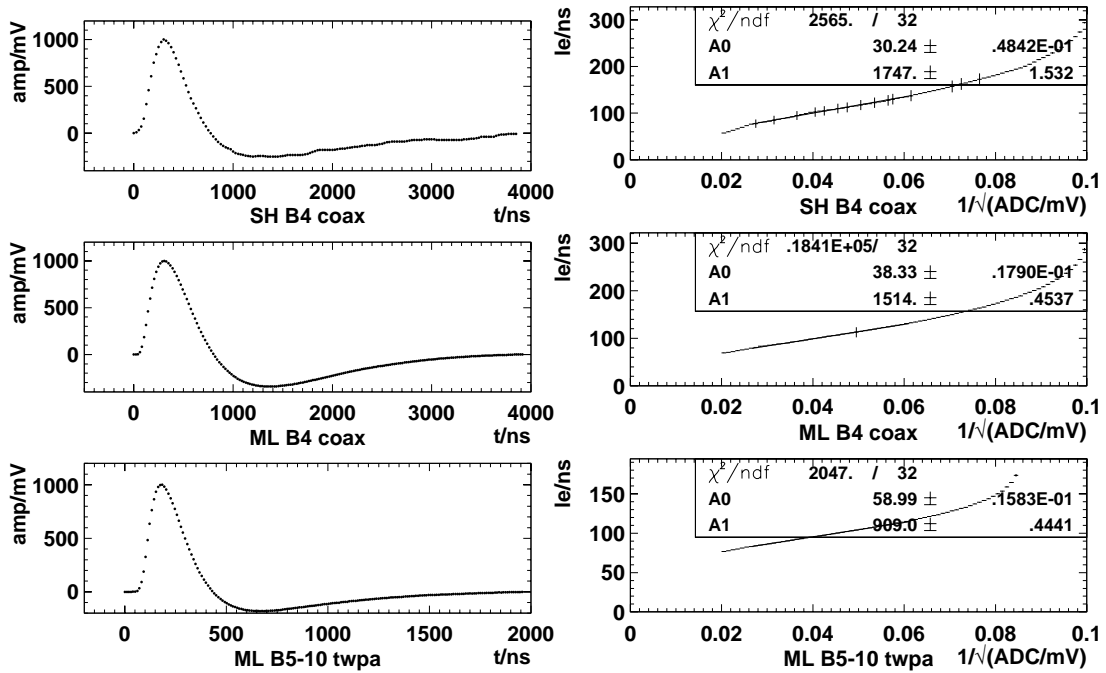
Figure 5.2: Left: Three pulse shapes measured for different cable types. These were used in the photo multiplier simulation part of the detector Monte Carlo. SH B4 was used for the generation of muonic background, the two lower (ML B4/ML B5-10) were used for the signal simulation. Right: The leading edge time as a function of $1/\sqrt{ADC/\mathrm{mV}}$ which is used for the determination of α. The nominal one pe pulse is at ~ 0.03.

5.2 Amplitude calibration

Amplitudes are calibrated using the dark noise of the PMT as a source of 1 photo electron (pe) signals. The high voltage is then set to the value at which the tube is operated at a gain of 10^9, i.e. for which the collected charge at the anode is 10^9 electrons. It is, however, found that there is a disagreement between the amplitude distributions of individual modules in Monte Carlo and experiment. Some examples of photo electron spectra taken from muon data are shown in figure 5.3. The probability per 0.5 pe bin
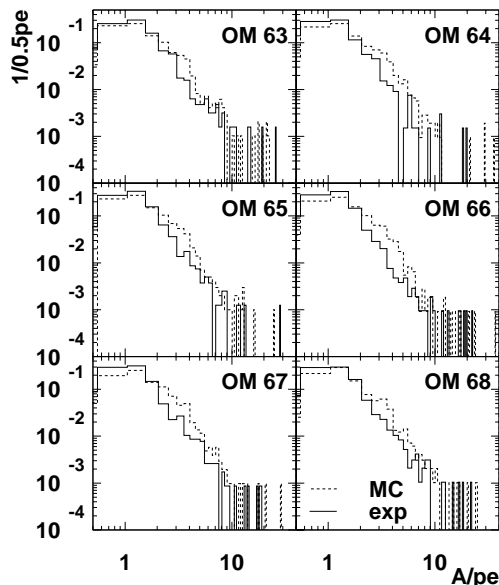
Figure 5.3: Amplitude spectra for some modules in experiment (solid) and Monte Carlo (dashed lines).

is given in these plots for experiment (solid line) and Monte Carlo (dashed line). The Monte Carlo on average gives too high a fraction of multi photo electron hits. The reason for this is not clear. Since the PMT in the experiment is run in an extreme amplification regime close to saturation, it might be that the assumption made in the Monte Carlo, namely that pulses add linearly, no longer holds.

Measurements performed with a YAG laser at the South Pole with *in situ* photo multipliers [Kowalski, 1999, Mihalyi et al., 2000] suggest that the calibration constant changes above 1 pe. This can be expressed by

$$A \mapsto A' = \begin{cases} A & : & A < 1\text{pe} \\ (A-1) \cdot \kappa + 1 & : & A > 1\text{pe} \end{cases} \tag{5.3}$$

where A and A' is the amplitude measured in units of photo electrons. In this way an amplitude $A > 1$pe is mapped to a smaller/bigger amplitude A', depending on whether κ

is smaller or bigger than 1. Applying this re-calibration using a κ of 1.5, it is possible to obtain a better agreement between Monte Carlo and experiment as shown in figure 5.4. Here alternatively experiment ($\kappa = 1.5$) or Monte Carlo ($\kappa = 0.67$) were rescaled; the result appears to be consistent. This implies one can perform the re-calibration on the much smaller sample of simulated data.
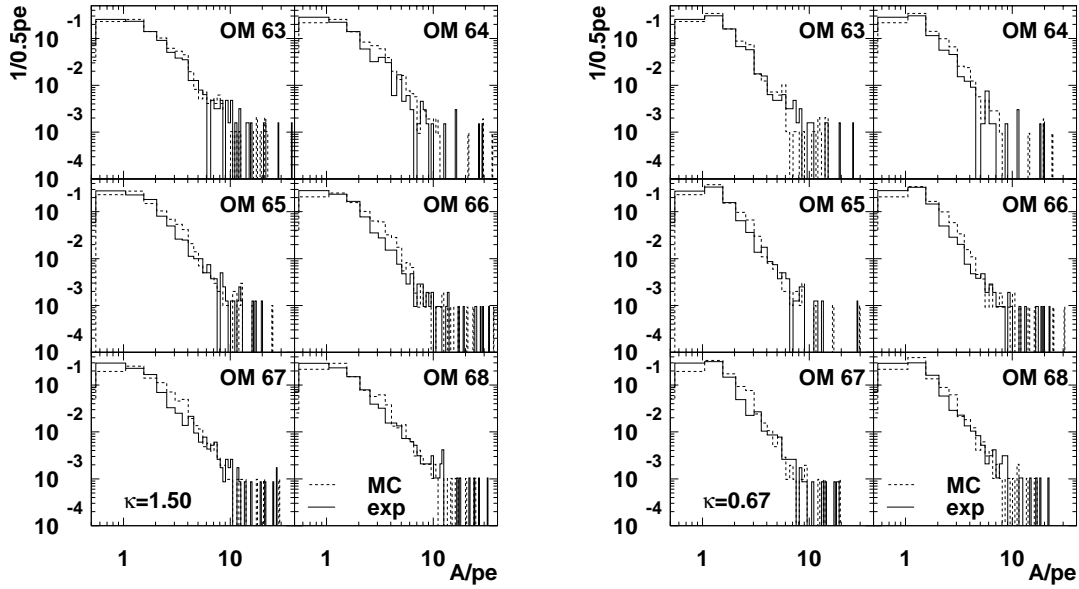
Figure 5.4: Amplitude spectra. Left: mapped A'(experiment), original A(simulation), right: original A(experiment), mapped A'(simulation).

A reliable amplitude information would be very desirable as it would allow an easy rejection of non-direct hits, i.e. hits in which the photon has been scattered so much that it has been delayed considerably. This is shown in figure 5.5. An iterative likelihood fit [Wiebusch, 1998b] was applied to experimental and Monte Carlo data. The amplitude information is not used in this method. A hit cleaning was performed during the fit, however all hits were kept in the data stream. In the plot, the time residual, defined as the difference between the actual arrival time of light at the OM and the arrival time predicted from the Cherenkov cone of a certain track, is plotted versus the number of photo electrons in this hit. Higher amplitudes are thus connected with smaller time residuals. Thus timing quality can be enhanced by weighting the hits according to their amplitude. This property will be made use of later in the reconstruction.
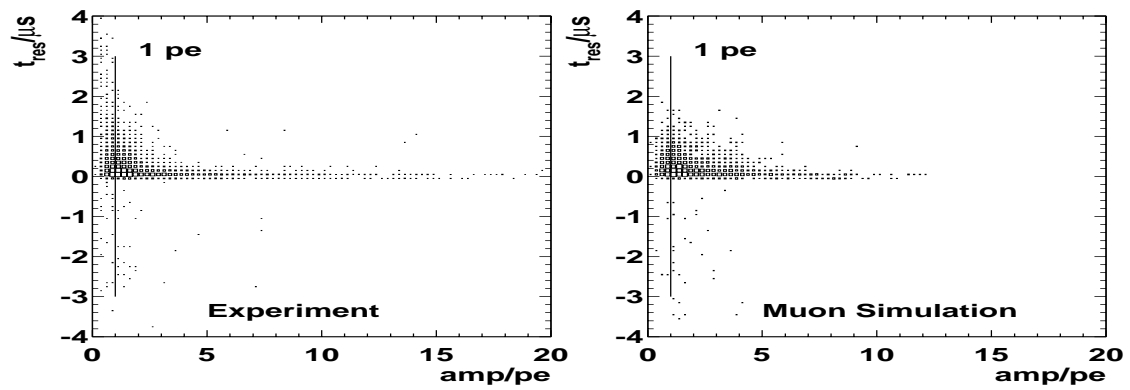
Figure 5.5: Time residuals (in ns) vs. amplitude (in pe) for an iterative likelihood fit. No amplitude weights are used in getting the fit, no quality criteria for the correctness of the fit are applied.

Chapter 6

Simulation

The simulation of events in AMANDA is done in several stages. The generation and tracking of the particles, the propagation of light from the track and the response of the detector are treated separately.

6.1 Track simulation

The first step of monopole simulation is to generate tracks. It was assumed that the track length is infinite. For the generation of monopole tracks, the program `muo0` [Bouchta et al., 2000] from the *SiEGMuND* package was used. It was run in such a way that particles start perpendicular to a plane of radius $R = 400$m. As discussed in section 2.7.2, secondary processes like δ-electrons are neglected because their light output is small compared to the Cherenkov light output from the monopoles.

6.2 Photon Transport and Detection (PTD)

When a photon is emitted along a particle track, it is subjected to scattering (as mentioned in chapter 4 above). Simulating this light propagation for every single event would be very time consuming and a different approach has thus been adopted by separating the photon propagation from the charged track simulation.

   The photon propagation and detection simulation (PTD, [Karle, 1998b]) is performed in cylindrical coordinates with longitudinal coordinate z and radial coordinate ρ. The azimuthal coordinate ϕ is not taken into account because of the cylindrical symmetry of the problem. The extension in z was taken from -350 m to 350 m and the maximal radius is set to 700m. Outside this volume no photons can be seen.

   Several light sources can be simulated, such as light from a shower, from point sources (simulation of the calibration laser) and emission from a particle track. For the present work, PTD was extended in order to handle not only particles with $\beta = 1.0$, but it is

possible to simulate the light emission of slower particles with speeds above the Cherenkov threshold.

The photons (typically 25000 per simulation) are injected into the ice under the desired Cherenkov angle. Each photon is tracked until a maximum distance or a maximum number of scatterings has occurred. The tracking of each photon is done on a grid representing time and space. The grid width is dependent on the distance, it is finer close to the track and coarser far away from the track, thus the simulation can cover a volume of ice without using up too much memory. This is achieved by using $\sqrt{t}, \sqrt{\rho}$ and $\sqrt{z}$ instead of t, ρ and z. In this work, the size of the archive was expanded to 51 bins from -350 m to 350 m in z, 36 bins from 0. m to 700 m to take into account the large visibility of the monopoles.

The absorption of the ice and the conversion from photons to photo electrons are applied on the resulting tables after the scattering is done. The absorption is included by scaling the numbers of photons at a certain distance down to the level given by the absorption function. The conversion from photons to photo electrons takes into account the spectral properties of the optical module, such as the transmissivity of the glass sphere. The orientation of the PMT relative to the incident light is also taken into account.

The final result is a table containing the distribution

$$\Phi(z, \rho, \theta, \phi, t) = \frac{dN}{dz\,d\rho\,d\theta\,d\phi\,dt} \tag{6.1}$$

giving the arrival time delay t and the mean number of photoelectrons N for a module at z, ρ and orientation θ , ϕ. Here, the time delay is defined as the time the photon travels on top of the Cherenkov time, i.e. the time the photon spends scattering. The amplitude is given in units of photoelectrons per square meter. A maximum quantum efficiency of 100% is assumed. The lower quantum efficiency of the individual OM is taken into account within the detector simulation. From this distribution a random time delay and incident angle will be sampled which will be used to simulate the fluctuations caused by the scattering.

6.3   Detector simulation with AMASIM

The detector response to a track has been described in great detail in [Hundertmark, 1999]. The AMASIM program uses a steering file containing all the information on the features which are to be simulated, such as after-pulsing, and noise hit generation. The detector is described by means of a separate file. This contains the location and orientation of the modules, the location of the one photoelectron peak in mV, the noise rate, the sensitive area, the relative sensitivity, the cable delay and the after pulse probability and delay.

The hit times and amplitudes of the modules have to be determined from a particle track starting at a vertex at a certain time. This is done in the following way: First, the so-called geometrical arrival time given by the Cherenkov light cone is calculated for

each module. From the PTD tables the mean number of photoelectrons per unit area is retrieved, and a mean number of photoelectrons $\bar{N}_{\mathrm{pe}}$ is obtained by multiplying the photoelectron density with the area of the optical module. Subsequently this number is multiplied by the quantum efficiency and the relative sensitivity of the OM. This is used to simulate the high light output a monopole gives by scaling the relative sensitivity by a factor 8300. This mean number of photoelectrons is then randomised by choosing a new value N_{pe} from a Poisson distribution with mean $\bar{N}_{\mathrm{pe}}$. For all the photoelectrons, a time delay is taken from the tables and each is assigned an amplitude.

The PMT jitter is simulated by adding a random time which is Gaussian distributed with a spread of 7 ns, where this value is chosen for historical reasons [Hundertmark, 1999]. This is actually a pessimistic assumption. Figure 6.1 shows the linear relation between the jitter and $1/\sqrt{ADC}$. This plot shows that the jitter is 6 ns for this very well behaved module (OM 1) for low amplitudes. With increasing amplitudes, the jitter lowers almost linearly with $1/\sqrt{ADC}$. Thus, the timing error in the experiment is actually smaller than
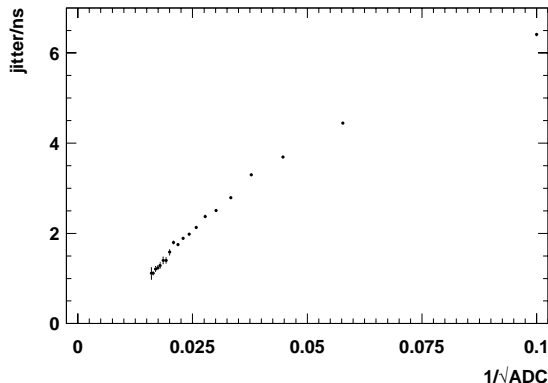
Figure 6.1: Photo multiplier jitter as a function of amplitude, taken from a laser *in situ* measurement of module 1 on string 1.

in the simulation, but it has been shown that an error of a few ns is not dramatic. The amplitude is calculated by using the inverse function method [Youssef, 1998]. A typical one-photo electron pulse form is then scaled according to the amplitude and a time offset is added according to the generated delay. All these pulses are then added linearly to give the final pulse form. A threshold is applied and the leading edge times and time over threshold values are recorded as well as the amplitudes.

6.4   Muonic background

The atmospheric background used in this analysis was generated by AMASIM. The production versions v004 and v005 of the Zeuthen Monte Carlo effort for the AMANDA collaboration were used. They simulate atmospheric muons with an energy spectrum of $E^{-2.67}$ [Boziev et al., 1989]. For further details see [Biron, 1999].

6.5   Monopole generation

Figure 6.2 sketches the generation of monopoles. They are generated isotropically on a disk with 400 m radius which is located 500 m away from the detector centre. The disk moves isotropically in azimuth and in the cosine of the zenith angle with respect to
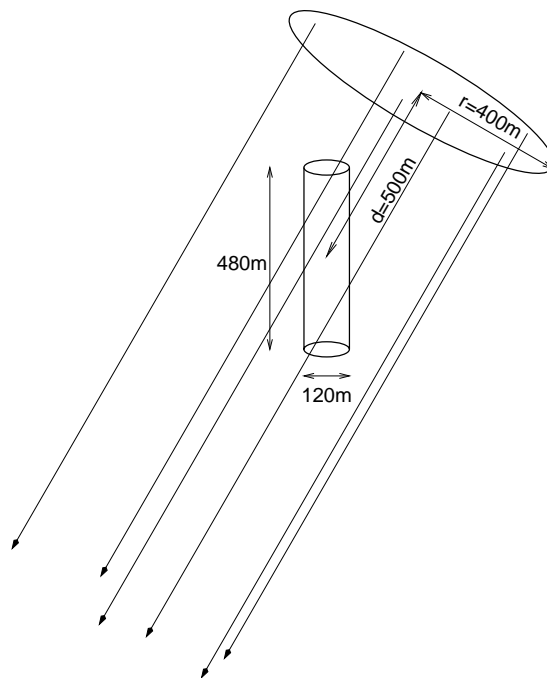
Figure 6.2: Monopoles are generated on a plane with 400 m radius in a distance of 500 m from the detector centre. Their track length is assumed to be infinitely long.

the long axis of the detector. The generated tracks are fed into AMASIM to yield the response of the detector. This response can be expressed by the trigger efficiency η_{trigg} which is given by the ratio of triggered to simulated events. In the limit of an infinite generation disk the efficiency will go to zero, however the product of generation area and trigger efficiency should reach a constant value A_{trigg} asymptotically.

In order to verify this, monopoles were generated on disks with increasing diameter and the trigger area A_{trigg} was calculated. If the size of the generation plane is too small, then the trigger area will increase with the size of the generation area. If the size becomes too big, the simulation accesses the photon tables outside their validity range. The result is given in table 6.1 showing that the effective area becomes constant at about 400 m. The efficiencies and trigger areas for other values of β are shown in table 6.2. Figure 6.3 shows the relative number of events which triggered the detector as a function of the distance of the track from the detector centre. For every value of β, the area is normalised to the trigger efficiency and thus, because the number of triggered events is the same, to the same number of input events (events passed to AMASIM, regardless of the trigger).

r_{gen}/m	n_{in}	n_{trigg}	η_{trigg}	$A_{trigg} = \pi r_{gen}^2 \times \eta_{trigg}/1000 \text{ m}^2$
100	1600	1600	1.00	31
200	1600	1600	1.00	125
300	1653	1600	0.97	274
400	2395	1600	0.67	336
500	3769	1600	0.43	333
600	5466	1600	0.29	331

Table 6.1: Trigger efficiencies and trigger areas versus the generation plane areas for $\beta = 1$ monopoles.

β	n_{trigg}	n_{proc}	η_{trigg}	$A_{trigg}/1000\text{m}^2$
1.0	7200	10882	0.66	333
0.9	7200	12134	0.59	291
0.8	7200	16192	0.45	224

Table 6.2: Trigger efficiencies and effective areas for several values of β.
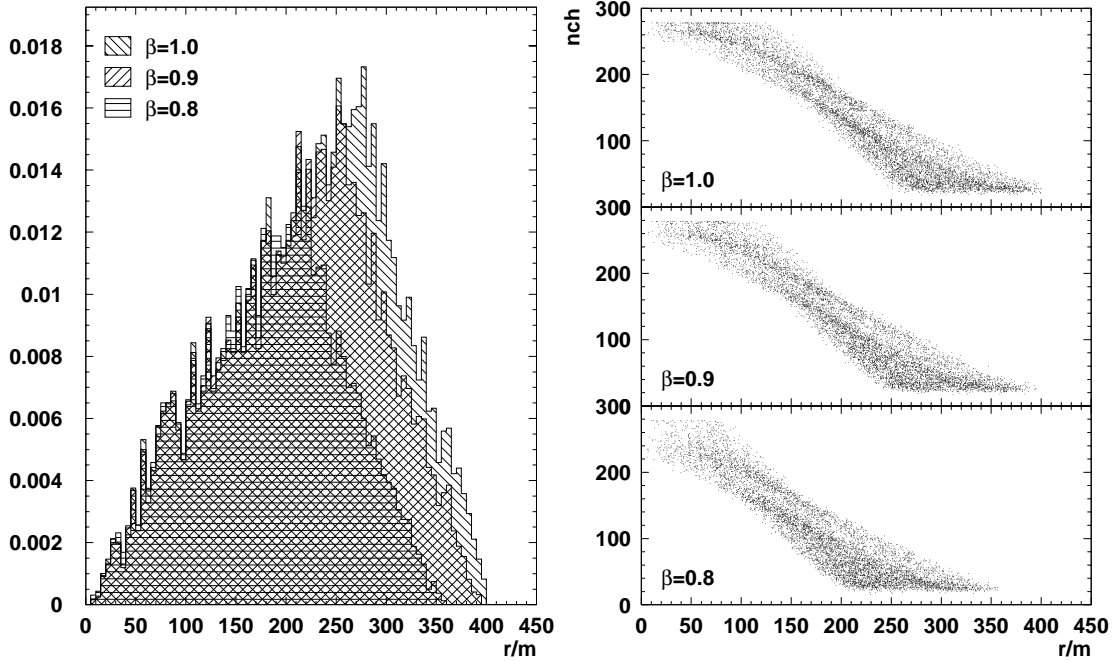
Figure 6.3: Left: fraction of triggered events as a function of the distance between the generated track and the detector centre. Each histogram is normalised to the trigger efficiency η_{trigg} from table 6.2. Right: number of channels as a function of distance of the track from the detector centre.
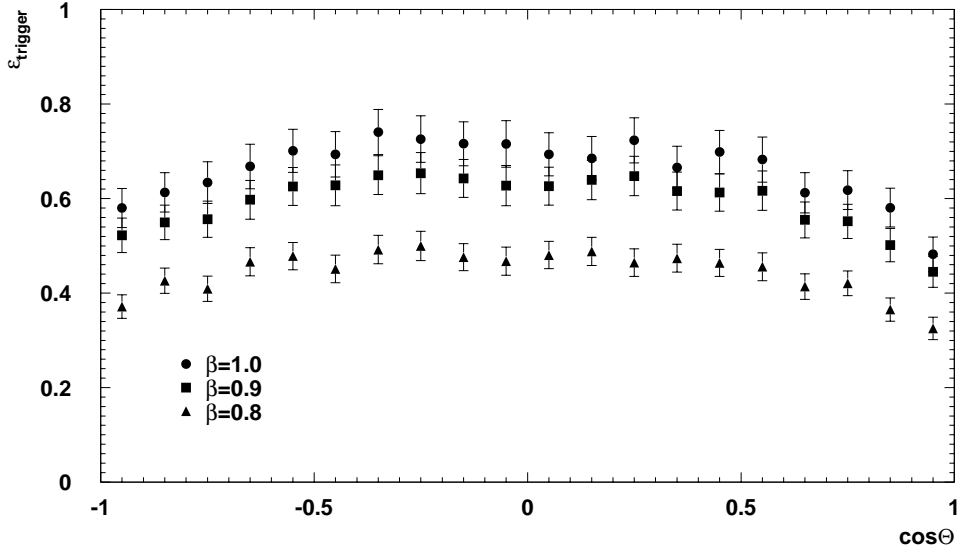
Figure 6.4: Trigger efficiency $\epsilon_{\text{trigger}}$ in dependency of the generation angle. Since the detector is tall rather than wide, the efficiency decreases for vertical tracks.

As the events were generated on a plane with constant density, the fraction dN of events generated on a ring between the radii r and $r + dr$ is $dN = 2\pi r dr$, one expects a linear relation between dN and r, which is indeed observed in figure 6.3 (left).

Up to a certain radius (approximately 200m, see table 6.1 the efficiency is 1 and then decreases rapidly. The position of the peak arises from the fact that the detector ends at heights of ± 200 m, with the visibility extending beyond the detector bounds for β close to 1. As the endpoint of the distribution for $\beta = 1.0$ reaches 400 m smoothly, it can be said that the size of the generation plane is sufficient. The number of hit channels as a function of the distance from the detector centre is shown in figure 6.3 (right). This suggests a multiplicity cut in order to reduce the number of tracks passing outside the detector which are probably difficult to reconstruct.

As the width of the detector is only a third of its height, the trigger efficiency will vary with the generation zenith angle. For horizontal tracks, the detector will cover more of the generation area than for vertical tracks. Indeed, the trigger efficiency at very large or small zenith angles ($\cos \Theta \approx \pm 1$) drops to about 70% compared with horizontal tracks, see figure 6.4. In appendix C it is shown that the acceptance is more uniform for a cube-shaped detector. As most of the OMs have their sensitive area facing down, the trigger efficiency is lower for down going ($\cos = +1$) than for up going ($\cos = -1$) tracks.

A simulated $\beta = 1.0$ event is shown in figure 6.5.

Color displays: LE   Primary Channels

3020   10
3110   12
3199   14
3288   17
3378   28
3467   30
3557   33
3646   25
3735   23
3825   13
3914   7
4004   9
4093   2
4183   4
4272
4361   1

Size displays: ADC   Size scaling: Lin

<6   <10   <14   <18   <22   <26   <30   <34

<38   <42   <46   <50   <55   <59   <63   <67

No external geometry file is opened.
Detector: amanda-b-10, 10 strings, 303 modules
Data file: standard input
Displaying MC event 104 from run 400
Created yr/dy: 1970/1
Created yr/dy: 1970/1
Before cuts: 228 hits, 228 OMs
After cuts : 228 hits, 228 OMs
1   Muon
                          x   y   z
Vertex pos.   :   120.6 -387.9 -297.8 m
Stopping pos.: -1251.6 7078.2 6211.8 m
Direction   : -0.13722 0.74661 0.65096
Length   :   10000 m
Energy   :   10000 GeV
Time   :   1722.820000 ns
Zenith   :   130.6°
Azimuth :   280.4°

Figure 6.5: A simulated $\beta = 1.0$ monopole passes through the B10 array.

Chapter 7

Reconstruction

7.1 Introduction

Particle tracks in AMANDA are reconstructed from the arrival times of photons at the optical modules. In order to perform a reconstruction, one makes an assumption which connects the time and amplitude information provided by the OM to a hypothetical particle track. The assumption is qualified by a likelihood and parameters of the track are varied in order to maximise it. A simple model will be discussed in section 7.5.

Not all the hits registered in an event are caused by a traversing particle. Dark currents in the PMT and radioactivity in the glass spheres of the OM's may cause random hits.

7.2 Pre-processing

Before the actual reconstruction, the data pass through several pre-processing steps, which are different for experimental and Monte Carlo data. E.g., since AMANDA is run in coincidence with external experiments such as SPASE, all events triggered by outer detectors are rejected to make a comparison to Monte Carlo possible.

Since the monopoles searched for are bright events a cut is made and all events which have a channel multiplicity below 100 OMs are rejected. This cuts down the event rate from $\sim$100 Hz to $\sim$0.04 Hz.

Some modules have to be removed from the analysis, whether it is because calibration constants are not known or because the OMs themselves are non-operational. This is done for both Monte Carlo and experiment.

As described in section 4.5, eight leading and trailing edges are recorded per channel but only one amplitude is measured. The ADC gate is set such that it samples between 2000 ns before and 2270 ns after the recorded trigger time. It may happen that during this time multiple hits are recorded and it is then not clear which of these have to be assigned to the amplitude. Several options are possible: One could assign the first hit, the hit with the largest time over threshold or all hits to the amplitude. However, it has been

58

found [Biron et al., 1999] that the results do not depend strongly on the choice. Here, the amplitude was assigned to the hit with the largest time over threshold. All hits outside the ADC gate will be discarded later.

The ADCs in this experiment are limited to a maximum output of 2048 counts for strings 1-4 and to 4096 counts in strings 5-10 (see figure 7.1). Thus, in Monte Carlo all amplitudes above that value were truncated to this limit.
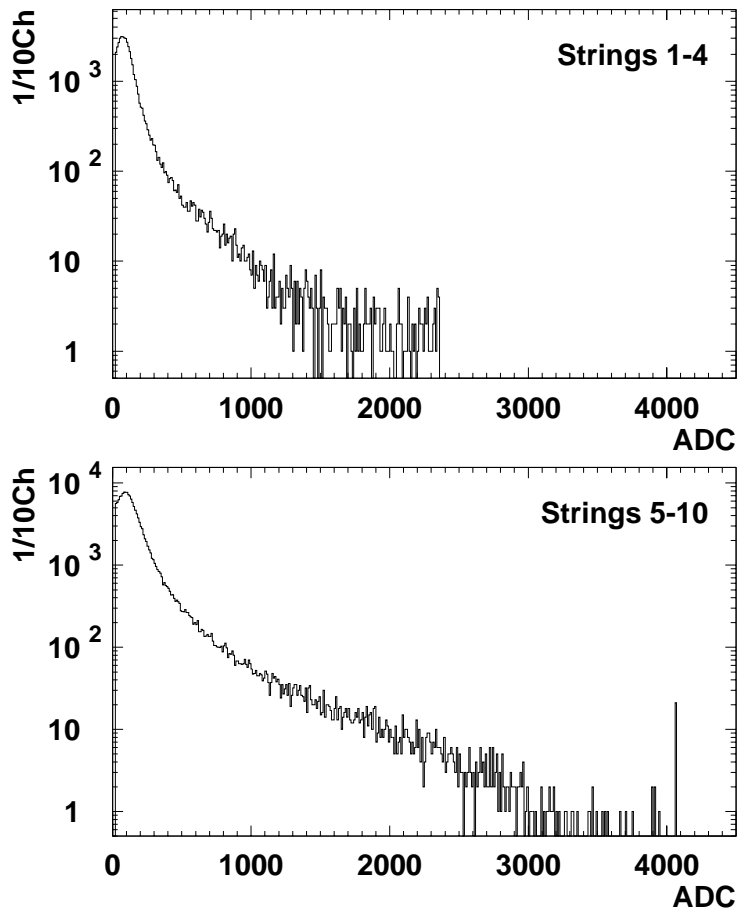
Figure 7.1: Experimental raw amplitudes spectra after assignment of ADC and cutting noise for strings 1–4 and 5–10.

After this, electronics noise is reduced by applying a threshold on the ADC values. The Monte Carlo uses the un-delayed SWAMP output for both amplitudes and timing, whereas in the experiment the amplitudes are formed from the delayed output, which is roughly a factor three lower in amplitude than the un-delayed. Thus, in the detector setup the threshold is fixed at 20 ADC counts but at 60 ADC counts in Monte Carlo.

7.3 Trigger peak and time shift

A histogram of the un-calibrated leading edge times of all OMs in the experiment is shown in figure 7.2. The main features are still apparent after time calibration, but the trigger peak at 22000 ns is smeared out when the individual cable times are subtracted. The distribution consists of three contributions: first the noise hits between 0 and ~ 19 μs, followed by the leading edges caused by a particle between 19 μs and ~ 26 μs, and finally the after pulse region beyond 26 μs. In Monte Carlo, the trigger time is set to arbitrarily to zero and as a consequence most of the leading edges are negative. Because the reconstruction algorithm expects the times to be positive, they are shifted; in the experiment to the left by 19 μs and in Monte Carlo to the right by 4 μs. This puts the left shoulder of the trigger peak close to time zero. Then a window with a width of 4.5μs is applied, rejecting pure noise and after-pulses outside the trigger peak.
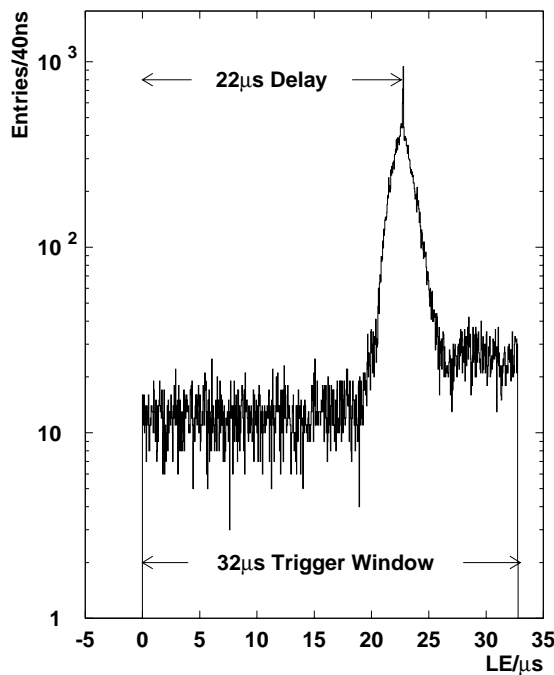
Figure 7.2: Distribution of un-calibrated leading edges in experiment.

7.4 Hit cleaning

Hit cleaning is used to maximise the information content of the hits, implying that hits containing no information are rejected. First, there are still electronics noise hits even after the 4.5μs application. Secondly, the time information of photons travelling a long way from the track to the module will be perturbed by scattering.

A cut on the time over threshold value (TOT) is applied at 125 ns to reduce cross talk and a cut on the amplitude at 0.1 photo electrons is used to suppress dynode noise in the PMT. The assumption is made that the crosstalk pulses will be shorter than regular pulses. As the muonic background simulation used at that time had only coaxial cables available, the cut is tightened by demanding time over threshold values above 275 ns to take into account the lower broadening of the signal in the twisted pair cable. In the monopole signal simulation, coaxial and twisted pair cables were treated separately, resulting in a single TOT cut above 125 ns.

A large part of the strongly scattered photons are rejected by two additional requirements: for each hit, another hit has to be present within a time window of 500 ns and a radius of 100 m, and hits isolated from any other hit in time by more than 400 ns are rejected.

7.5 Line fit

After the event has been cleaned from non-relevant hits, a reconstruction can be made. The particle propagates along its track and emits photons which hit modules at position $\vec{x}_i$ at times t_i. The position of the particle can be approximated by

$$\vec{X}(t) = \vec{X}_0 + v_{\mathrm{LF}} \cdot \vec{e} \cdot t \tag{7.1}$$

where $\vec{X}_0$ is an arbitrary point on the particle trajectory $\vec{e} = (\cos\phi\sin\Theta, \sin\phi\sin\Theta, \cos\Theta)$, parametrised in zenith Θ and azimuth ϕ. $\vec{X}_0$ can also be written as $\vec{v} \cdot t_0$ ($\vec{v} = v_{\mathrm{LF}} \cdot \vec{e}$). Here, $\vec{X}_0$ is chosen as the point closest to the origin of the track, i.e. the generation point. In order to determine the parameters v_{LF}, Θ and ϕ one compares the particle position predicted by equation 7.1 with the times t_i measured at the positions $\vec{x}_i$ of the modules, setting up a χ^2 function:

$$\chi^2 = \sum_{\mathrm{hit\ modules}} w_i \cdot (\vec{x}_i - \vec{X}(t_i))^2 \tag{7.2}$$

where w_i is a weight for every single hit. It can be set to a power α of the amplitude a_i in a hit, thus $w_i = a_i^\alpha$. Minimising χ^2 yields an analytical solution:

$$\vec{v} = \frac{\langle t\vec{x} \rangle - \langle t \rangle \langle \vec{x} \rangle}{\langle t^2 \rangle - \langle t \rangle^2} \tag{7.3}$$

$$\vec{X}_0 = \langle \vec{x} \rangle - \vec{v} \cdot \langle t \rangle \tag{7.4}$$

where the mean values $\langle O \rangle$ are calculated as $\langle O \rangle = \sum w_i O_i / \sum w_i$. This line fit [Stenger, 1990] works best in case of a very densely instrumented detector or if only modules close to the track had been hit. As soon as there are modules hit far away from the track, the accuracy declines due to scattering of photons. This is shown in figure 7.3 by plotting the angular mismatch vs. the fraction of direct hits. A direct hit is defined here as a hit for

which the impact of the photon takes place between -15 ns and 75 ns with respect to the expectation from straight light propagation. As the fraction of direct hits exceeds 0.1, the angular mismatch is reduced. Thus, to make the line fit work, one has to find a method to increase the fraction of direct hits. Direct hits will occur in modules close to the track which in turn are exposed to brighter light.
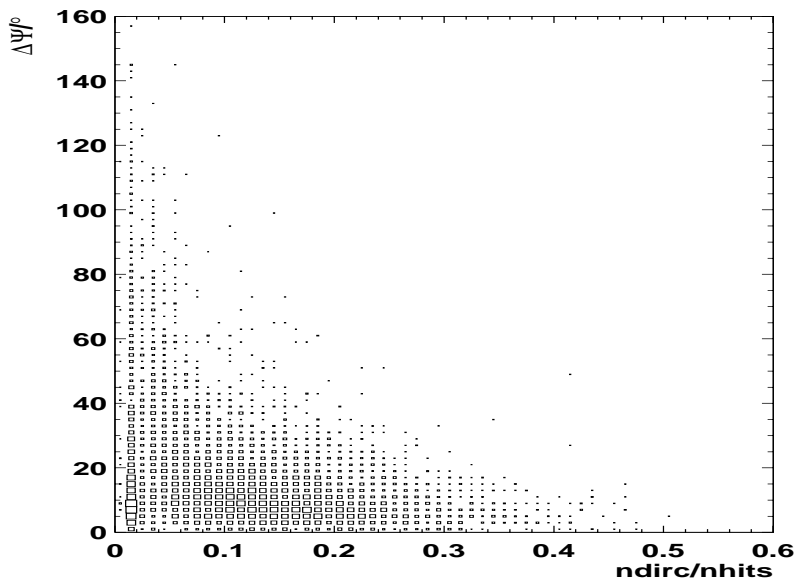
Figure 7.3: The angular mismatch $\Delta\Psi$ between generated and line fit reconstructed track vs. the fraction of direct "C"hits (time difference between expected and actual arrival time is between -15 ns and 75 ns) in muon simulation data.

7.6 Pulse height and hit quality

The relation between amplitude and residual for a $\beta = 1$ monopole simulation is shown in figure 7.4. One sees that the hits with amplitudes below 1.5 photo electrons are the ones with a very large residual. A possible remedy to this is the exclusion of low amplitude hits or the introduction of a weight to give the more meaningful (i.e. with a low residual) hits more importance in the fit. Since for hits of more than one photo electron the chance that the first p.e. is less delayed than the average one photo electron hit, time residuals are smaller for large amplitudes. Thus, a line fit making use of amplitude information will be applied. It will be robust and also be able to handle particles with speeds below $\beta = 1.0$.
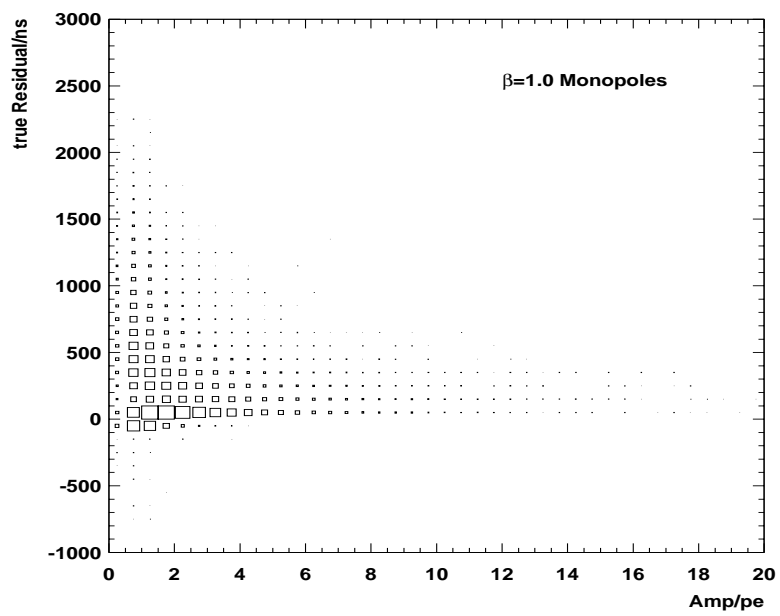
Figure 7.4: Time residual of hits vs. amplitude for monopole Monte Carlo.

Chapter 8

Analysis

As it was discussed in chapter 2, the prominent feature of a monopole passing through AMANDA is its large light output, resulting in a high number of hit modules in the detector. High multiplicities can also be caused by energetic muons or muon bundles which are produced in atmospheric reactions. Thus, the Earth will be used as a shield against these particles and the search for monopoles will be restricted to the lower hemisphere (section 8.2). Nevertheless, the upper hemisphere will be studied, too, in section 8.3.

Searching particles in different hemispheres requires that the reconstruction of tracks works well, so that e.g. no downward going tracks are reconstructed as up going. The way to avoid this is the introduction of requirements on suitable observables ("cuts").

Some naming conventions are in order now. The zenith angle Θ is 0 for a particle moving downward, i.e. towards the centre of the Earth. The term "upper hemisphere" will refer to particles coming from angles Θ between $0° \leq \Theta \leq 90°$. The "lower hemisphere" is defined by zenith angles larger than $90°$. The monopoles which are to be detected will be referred to as the "signal". Everything which is not a monopole will be called "background". The background consists primarily of downward moving particles generated in atmospheric reactions. If these downward moving particles are reconstructed as upward-moving, they will be called "fakes".

8.1 Cuts and fake estimation

In this section, a method will be proposed and applied to get reasonable background predictions from medium statistics samples and to handle cross-talk effects present only in the experimental data.

In order to obtain a clean signal event sample, cuts have to be applied. This means that some observables or cut parameters C_i have to be bigger/smaller than some cut value a_i. Cuts should be chosen in such a way that they can reduce the appearance of fakes in a given data sample. It is to be expected that the application of several cuts is more efficient w.r.t. this task. Cuts will have to be "non parallel" in this case. This means that

after the application of one cut, the application of another results in a further reduction of fakes in the sample.

E.g., if the two cuts $C_1 > a_1$ and $C_2 > a_2$ yield a relative rate of fakes in the background $f_{\mathrm{BG}}(a1)$ and $f_{\mathrm{BG}}(a2)$, then the two cuts are independent if their combination yields a fake appearance of $f_{\mathrm{BG}}(a_1, a_2) = f_{\mathrm{BG}}(a_1) \times f_{\mathrm{BG}}(a_2)$. Here, the relative rate of fakes f_{BG} is defined as the number of fakes passing a cut divided by the total number of fakes. An example of this is shown in figure 8.1.
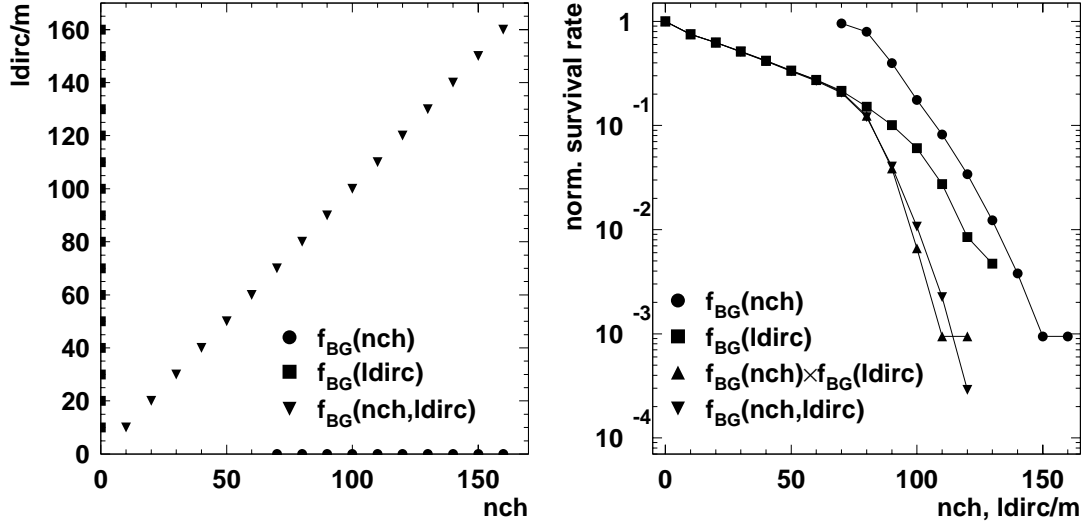
Figure 8.1: Left: points in $nch-ldirc$ space along which the fraction of background events f_{BG} is evaluated. Right: fraction of fake events f_{bg} surviving a cut on nch, the number of hit channels and $ldirc$, the maximal distance between direct hits in the time window (-15 ns...75 ns).

The two cut parameters involved are nch, the number of hit channels and $ldirc$. The latter is obtained by the following method: all hits with a time residual with respect to a fitted track between -15 ns and 75 ns are projected on this track. Then the projected distance between the first and the last hit on this track defines the value of $ldirc$. The figure shows the fraction of fakes surviving a cut on one ($f_{\mathrm{BG}}(nch), f_{\mathrm{BG}}(ldirc)$) or two ($f_{\mathrm{BG}}(nch, ldirc)$) parameters. Additionally, they show the product of the fraction of the two single cuts, i.e. $f_{\mathrm{BG}}(nch) \times f_{\mathrm{BG}}(ldirc)$. For the parameters nch and $ldirc$, the cut values were separately varied between 0 and 160 and 0 and 160 m respectively. For the combination of cuts, both values were varied simultaneously, i.e. along a line in $nch-ldirc$ space . The independence of the two parameters nch and $ldirc$ is inferred from the good agreement between $f_{\mathrm{BG}}(nch, ldirc)$ and $f_{\mathrm{BG}}(nch) \times f_{\mathrm{BG}}(ldirc)$. From this one concludes that it is reasonable to use these two parameters as "non-parallel" cuts.

As a next step, the question has to be considered as how the cut values should be chosen. Two competing demands have to be satisfied: on the one hand, fakes from the

background have to be rejected, on the other hand the amount of signal passing through the cuts should be high, implying a weak application of the cut. As the cuts will be developed on a small sub-sample before applying them to the whole available sample, one has to be able to predict how many background/fake events are left after application of cuts. A schematic example is given in figure 8.2.
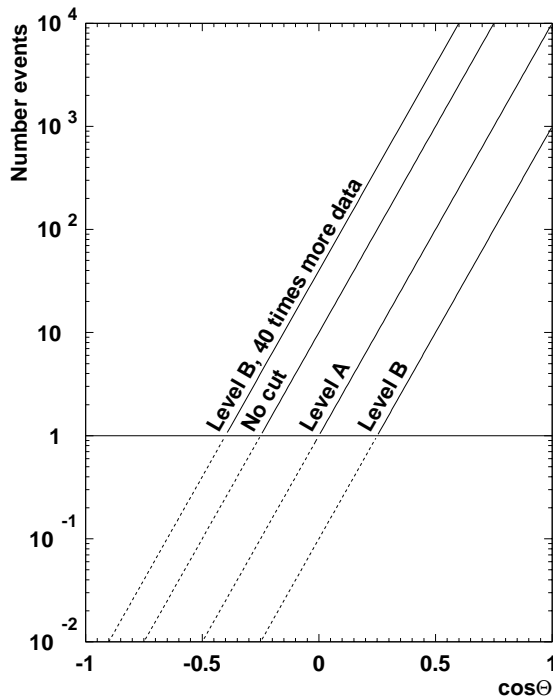
Figure 8.2: An idealised zenith angle distribution.

Let us assume that particles hitting the detector from above ($\cos \Theta > 0$) are reconstructed, yielding the spectrum shown. These particles represent the background. A fake is identified as an event with $\cos \Theta < 0$. Additionally it is assumed that the number of signal events coming from below ($\cos \Theta < 0$) is small compared with the number of fakes. The distribution of a small sample is given by the "no cut" curve. Some fakes are present. As cuts are applied ("Level A", "Level B"), the fakes disappear. "Level B" is a bit more conservative, allowing for some uncertainties in the reconstruction of the data. However, as more data are processed ("Level B, 40 time more data"), fakes start appearing again. It would be desirable to know a function

$$f_{\mathrm{BG}}(C_1 > a_1, \ldots, C_i > a_i, \ldots, C_n > a_n) \equiv f_{\mathrm{BG}}(a_1, \ldots, a_n) \qquad (8.1)$$

which gives the number of background/fake events where n is the number of cut parameters. The condition that the cut parameter C_i should be larger than the cut value a_i ensures that the f_{BG} falls monotonously with increasing a_i which will help in modelling

of the function later. Thus, what is required are the fitting and extrapolation of a multi-dimensional function. Alternatively, this multidimensional problem can be reduced to a one dimensional by parametrising the cut values a_i by a single variable t, e.g.

$$f_{\mathrm{BG}}(a_1(t), \dots, a_n(t)) \equiv f_{\mathrm{BG}}(t). \tag{8.2}$$

However, here the result would depend on the path given by the $a_i(t)$. Returning to a multidimensional function, one is confronted with the problems of which function to use for the fit and that the derivatives in all variables and their combinations have to be known [Press et al., 1992].

These problems can be avoided by using a neural net as a means of fitting and extrapolating, see section E.5 in the appendix. The net will be trained with the cut values which yield the number of fakes present in the background sample. From training with a small sample and applying the result of the net to a larger sample ("cross validation", see figure 8.14 and table 8.5) the validity of the procedure will be tested.

8.2   Search across the lower hemisphere

8.2.1   Reconstruction and cut parameters

Since most of the background originates from the atmosphere above AMANDA, it is more efficient to restrict the search for monopoles to the lower hemisphere. The conditions under which a monopole above a mass of 10^{11} GeV can traverse the Earth have already been discussed in chapter 2. As many modules are hit in the events selected for the analysis, a line fit will give a reasonable direction information, if not too many bad hits caused by delayed light are present. The four versions of the fit used are:

1. Use all the modules left after cleaning, take all of them into account with the same weight. This fit will be referred to as ID 1 or nw.

2. As ID 1, but now the hits are weighted by their amplitudes. This is ID 2 or w.

3. After hit cleaning, restrict to hits with an amplitude above the equivalent of one photo electron. Do not weight. Abbreviated as ID 3 or $> 1pe, nw$.

4. Like ID 3, but additionally weighting is performed. As shorthand, ID 4 or $> 1pe, w$ will be used.

The deviation $\Delta\Theta$ between generated and reconstructed zenith angle for the atmospheric muon simulation is shown in figure 8.3. As a measure of the overall fit accuracy, the mean value $\langle\Delta\Theta\rangle$ is chosen. As amplitudes are involved, one has to take into account their uncertainty as discussed in chapter 5. Three values of κ of the calibration prescription 5.3 are chosen to cover every possible scenario, although this is meaningful only for fits ID 2, 3, 4 which make use of the amplitude information. It is seen that the
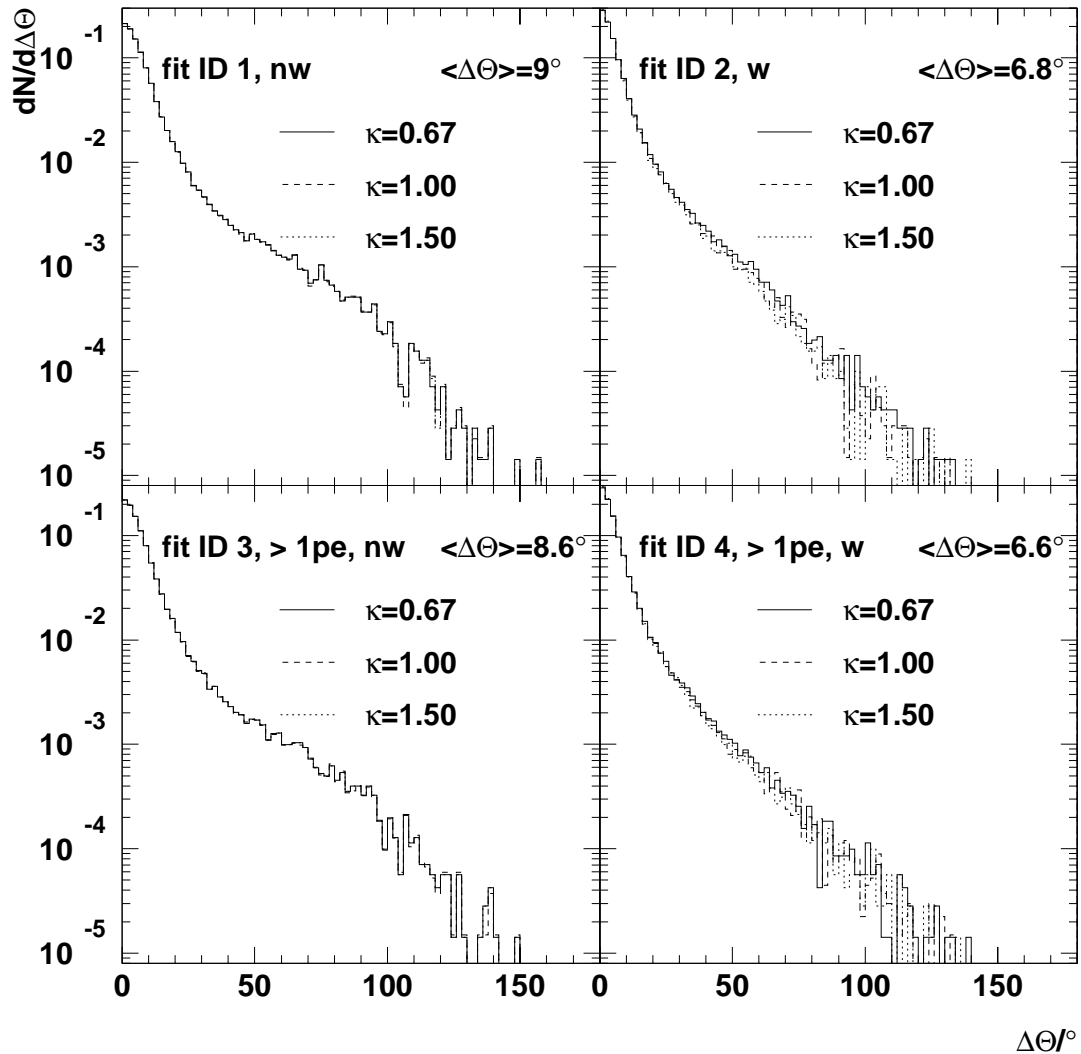
Figure 8.3: Distribution of the zenith mismatch for various fits in muon background simulation.

introduction of amplitude weighting (fits ID 2, 4) improves the fit performance and yields a lower average angular error. The calibration variations are also of minor influence on the fitted zenith angle.

The effect of weighting is seen even better in the monopole signal simulation. Figure 8.4 shows the reconstructed angle vs. the generated zenith angle for each event. When no weighting of amplitudes is performed (ID 1), many events are reconstructed into the wrong hemisphere. This situation is improved considerably by weighting (ID2, ID 4). Due to the shape of the detector, the reconstruction algorithm tends to draw the tracks to the vertical, leading to the sinusoidal distribution of the scattered points in figure 8.4.
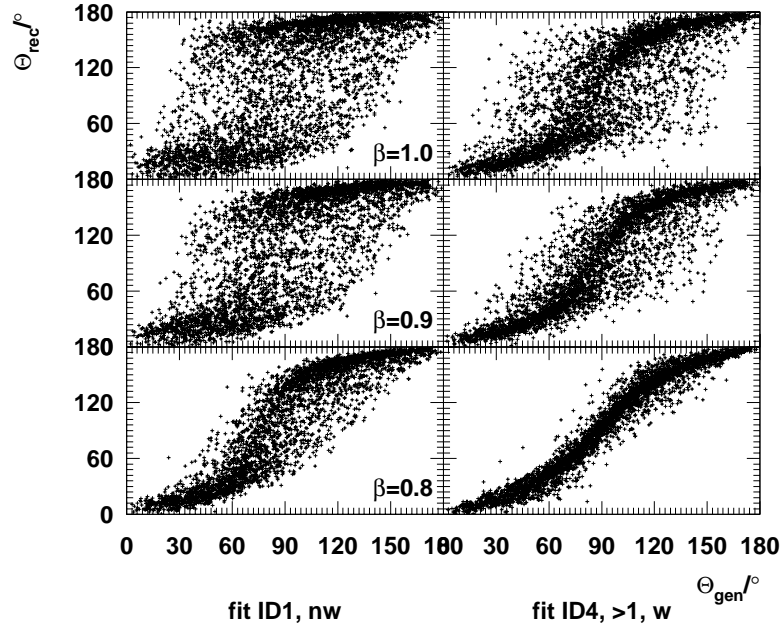
Figure 8.4: Reconstructed vs. generated zenith angle for different fits and speeds in monopole simulation.

It is interesting to note that the line fit gives a better result for lower values of β. The reason is that for smaller β the number of hits decreases and the ratio of the number of direct hits to the number of all hits increases. As the line fit does not take into account scattering it is perturbed stronger, the more delayed hits contribute – i.e., for $\beta = 1$ more than for $\beta = 0.8$. In appendix C it is shown that a cube shaped detector leads to better results, even without weighting.

Figures 8.3 and 8.4 show that additional criteria have to be found in order to determine whether the fit is correct or not. Since the main concern here is the search for upward going tracks, "correct" means that the track is reconstructed into the right hemisphere.

Number of hit channels

The first and most simple observable is the number of channels. The channel multiplicities for data from five days are shown in figure 8.5. Experiment is different from background Monte Carlo in two respects, namely in the low ($nch < 50$) and high ($nch > 100$) multiplicity region. The discrepancy in the lower region can be explained as follows. The (un-calibrated) leading edge distribution of the hits is shown in figure 8.6. If this distribution is compared to the corresponding distribution of the other events (cf. figure 7.2 in chapter 7), one sees that there is a large fraction of hits after the end of the ADC gate at 25230 ns. As mentioned above, all hits outside the ADC gate will be discarded,

leading to a lower value of *nch*. Because often all eight TDC channels were filled, this phenomenon is probably an electronic artefact. For multiplicity values between 50 and
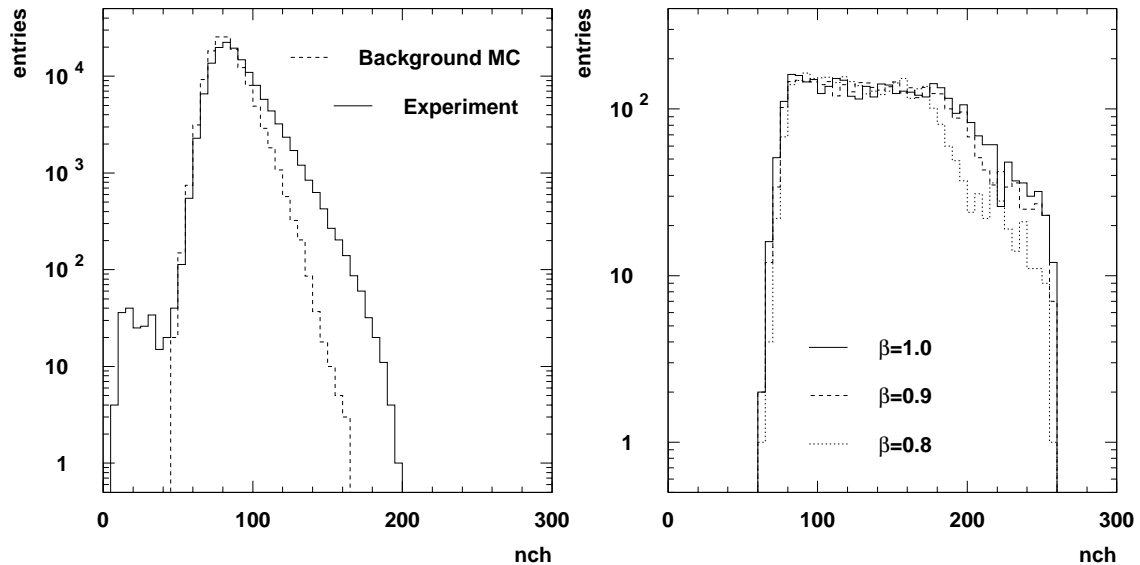
Figure 8.5: Channel multiplicities in experiment, background Monte Carlo (left) and signal Monte Carlo (right) after hit cleaning. Signal Monte Carlo starts at multiplicities of 60 due to using two pulse shapes and doing thus a different TOT cleaning, see section 7.4.

90, the distributions in experiment and Monte Carlo are in good agreement. Above 90, there is an excess in experiment.

Two different generators It was thought that this discrepancy is caused by using the Basiev atmospheric muon generator [Boziev et al., 1989], which only generates protons as primary particles. However, using the Corsika [Heck et al., 1998] generator, which takes into account all the elements up to iron, shows that this was not the only reason. The comparison of the raw channel multiplicity distribution is shown in figure 8.7. One sees that there is only an excess (factor 2-3) at high multiplicities in the case of Corsika.

Crosstalk Another possibility to explain the higher multiplicity is crosstalk, which can occur in the cables leading from the module to the surface or in the recording electronics [Wiebusch, 1998a, Hanson, 2000]. The crosstalk signals in the cable would arrive at the surface within a narrow time window. We used the noise hits in the OM present before the trigger peak ($0...19\ \mu$s in figure 7.2) as a signal source for crosstalk. For each recorded event, the hits were ordered by their channel number. Then, channel pairs (i, j) with $i \neq j$ were selected for which the time difference un-corrected for cable delay was less than 20 ns. If such a pair is found, an entry is made into a two-dimensional histogram at column i and
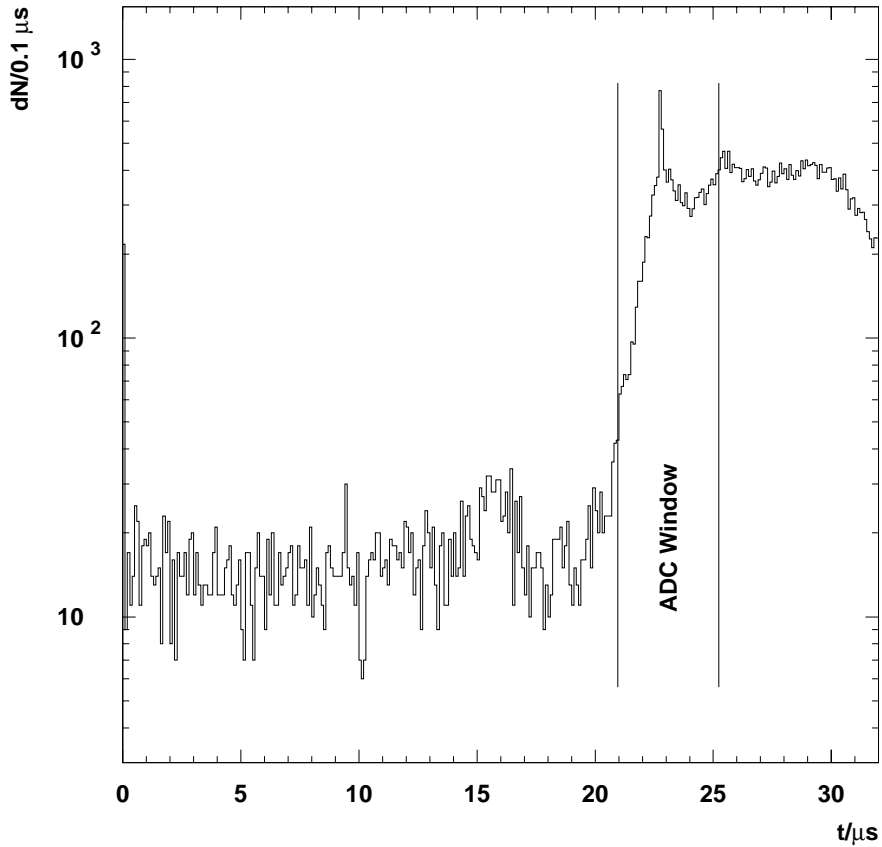
Figure 8.6: Raw leading edge distribution for events in experimental data which have a OM multiplicity below 50 after cleaning in figure 8.5. In contrast to figure 7.2 in chapter 7, the contribution outside the ADC window ($t > 25230$ ns) is very large. The number of hits at $t = 0$ is high compared to figure 7.2. Note also the bump centred around 16 μs.

line j, where $i < j$. The result is shown in figure 8.8. The number of entries in each plot was chosen such that the density of entries in the crosstalk free region (strings 1-4) was the same for experiment and atmospheric muon simulation. If a channel has a high noise rate, (like channels 255, 259 and 260 with rates of 170 kHz, 30 kHz and 20 kHz respectively,) then there will always be an entry in the corresponding line/column, depending whether the channel having a hit at the same time has a smaller/bigger number. This explains the horizontal/vertical structures present both in Monte Carlo and experiment. A feature present in experiment only is the strong occupation along the diagonal, indicating a correlation of hits in neighbouring channels.

Although there is a strong discrepancy between the overall nch distribution in experiment and simulation, it was found that the description of fake events is in better agreement for the fit using amplitude weighting (ID 4), see figure 8.9. This justifies the application
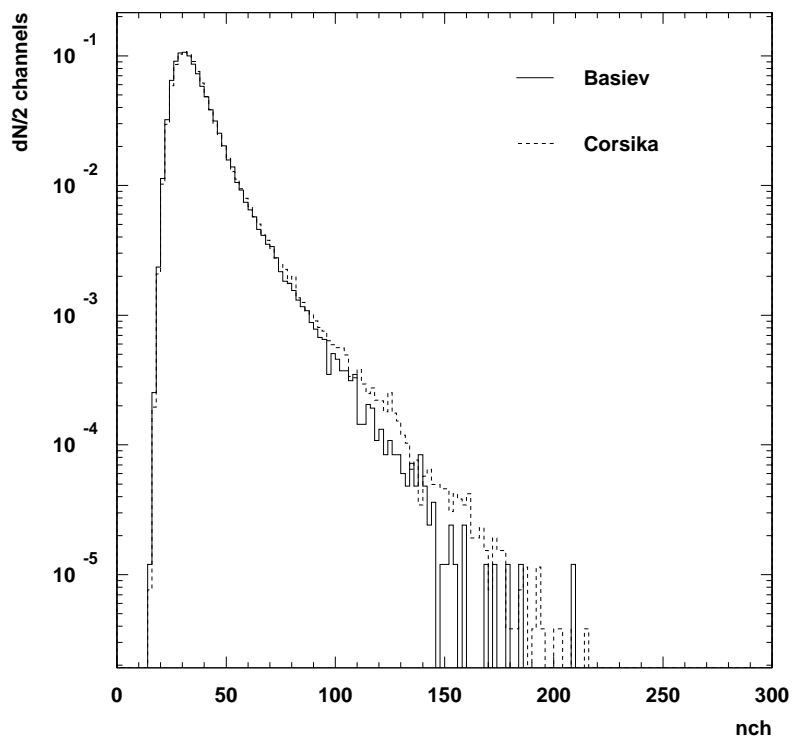
Figure 8.7: Raw channel multiplicities as obtained from Basiev and Corsika generators.
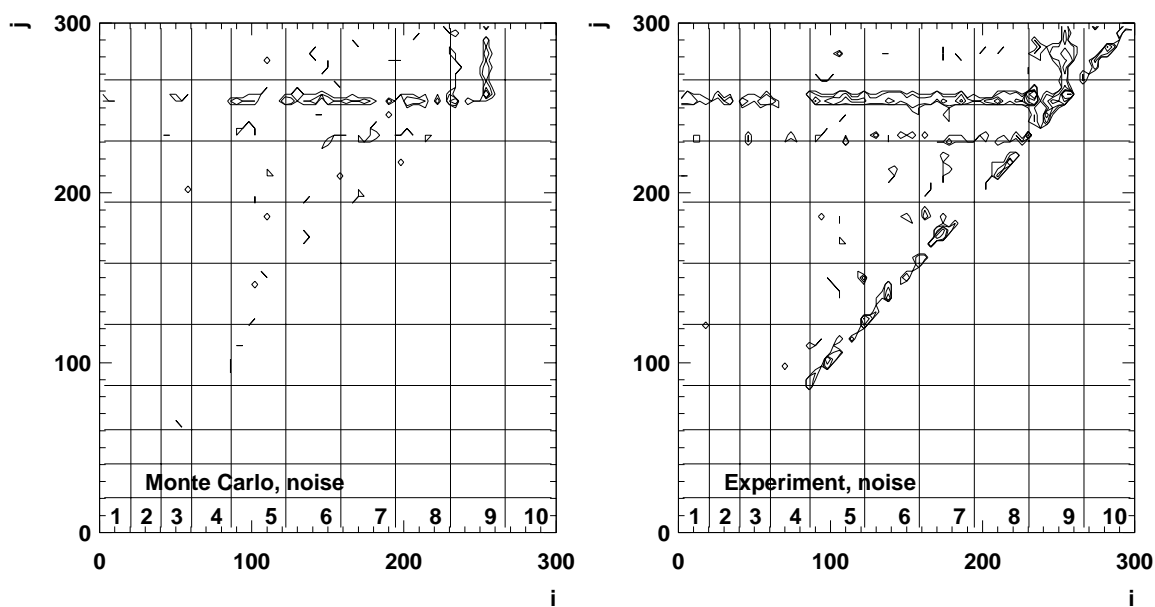
Figure 8.8: Graphical representation of the crosstalk matrix, i.e. the number of hits induced from one channel to another within 20ns (uncalibrated times).

of an *nch* cut in order to reject events which are reconstructed wrongly as coming from below, i.e. with a zenith angle $\Theta > 90°$. The influence of the amplitude calibration in case of the ID 4 fit is small.

However, as the cuts on *nch* will be set using experiment and crosstalk is not included in the monopole simulation, the simulated channel numbers will be too low in comparison, leading to an underestimation of signal. If an upper limit is to be determined, this mechanism will add conservatism to the result. In the case that there is a signal in this region, it would be lost. Thus, it is important to keep the region in *nch* where events are excluded small, as will be done in section 8.2.2.
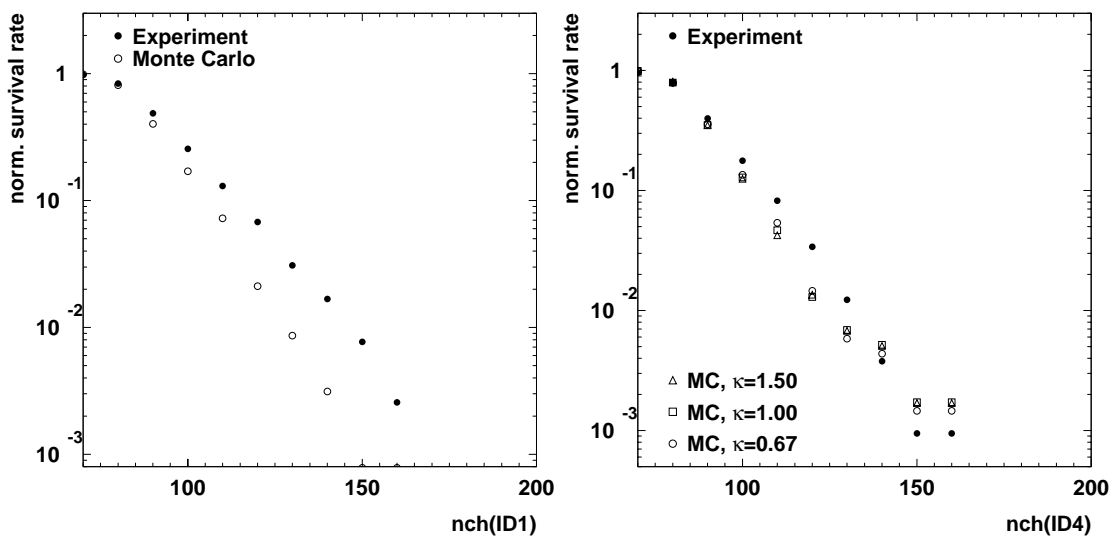
Figure 8.9: Relative fake rates in experiment and simulation as a function of a cut on *nch*. Left: fakes generated by fit ID 1 (*nw*), right: fakes generated by fit ID 4 ($> 1pe, w$).

The generation of a monopole signal with a Monte Carlo program results in the multiplicity distribution shown in the right plot in figure 8.5. The cutoff at ~ 260 on the plot is due to the removal of 45 modules from the analysis, leaving a maximum number of 302-45=257 modules. The relatively slower and thus less bright $\beta = 0.8$ monopoles show a steeper drop towards higher multiplicity.

The difference in the lower cutoff between background and signal is due to using different pulse shapes in signal and background simulation. The use of one pulse shape for all channels in the muon simulation is due to the fact that at the time of its generation only one pulse shape was available. In the background simulation, coaxial cables are used only and the twisted pair cable behaviour is emulated by a different TOT cut. The signal Monte Carlo uses coax cables for strings 1 to 4 and twisted pair cables for strings 5 to 10, leading to a different effect of the TOT cut.

Optical module sensitivities Studies varying the OM sensitivities show that this parameter has a great influence on the *nch* distribution [Leuthold and Wissing, 2000]. All three effects contribute towards the discrepancy in the distribution between simulation and experiment. It is however not simple to disentangle the three effects from each other and a different approach (cf. sections 8.2.2 and 8.3) will be chosen.

Extension of direct hits along the track

Since the line fit algorithm does not handle delayed hits well, one would like to select events with a long lever arm with hits close to the track. This can be done by using the so called *ldir* parameter which was introduced in section 8.1. A high value of *ldirc* will imply a long lever arm. Naturally, as the detector is tall rather than wide, a strong requirement on this variable will enhance the acceptance of vertical tracks while horizontal tracks will be suppressed. The behaviour of this variable in experiment and muon Monte Carlo is shown in figures 8.10 and 8.11. Each plot shows the overall distribution of the
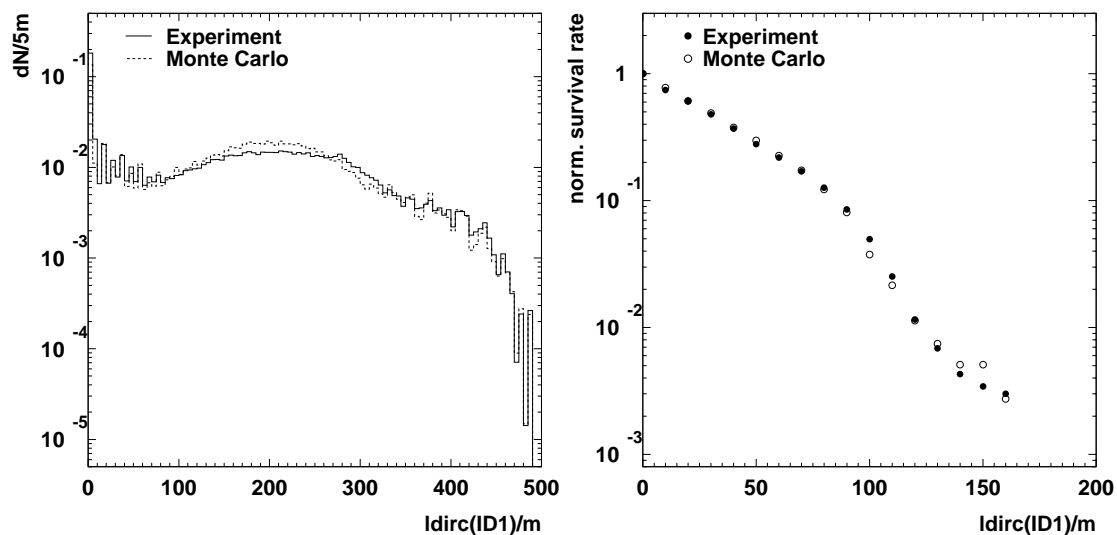
Figure 8.10: *ldirc* based on fit ID 1. Left: distribution of *ldirc* for fit using all hits. right: Relative fake rate in dependence of *ldirc*.

cut parameter (left plot) and its power to reject upward reconstructed fake events. The agreement is very good for both fits ID 1 and ID 4. As visible in figure 8.11, the influence of different ADC calibrations is small.

Speed of the particle traversing the array

As the line fit yields a speed v_{LF} of the particle associated with the track, one might put a restriction on this parameter. One might expect that this parameter is in the order of the speed of the particle, i.e. 0.3 m/ns. However, it turns out that the fitted speed is
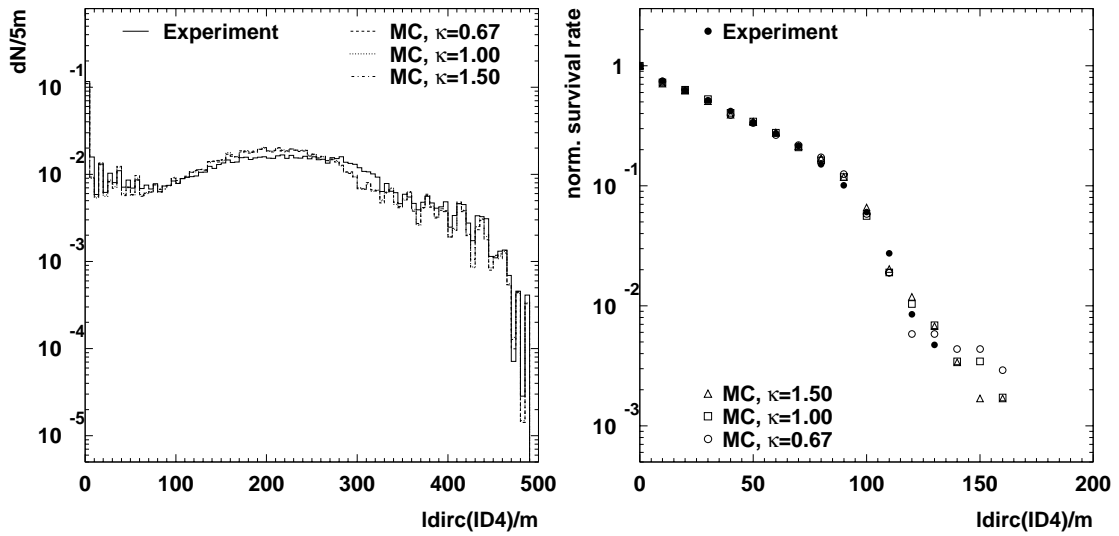
Figure 8.11: Left: distribution of *ldirc* for fit ID 4, right: relative fake rate in dependence of *ldirc* for this fit in experiment and background simulation data.

very sensitive to delayed hits, often resulting in numerical values much lower than the particle speed. Shower-like, more spherical events yield even lower speeds than track-like events. The distribution for the ID 1 fit using all amplitudes unweighted is seen in figure 8.12. Overall, the agreement between Monte Carlo and experiment is good. There is a
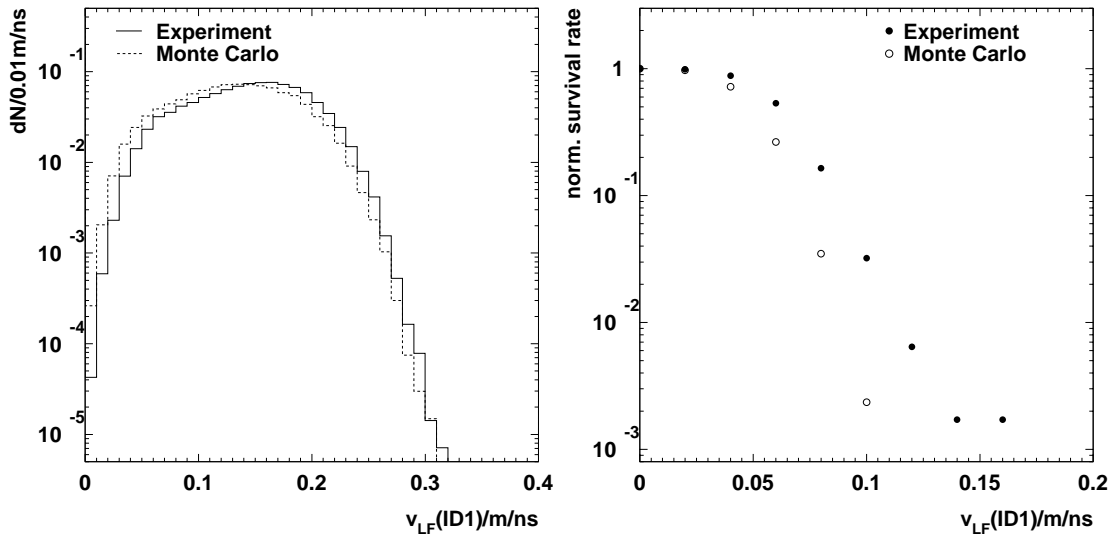
Figure 8.12: Left: distribution of the speed of the line fit for a fit based on all the hits (fit ID 1), right: the normalised fraction of fakes remaining after a cut above some value of v_{LF} in experimental and background simulation data.

small systematic shift towards lower values in Monte Carlo. The most probable speed is around 0.14 m/ns in Monte Carlo and 0.16 m/ns in experiment. No velocities above 0.32 m/ns are observed. The suppression of fakes in experiment is worse by a factor of two above values of $v_{\mathrm{LF}} = 0.05$ m/ns. This will not allow for a strong application of this cut. Although at $v_{\mathrm{LF}} = 0.05$ m/ns, between 50% and 70% of fake events will survive, its application will reject events which are sphere-like and lack a definite direction and will be reconstructed into random directions.

Number of direct hits in the time window -15 ns to 75 ns

Apart from the projected length of direct hits on the track, the number of direct hits *ndirc* itself can be used as a cut parameter, where a direct hit is characterised by a time delay of the photon between -15 ns and 75 ns[1].

When two uncorrelated muons cross the detector in the lower and upper region, this might lead to a track reconstructed as coming from below. If two direct hits are present, this will result in a large value of *ldirc*. In order to reject this class of fake events, one might additionally require more direct hits. The distribution of the number of direct hits is shown in figure 8.13. In 18% of the cases, there is only one direct hit. At values of *ndirc* between 5 and 15, there is an excess in Monte Carlo. For *ndirc* > 20, the excess is a factor of 2-3 in experiment. The description of fake events is good up to values of 5, afterwards the suppression of fakes in experiment is not quite as efficient as in Monte Carlo. Its application will give an additional factor of about five in background suppression.
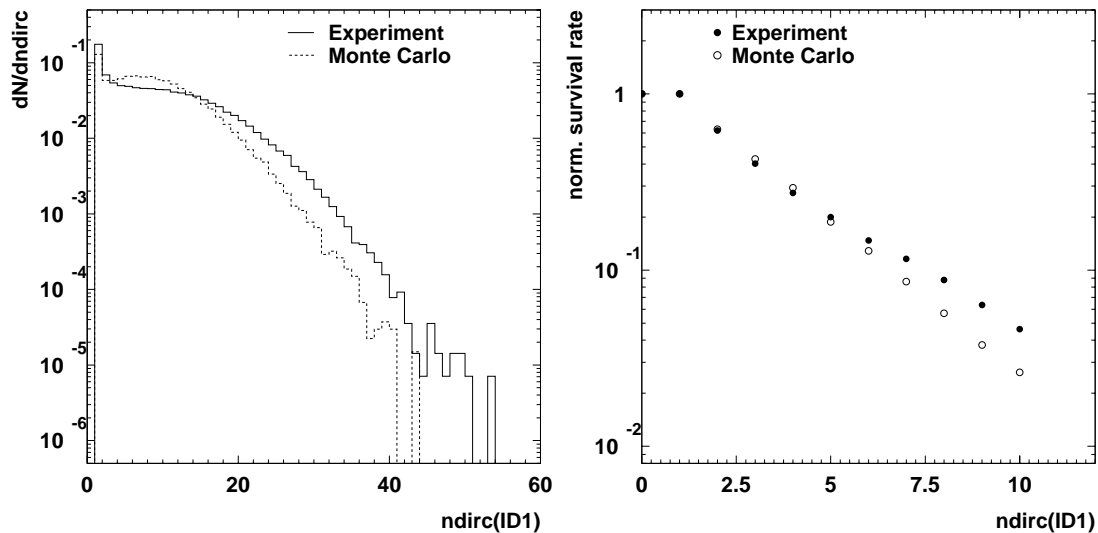
Figure 8.13: Left: distribution of *ndirc* for fit ID 1, right: relative fake rate in dependence of *ndirc* for this fit in experimental and background simulation data.

---

[1]The negative time delay takes into account the PMT's jitter.

Parameter	from	to	step
nch	0	160	10
$v_{\mathrm{LF}}/\mathrm{m/ns}$	0	0.16	0.02
$ldirc/\mathrm{m}$	0	160	10
$ndirc$	0	10	1

Table 8.1: Ranges and step sizes for the parameters used in the neural network.

8.2.2 Fake estimation

From here on, fit ID 4 will be used, because it performs best in terms of zenith mismatch, as found in figure 8.3. Now that the cut parameters have been introduced, their values have to be fixed. The cuts should be set in such a way that no background remains within a chosen amount of data and at the same time the signal efficiency (events surviving the cuts) should be high. Since the simulation, especially in the description of the nch parameter, is not very good, this number has to be estimated in some other way.

This was done by fitting the number of fake events as a function of the four cut values for nch, $ldirc$, v_{LF} and $ndirc$ based on a five day sample of experimental data. The parameters of the sampling grid are given in table 8.1. For each grid point, the number of fake events, defined as events reconstructed with a zenith angle above 90 degrees, was determined. In the considered sample, consisting of $nch > 100$ data from 5 days, 1522 fake events were found.

To perform the fit, a feed-forward neural network (see appendix E) is set up. It consists of 4 input nodes representing the four cut parameters, 8 intermediate nodes and one output node representing the number of fake events. Since sigmoid functions are involved which might saturate if their input is too high, all the cut values were normalised to a range between zero and one:

$$nch \quad \rightarrow \quad nch_{\mathrm{nn}} = nch/160 \qquad (8.3)$$

$$v_{\mathrm{LF}} \quad \rightarrow \quad v_{\mathrm{LF,nn}} = v_{\mathrm{LF}}/0.16\mathrm{m/ns} \qquad (8.4)$$

$$ldirc \quad \rightarrow \quad ldirc_{\mathrm{nn}} = ldirc/160\mathrm{m} \qquad (8.5)$$

$$ndirc \quad \rightarrow \quad ndirc_{\mathrm{nn}} = ndirc/10 \qquad (8.6)$$

Since the background decreases strongly with tightened cuts, the following transformation is applied on the number of fake events:

$$n_{\mathrm{fake}} \rightarrow n_{\mathrm{fake,nn}} = \frac{\log(n_{\mathrm{fake}}/1522)}{-\log(1522)} \qquad (8.7)$$

This transformation [Ashton, 1972] ensures that the desired output stays positive. The net was given the available 5-tuples (4 input, 1 output variable) to learn, requiring that the net answer towards the input variables (nch_{nn}, $v_{\mathrm{LF,nn}}$, $ldirc_{\mathrm{nn}}$, $ndirc_{\mathrm{nn}}$) should match
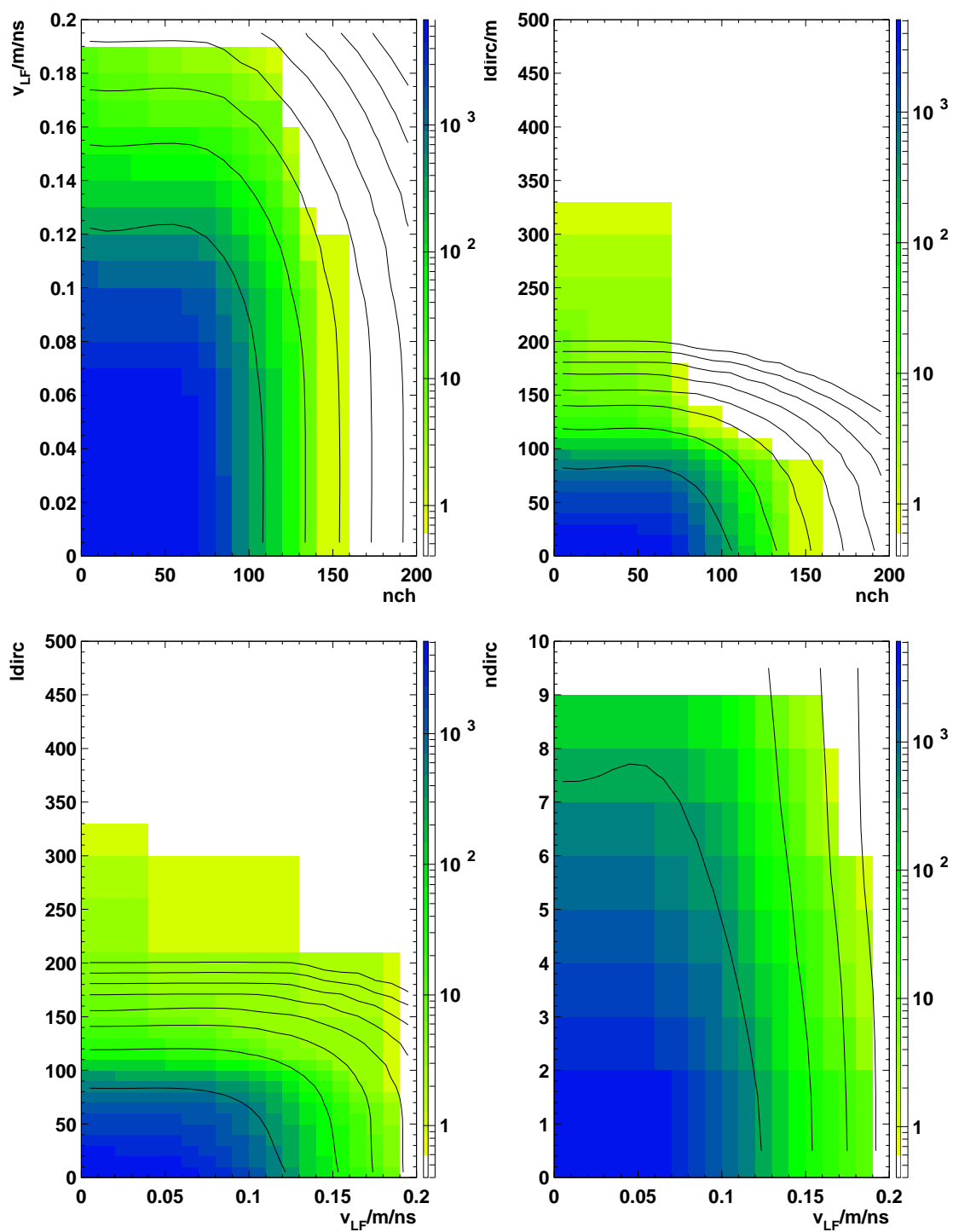
Figure 8.14: Predictions for background appearance gained from training a neural network on 5 days of experimental data, compared to data from 29 days (coloured areas). The network's prediction is represented as contour lines at 1000, 100, 10,…,0.001, 0.0001 predicted events.

the transformed number of fakes $n_{\text{fake,nn}}$. This was done by applying 1000 learning cycles, using the method described by [McLoone et al., 1998].

As a result, a FORTRAN function is produced, which takes the four cut parameters as input and calculates n_{fake}. The result was checked ("cross validated") by scaling the network's answer to 29 days and comparing it to a 29 day sample of experimental data disjunct from the training sample. To demonstrate the agreement, 2 dimensional projections are chosen. The comparison is done in figure 8.14.

In the top left figure, the projection to the nch/v_{LF} plane is shown. The contour lines representing 1000, 100, 10, ..., 0.00001 events give a good description of the data actually found. In the top right plot, showing the projection to the $nch/ldirc$ plane, one observes a discrepancy which, however, is located much below the multiplicity range considered for the monopole analysis ($nch > 100$). This is caused by a background pedestal extending in the $ldirc$ direction which is too small to be visible in the low statistics sample used to train the net but becomes apparent when the sample size is increased. This leads to a prediction which is too optimistic in the sense that the number of predicted events is too low. In the bottom left picture, showing the $v_{\text{LF}}/ldirc$ projection, the distribution is characterised by a constant background with respect to the $ldirc$ distribution.

The prediction still holds if the other parameters outside the projection are applied, as shown in figure 8.15. Additionally to the two main cut parameters, nch and $ldirc$, the two other cuts on $v_{\text{LF}} > 0.05$ m/ns and $ndirc > 4$ were applied. The contour lines
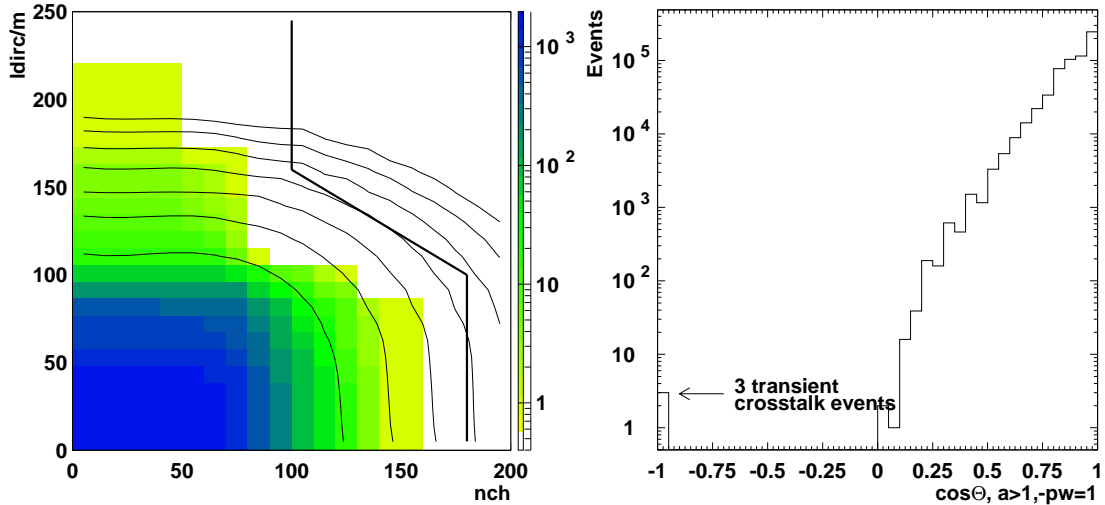
Figure 8.15: Left: distribution of 29 days fake events in the $nch/ldirc$ plane for fit ID 4 (> 1, w) for data with $v_{\text{LF}} > 0.05$ m/ns and $ndirc > 4$. The contour lines represent a predicted background of 100, 10, 1, 0.1, 0.01, 0.001 and 0.0001. The bold line indicates the chosen cut. Right: Cosine zenith distribution of events in experimental data surviving the cuts 8.10, 8.11, 8.8 and 8.9.
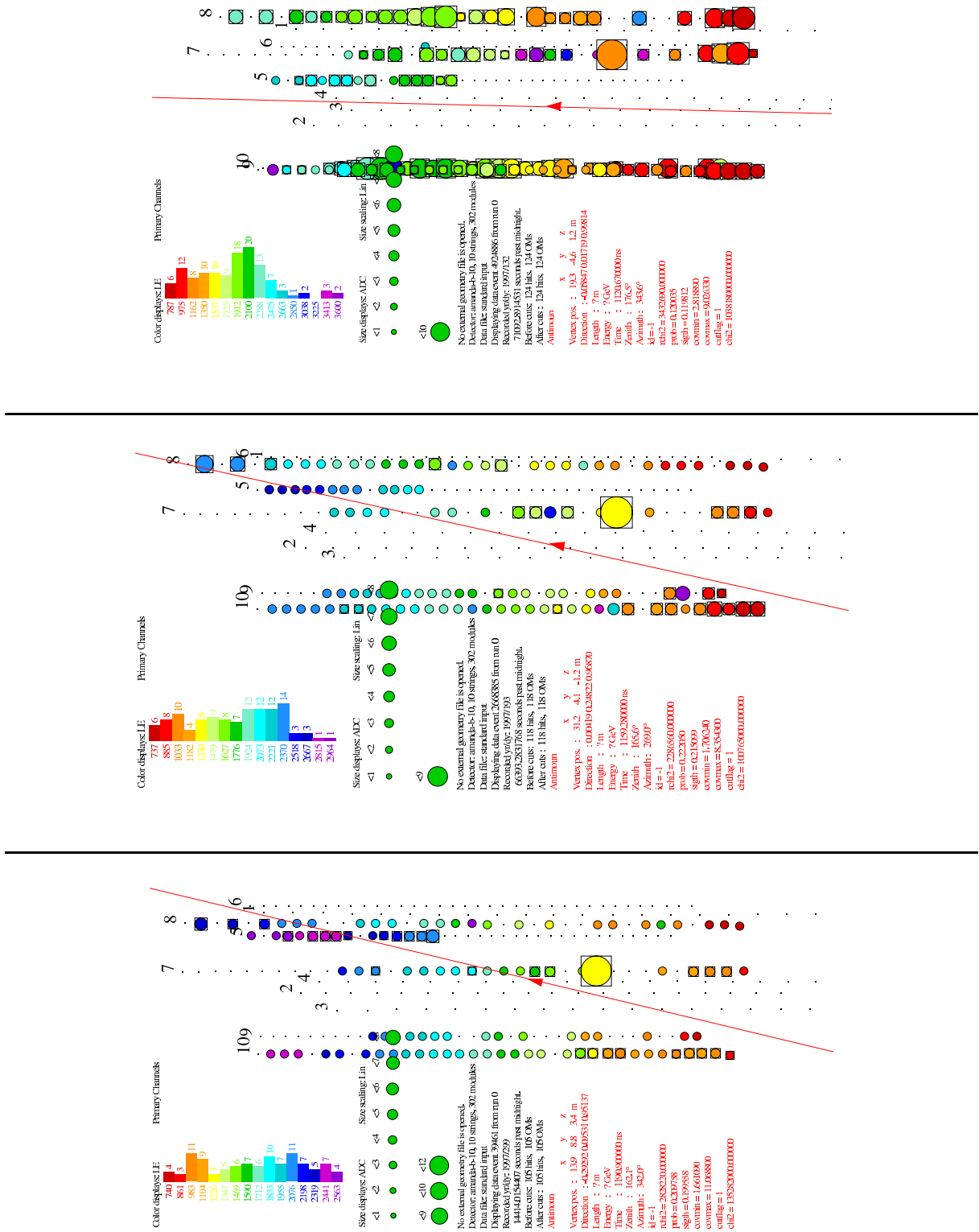
Figure 8.16: The three remaining events. From left to right: Event 4924886, run 687-22, day 132, event 2668385, run 782-12, day 193 and event 39461, run 1086-0, day 299. The $a > 0, -pw = 1$ fit is also given. The light arrival times are colour-coded, i.e. the early times are in red, the late ones are in violet. The size of the OM represents the amplitude.

gained from 5 days are still in agreement with the observation from 29 days. In order to get an expectation of less than 1 event in 200 days, one would need a suppression factor of 29/200=0.15. The contour line representing the cut has been approximated by a set of cuts linear in the four cut parameters:

$$v_{\mathrm{LF}} > 0.05\mathrm{m/ns} \tag{8.8}$$

$$ndirc > 4 \tag{8.9}$$

$$nch > 100 \tag{8.10}$$

$$ldirc > 235\mathrm{m} - 0.75\mathrm{m} \times nch \text{ or } nch > 180 \tag{8.11}$$

which are represented as the bold line in figure 8.15. The result of the measurement is shown in figure 8.15 (right), which gives the $\cos(\Theta)$ spectrum of the events surviving the three cuts above (8.8 and following). Three events are left in the upward direction which have to be considered separately. Upon visual inspection, it turns out that in all three
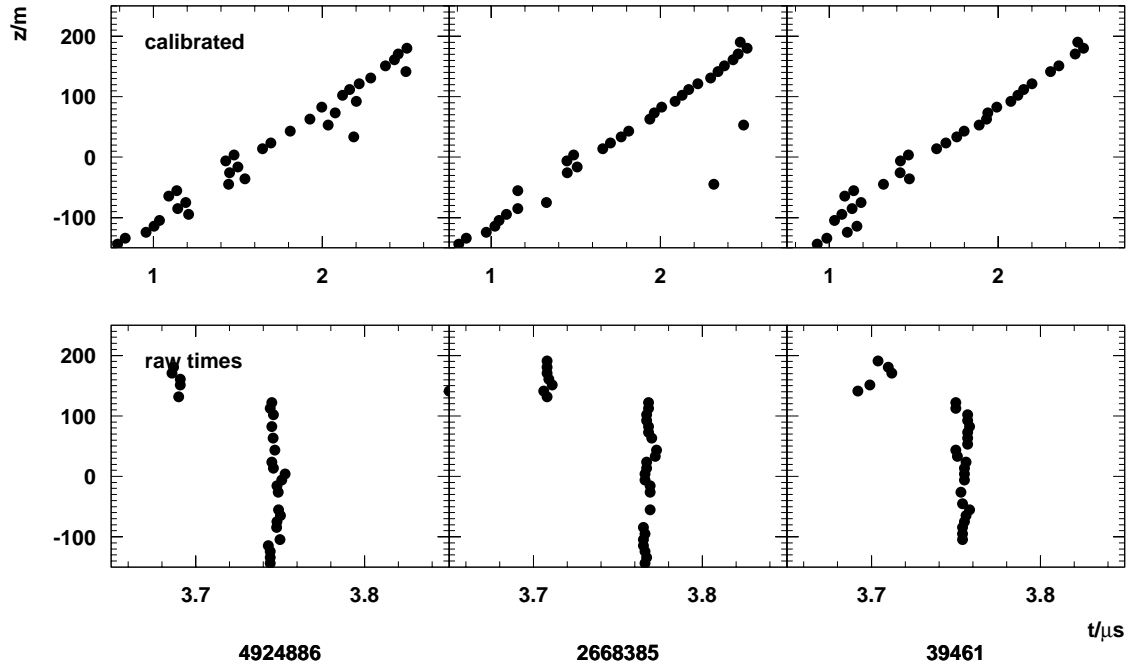
Figure 8.17: For the three events of figure 8.16, the module positions of string 10 are plotted versus their respective hit times. When the times before calibration (lowest plot) are considered, it is found that they are distributed Gaussian with a width σ of less than 5 ns around their mean.

events, only the outer strings 5 to 10 are hit but none of the inner ones are. When looking at the simulated monopole event in figure 6.5, one will find that it is not very likely for a bright object as a monopole to go right through the array and not to have hits on the inner strings 1 to 4.

This absence of hits points to a apparatus-specific effect, which has not been simulated. This effect occurs only rarely as opposed to the permanent crosstalk discussed in connection with figure 8.8. Displays of the three events are shown in figure 8.16. In figure 8.17, the position of each hit module on string 10 is shown in dependency of the hit or leading edge time. The calibrated module depth/time pairs (t, z) can be fitted using a linear model $z(t) = v_z \times t$ which in all three events yields a speed of 0.18 m/ns, which is roughly the signal propagation speed in the cable, the numerical value of which is 0.20 m/ns. This could be explained by assuming a simultaneous recording time in the electronics, which will be translated into a signal propagating with the signal speed in a cable when the time calibration is applied. Considering the raw times by reversing the calibration, the lowest plot of figure 8.16 demonstrates that the signals occur almost simultaneously within 5 ns in two groups at around 3.70 μs and 3.75 μs at the input of the electronics. This points to an effect in the surface electronics which is decoupled from physics processes in the detection medium. Therefore, these three events will not affect the detection efficiency.

No candidates thus remain in the analysis.

8.2.3   Effects of the chosen cuts on the reconstruction

The main observable with which fakes will be rejected is the reconstructed zenith angle. Thus it has to be checked how the cuts on other variables than the zenith angle affect the result of the reconstruction.

The distribution of the cosine of the reconstructed zenith angle is shown in figure 8.18 for the fit ID 4. Monte Carlo and experiment were scaled to unity in the plots. The agreement between Monte Carlo and experiment is good and the variation of the ADC calibration does not affect the result either.

Having shown that the angular distribution between muon Monte Carlo and experiment is in good agreement, one can be confident that the description of the angular properties by the simulation is correct to the desired level. Thus, the angular mismatch distribution in figure 8.19 (left) can be considered meaningful. In comparison with figure 8.3 it is seen that the cuts also improve the angular resolution.

One comes to the same conclusion for the signal. Figure 8.19 (right) illustrates the accuracy of the reconstruction. The weighting leads to an almost complete separation of the hemispheres. The price to be paid for the cuts is a low acceptance of events in the horizontal region. The angular acceptance of the analysis for the ID 4 cut is shown in figure 8.20. Events around the horizon ($\cos(\Theta) = 0$) are suppressed and the acceptance rises towards steeper tracks ($\cos(\Theta) = \pm 1$). The upward going tracks are enhanced because most of the optical modules face downwards.
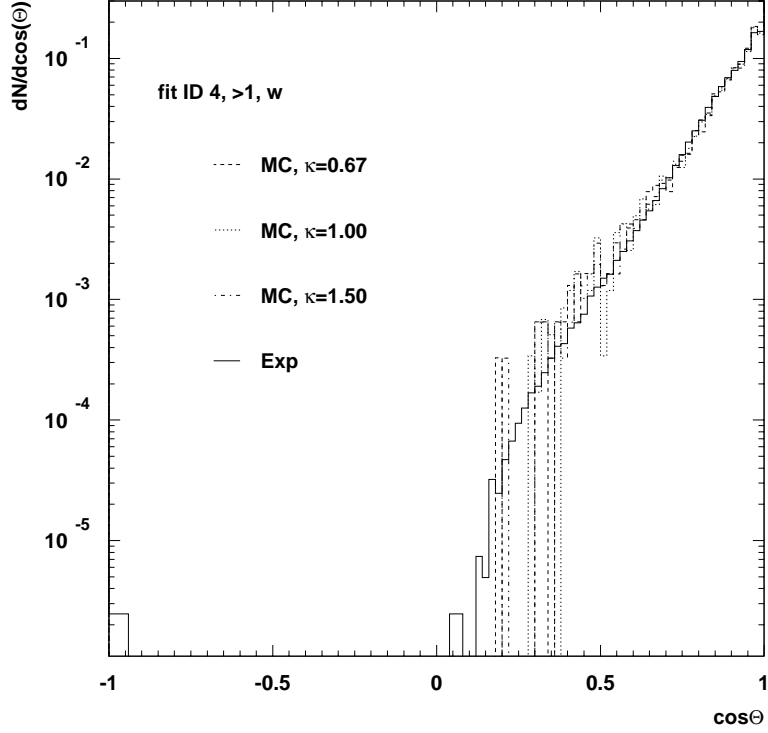
Figure 8.18: Distribution of the cosine of the reconstructed zenith angle in experiment and atmospheric muon Monte Carlo after all cuts. Because the amount of experimental data is many times higher than the Monte Carlo available, all distributions were scaled such that the integral is unity.

8.2.4   Calculating the flux limit

As no events have been observed in the analysis, an upper limit on the flux Φ_{CL} can be stated:

$$\Phi_{\mathrm{CL}} \leq \frac{N_{\mathrm{CL}}}{\mathcal{A} \times T \times \eta}. \tag{8.12}$$

Here, N_{CL} is the upper bound of an interval containing a certain fraction of a probability $P(n_0, \mu + b)$ distributed Poissonian around a mean value of μ to observe n_0 events in presence of a number of background events b:

$$\mathrm{CL} = \int_0^{N_{\mathrm{CL}}} \mathrm{d}\mu P(n_0, \mu + b). \tag{8.13}$$

For $n_0 = b = 0$ as observed, and a confidence level CL of 90%, the commonly used value, one finds $N_{\mathrm{CL}} = 2.33$. $\mathcal{A}$ represents the aperture or acceptance of the detector i.e. the area multiplied by a solid angle the detector can survey. The other numbers needed are the exposure time $T \times \eta$, where T is the actual observation time and η corrects for the dead time of the detector.
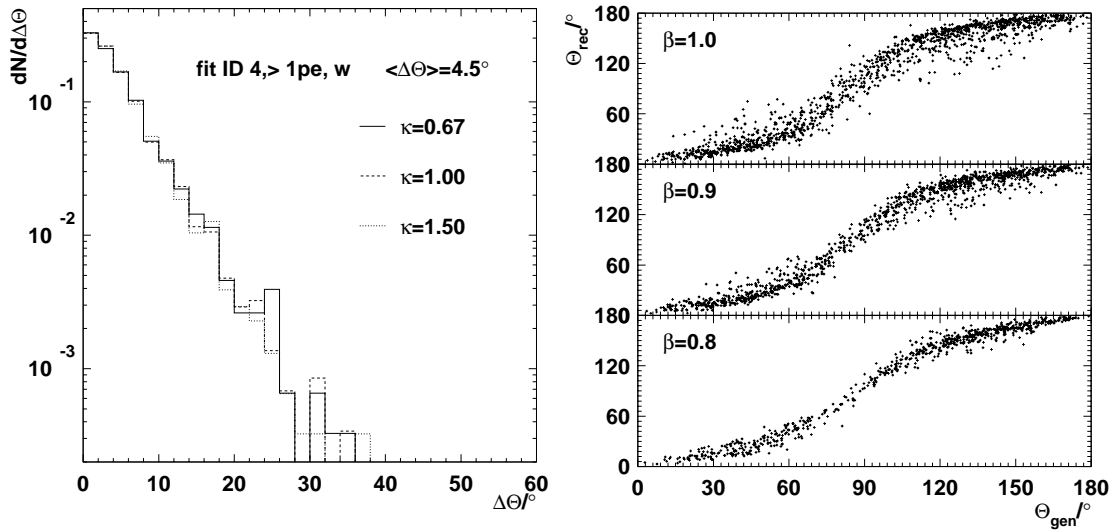
Figure 8.19: Results of fit ID 4. Left: distribution of the zenith mismatch for various fits after cuts for muon simulation. Right: reconstructed vs. generated zenith angle for different fits and speeds in monopole simulation after cuts.
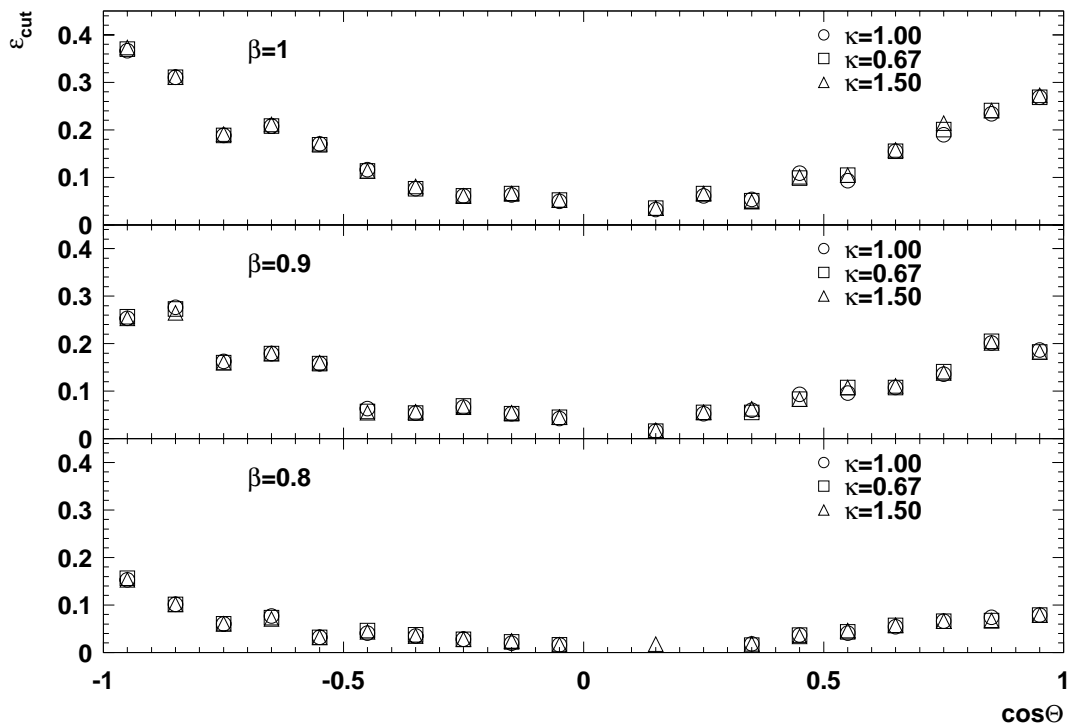
Figure 8.20: Fraction of monopole signal events as a function of cosine of the reconstructed zenith angle after quality cuts but without any explicit angular cut.

β	$\kappa = 1.00$	$\kappa = 0.67$	$\kappa = 1.50$
1.0	3.29	3.28	3.32
0.9	2.39	2.39	2.37
0.8	0.78	0.76	0.76

Table 8.2: Acceptances for the analysis considering the lower hemisphere in units of $10^9 \text{cm}^2 \text{sr}$.

Determining the acceptance

The acceptance takes into account the area and stereo angle which can be surveyed by the detector in dependence of the zenith angle Θ. The contribution $\mathrm{d}\mathcal{A}(\Theta)$ is given by

$$\mathrm{d}\mathcal{A} = \mathrm{d}\Omega \times A_{\text{gen}} \times \epsilon_{\text{trigg}}(\Theta) \times \epsilon_{\text{cut}}(\Theta), \tag{8.14}$$

where $\mathrm{d}\Omega$ is the fraction of the solid angle, A_{gen} the size of the generation plane, with the normal vector inclined at angle Θ, ϵ_{trigg} (cf. figure 6.4) and ϵ_{cut} (cf. figure 8.20) are the trigger and cut efficiencies for a given angle respectively. The two latter are defined as follows:

$$\epsilon_{\text{trigg}} = \frac{\text{Number of events triggered at } \Theta}{\text{Number of events generated at } \Theta} \tag{8.15}$$

$$\epsilon_{\text{cut}} = \frac{\text{Number of events reconstructed up going after cuts}}{\text{Number of events triggered at angle } \Theta} \tag{8.16}$$

Here, Θ is the zenith angle under which the particle to be detected is generated. Thus, $\epsilon_{\text{trigg}} \times \epsilon_{\text{cut}}$ is the fraction of events detected out of all events passing the detector at an angle Θ.

Given azimuthal symmetry of the detector response, the solid angle contribution is given by $\mathrm{d}\Omega = 2\pi \mathrm{d}\cos(\Theta)$.

The total acceptance $\mathcal{A}$ is computed by integrating over desired solid angle Ω, which will be the lower hemisphere:

$$\mathcal{A} = \int_\Omega \mathrm{d}\Omega \times A_{\text{gen}} \times \epsilon_{\text{trigg}}(\Theta) \times \epsilon_{\text{cut}}(\Theta) \tag{8.17}$$

$$= A_{\text{gen}} \times \Omega \times \langle \epsilon_{\text{trigg}}\epsilon_{\text{cut}} \rangle \big|_\Omega , \tag{8.18}$$

where

$$\langle \epsilon_{\text{trigg}}\epsilon_{\text{cut}} \rangle \big|_\Omega = \frac{\int_\Omega \mathrm{d}\Omega \epsilon_{\text{trigg}}(\Theta) \times \epsilon_{\text{cut}}(\Theta)}{\int_\Omega \mathrm{d}\Omega}. \tag{8.19}$$

The time T is the detector run time, i.e. the period over which the electronics is up and recording data. From the number of observed events, i.e. $n_{\text{Event}} = 6057729$ (figure 8.22) and the average rate of $\langle f \rangle = 0.39$ Hz (figure 4.7), one finds $T = n_{\text{Event}}/\langle f \rangle =$

β	$\mathcal{A}/10^9\mathrm{cm}^2\mathrm{sr}$	$\Phi_{90\%}/10^{-16}\mathrm{cm}^{-2}\mathrm{s}^{-1}\mathrm{sr}^{-1}$
1.0	3.28	0.61
0.9	2.37	0.84
0.8	0.76	2.59

Table 8.3: Flux limits obtained from analysing the lower hemisphere.

1.56×10^7s $= 179.8$d. The dead time of the detector is taken into account with the fraction of observable events η (FOE), introduced in chapter 4 with a value of 0.75.

The resulting acceptances are given in table 8.2. The variation of the ADC calibration adjustment κ results in an error of 4%-6%. This error will be taken into account in the upper limit by using the lowest acceptance.

8.2.5 Resulting fluxes

The resulting fluxes are given in the table 8.3 and compared to the results of other experiments in figure 8.21. Compared to the BAIKAL result, the AMANDA limit is lower almost by a factor of 10. The velocity dependence in AMANDA, however, agrees well with the one found by BAIKAL.

The advantages of ionisation experiments which detect monopoles, are their sensitivity to monopoles with speeds down to $\beta = 10^{-4}$ and their rather velocity independent acceptance (due to the DKMPR effect described in section 2.6.2). However, their relatively small detection areas will require long exposure times (typically several years) to reach limits comparable to the ones provided by Cherenkov telescopes in less than one year.

Recent publications ([Kephart and Weiler, 1996, Anchorduqui et al., 2000]) have revived the interest in relativistic monopoles which gives the Cherenkov experiments an advantage by their large observation area. The flux limit measured for $\beta = 1.0$, $\Phi \leq 0.61 \times 10^{-16}\mathrm{cm}^{-2}\mathrm{s}^{-1}\mathrm{sr}^{-1}$, is 1.5 orders of magnitude below the Parker bound of $10^{-15}\mathrm{cm}^{-2}\mathrm{s}^{-1}\mathrm{sr}^{-1}$. A better limit is achieved in Mica searches, resulting in fluxes as low as $\Phi \leq 10^{-17}\mathrm{cm}^{-2}\mathrm{sr}^{-1}\mathrm{s}^{-1}$ at velocities of $\beta = \mathcal{O}(10^{-3})$ [Price, 1984]. However, with AMANDA one would have the chance of seeing a monopole directly.

8.3 Search across the upper hemisphere

The search for monopoles from below restricts their mass to values above 10^{11} GeV. It would be interesting to be able to search for monopoles from above, since already monopoles with a mass of 10^{6-8} GeV would reach the detector, see chapter 2. Now the question is where to apply a cut value for the cut parameter "number of channels" (nch). Assuming that the distribution of nch seen in figure 8.5 (left) is dominated by the background, one would define the signal region as that right to the background. Apparently, one cannot use the prediction from the Monte Carlo. Using this would yield
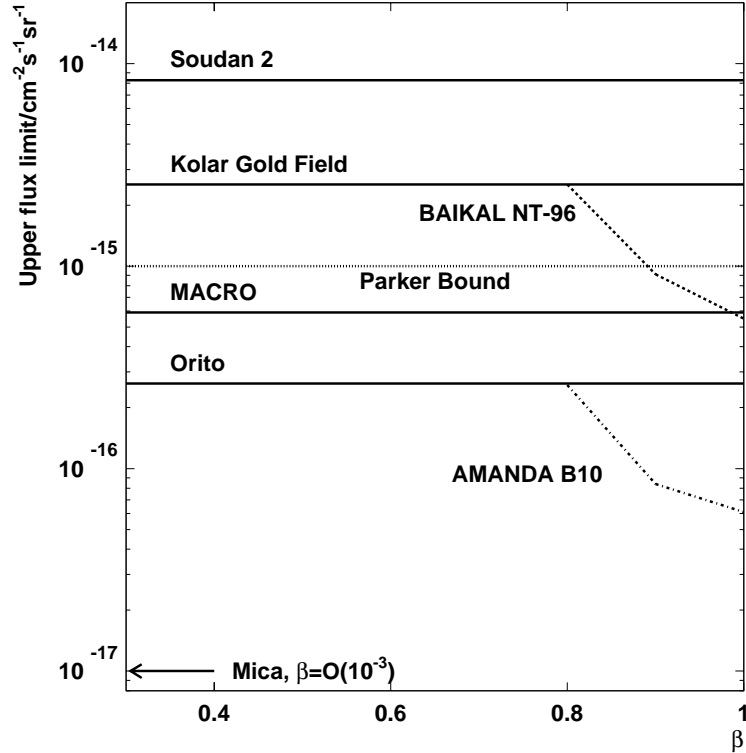
Figure 8.21: Flux limits (90% C.L.) for relativistic monopoles gained from various experiments [Cei et al., 1998]. The BAIKAL result [Balkanov et al., 1999a] is based on $T{\times}\eta{=}72$ days live time.

a cut of $nch > 165$. Then processing the experimental data would yield many monopole candidates. Thus the experimental data itself has to be used to do the prediction.

As in this case the background contamination of the data is not known to a sufficient degree, the procedure allows the determination of an upper flux limit only if a region in parameter space is found which is free of events but has a non-zero acceptance for signal. As only a few days are processed for fixing the cuts, one extrapolates the behaviour to many days of data. This was done like in the four-dimensional analysis of the "lower hemisphere".

In a first step, the function $f_{\mathrm{BG}}(nch > x)$ was evaluated from the experimental data. This monotonously falling function is shown in figure 8.22 (left). At $nch = 200$, only one event is left. Now one would like to know the continuation of this function in order to be able to scale it to higher amounts of data. The integrated distribution of the experimental data can be described by a function linearly dropping in its logarithm, where the slope changes around $nch = 175$. The pairs $(x, f_{\mathrm{BG}}(nch > x))$ are fed into a neural network, requiring that the net gives as an output f_{BG} when the input is x.
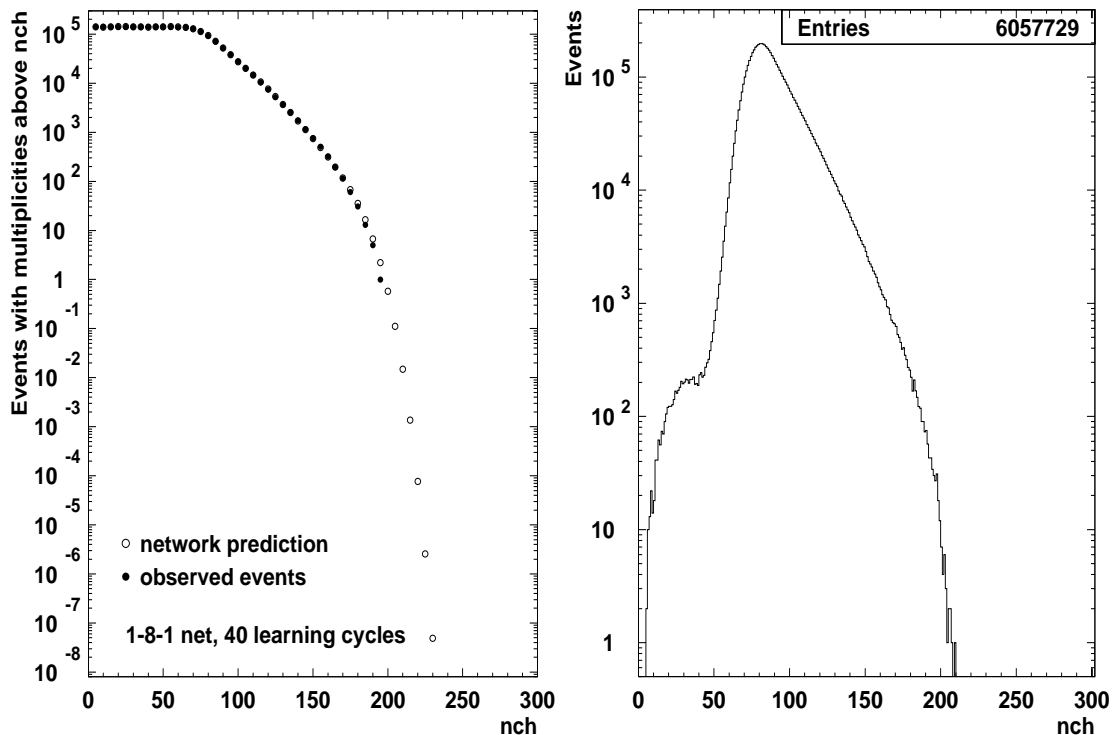
Figure 8.22: Left: number of events above a certain channel multiplicity *nch* in a five days amount of experimental data (140521 events). Right: differential multiplicity distribution in experiment.

Because of the sigmoid functions involved in the net, the input and output values should be between 0 and 1. This was achieved by dividing the input value *nch* arbitrarily by 300. The output value was treated like this:

$$f_{\mathrm{BG}} \to f_{\mathrm{BG,nn}} = \frac{\log(f_{\mathrm{BG}}/n_0)}{-\log n_0} \tag{8.20}$$

where n_0 is of the order of events in the sample. This transformation achieves the desired restriction to the interval $(0,1)$. Additionally, by fitting the logarithm, the re-transformed net output will always be positive [Ashton, 1972]. The learning algorithm used is described in [McLoone et al., 1998]. The number of learning cycles was 40. As a result, the network will provide the function $f_{\mathrm{BG,nn}}(nch/300 > x)$.

To test the stability of the procedure, the network architecture was varied. A network using 8 nodes in the hidden layer ("1-8-1") as well as one using 15 nodes in the hidden layer ("1-15-1") was used. The result for the two models is shown in table 8.4. A graphical representation is shown in figure 8.22. From the table one observes that in the region where events still exist $(nch < 200)$, the 1-15-1 over- and the 1-8-1 underestimates, but both predictions are within the statistical error. Comparing the predicted values, one can

nch	events	1-15-1	1-8-1
160	321	349.5	311.6
170	114	123.7	117.6
180	31	29.24	35.41
190	5	3.872	6.687
200	-	0.2227	0.5757
206	-	0.02640	0.07668
209	-	0.007875	0.02318
210	-	0.005111	0.01499
211	-	0.003359	0.009597
212	-	0.002147	0.006039
213	-	0.001366	0.003725
214	-	0.0008712	0.002262
215	-	0.0005429	0.001354

Table 8.4: Background expectation (for five days) for two network architectures.

estimate the error of the procedure. It is in the order of factor 3-5 in the interesting range of the high multiplicity limit due to the steepness of the decay of background. Requesting the background expectation for 200 days to be ≤ 0.1 events (i.e. getting a probability of $1 - P(0, 0.1) \approx 9.5\%$ for observing one or more background events), and using the more pessimistic 1-8-1 values, one gets 5 days / 200 days $\times$ 0.1 events = 0.0025 events corresponding to nch=214.

Processing 180 days of experimental data results in the distribution shown in figure 8.22 (right). Above a channel number of 214, indeed no events are observed. It turned out that the acceptance for monopole tracks from the upper hemisphere is very low, see table 8.5. This is explained in the following way: when a monopole enters the array from above, the Cherenkov light will reach the photo cathode of the downward looking PMT not directly, but scattered. This introduces an additional delay, leading to a spread of leading edge times, causing times outside the ADC recording window of 4.27 μs. In the subsequent removal of hits without ADC value, all channels outside the ADC gate are lost. In that way, high multiplicity events are reduced to smaller numbers. As a consequence, no signal events above 214 channels are left, instead, the highest channel numbers observed are 210 for $\beta = 1.0$ and 205 for $\beta = 0.9$. Thus, a limit for monopoles with a mass above 10^8 GeV cannot be given.

A possible additional criterion to separate monopoles from high energy muon tracks is the continuity of light emission along the tracks, which is expected for monopoles. It turned out that cuts based on continuous light emission did not result in a better discrimination. For details, see appendix B.

nch	n_{obs}	$n_{\text{1-8-1}}$	$n_{\text{1-15-1}}$	$\mathcal{A}/10^9\mathrm{cm}^2\mathrm{sr}$
200	39	24.85	9.64	0.468
201	27	18.25	6.97	0.420
202	20	13.33	4.94	0.359
203	16	9.58	3.47	0.322
204	10	6.83	2.41	0.205
205	7	4.77	1.64	0.170
206	6	3.30	1.14	0.135
207	4	2.25	0.76	0.119
208	2	1.50	0.51	0.080
209	1	1.00	0.33	0.034
210	1	0.65	0.22	0.034
>211	-	-	-	0.000

Table 8.5: Observed events, expected events and simulated signal acceptances for the analysis searching monopoles from above in case of $\beta = 1.0$ monopoles in units of $10^9\mathrm{cm}^2\mathrm{sr}$ for as a function of nch. Above 211 channels, the detector will not see any monopoles with zenith angles below $90°$.

Chapter 9

Conclusion

In this thesis, results on the search for relativistic magnetic monopoles with the AMANDA detector have been presented. During the last years, relativistic magnetic monopoles have gained strong interest. Firstly, new models of the magnetic fields in the universe would allow even heavy monopoles (10^{16} GeV) to be accelerated to relativistic speeds, secondly, there are hypotheses that magnetic monopoles are the origin of the highest energy cosmic rays.

For the purpose of monopole search with the AMANDA detector, the programs which simulate the light propagation and the detector response have been extended to cover a larger volume than in the standard versions and take into account particles with velocities $\beta = \frac{v}{c}$ in the range $0.75 < \beta < 1.00$, respectively.

In the subsequent reconstruction tracks were fitted to the hit timing patterns generated by the simulation. Several reconstructions were performed, making different use of amplitude information of the hits. The fit result did not depend strongly on the amplitude calibration and the reconstruction error was found to be about $7°$ on average.

For the actual analysis, neural nets were applied to predict the number of background events which remain. This was necessary because the Monte Carlo used was found not to be accurate enough in its description of high multiplicity events selected for the separation of signal from background. As a possible cause for this feature, the absence of elements heavier than hydrogen in the primary particle simulation as well as cross talk in cables and electronics have been discussed.

Within the monopole search, the sky has been divided into an upper and lower hemisphere. When searching across the lower hemisphere, the Earth is used as a shield against the atmospheric muon background. The price to be paid is a higher limit on the monopole mass: only monopoles with a mass above 10^{11} GeV can cross the full Earth diameter. This mass limit can be lowered to 10^6 GeV by looking at the upper hemisphere. However, since the background of high multiplicity events from above is much higher than from below, and since the sensitivity of the detector to downward moving monopoles is smaller than for upward moving ones, no competitive limit could be derived for lighter monopoles.

The flux limit achieved for the "heavy" monopoles ($\Phi \leq 0.61 \times 10^{-16} \mathrm{cm}^{-2}\mathrm{s}^{-1}\mathrm{sr}^{-1}$ at

$\beta = 1.0$) is lower by a factor of 16 than the limit imposed on the flux by the survival of the galactic field ("Parker limit"). It is also better by a factor of 3-4 at high speeds ($\beta > 0.9$) compared to other experiments.

Appendix A

Optical properties of refrozen ice

This appendix presents results not directly related to the monopole analysis. It concerns the properties of the refrozen ice in the drilling holes. Results obtained by the author and other collaborators enter the simulation of the detector response and therefore, indirectly, form a technical input information also used in the analysis.

Although the bulk ice at AMANDA-B depths has been shown to be relatively free of scatterers, the process of drilling with hot water might increase the scattering locally in the holes. During the Austral summer 1997/98, a camera was lowered into one of the holes drilled for the extension of AMANDA-B to 13 strings. About 36 hours of re-freezing were recorded on video tape. Indeed, upon analysing the visual data it was found that bubbles formed during the process of re-freezing [Thollander, 1998]. These bubbles are thought to appear only in the hole and not in the surrounding medium. Here it will be discussed how parameters of the bubbles can be assessed.

The PTD package was extended to simulate bubbles with scattering lengths of 10 cm, 30 cm, 50 cm and 100 cm in a infinitely long cylinder around the optical module [Karle, 1998a]. These options were used to simulate events caused by atmospheric muons in the AMANDA-B4 detector [Niessen, 1998].

A.1   Trigger efficiencies

The trigger efficiency is affected by the bubble scattering length. Table A.1 shows the corresponding values. The value ∞ corresponds to the case where no bubbles are present in the hole. The rate is obtained from the trigger efficiency by

$$\text{Rate} \approx \text{Efficiency} \times 4.07 \cdot 10^3 \text{Hz}$$

[Hundertmark, 1999]. The efficiency rises towards shorter values of λ_{bub}. This can be explained in the following manner: As the density of bubbles increases, light passing through the hole is also scattered into the opposite direction, which is not the case in scatter free ice. Thus light passing away from the photo cathode has the chance to be seen by the optical module.

λ_{bub}	10 cm	30 cm	50 cm	100 cm	∞	Experiment
ϵ_{trigg}	$8.3 \cdot 10^{-3}$	$5.8 \cdot 10^{-3}$	$5.3 \cdot 10^{-3}$	–	$4.4 \cdot 10^{-3}$	–
Rate	34 Hz	24 Hz	22 Hz	–	18 Hz	23 Hz

Table A.1: Trigger efficiencies and calculated rates for the different hole ice scenarios in comparison to the observed experimental values. The values for $\lambda_{\text{bub}} = 100$ cm was lost.

λ_{bub}	MEAN	CONST	SLOPE
10 cm	12.66	10.34 ± 0.13	-0.221 ± 0.008
30 cm	12.22	10.18 ± 0.04	-0.240 ± 0.003
50 cm	12.08	10.13 ± 0.04	-0.245 ± 0.002
100 cm	12.02	10.06 ± 0.03	-0.248 ± 0.003
Exp.	11.88	10.58 ± 0.03	-0.210 ± 0.002

Table A.2: Mean values and fit results for the observed channel multiplicities in dependence of various values for λ_{bub}.

A.2 Event multiplicity

The number of hit channels is shown in figure A.1. Since the rate was seen to rise according to the density of bubbles, one might expect that the average multiplicity also rises, since more optical modules get a chance of seeing light which they might not have seen without bubbles. Indeed, the mean number of hit modules increases, but only on a 5% level from 12 ($\lambda_{\text{bub}} = 100$ cm) to 12.7 ($\lambda_{\text{bub}} = 10$ cm). The slope of an exponential fit ($f(m) = \exp\{\text{CONST} + \text{SLOPE} \cdot m\}$) also steepens towards higher values of λ_{bub}, but the effect is very minute. The mean multiplicities and results of the fit are given in table A.2.

A.3 Time differences

A simple variable to be considered is the time difference of leading edges in two neighbouring modules on a string. This method has the advantage that no reconstruction is required; any biasing effect of this would be eliminated. For the four hole ice models and experiment, the time difference of the leading edges of neighbouring modules was histogrammed. Since the RMS of the distribution depends on the range of the histogram (see table A.3) a Breit-Wigner function

$$BW(x) = g\frac{\Gamma^2/4}{(x-\mu)^2 + \Gamma^2/4}$$

Multiplicities
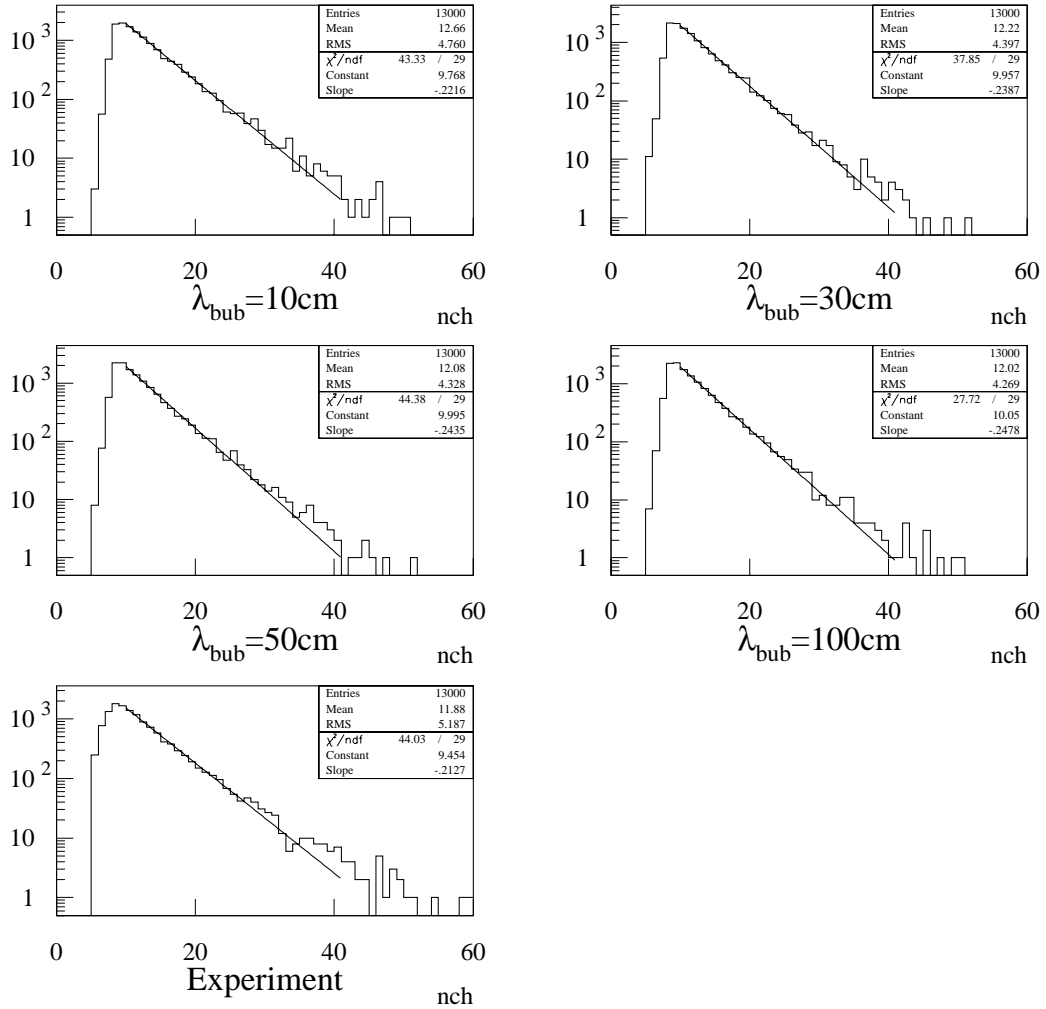
Figure A.1: Channel multiplicities for the simulated values of λ_{bub} and experiment.

bins	from	to	Mean	RMS	μ	Γ
100	-1000	1000	28	274	39	191 ± 5.41
150	-1500	1500	28	323	39	190
200	-2000	2000	25	360	39	191
400	-4000	4000	26	402	39	192

Table A.3: Influence of histogram extension to the RMS values and Breit-Wigner fit parameters μ and Γ, OM pair 65/66.

with normalisation g, mean μ and width Γ was fitted to the distribution. This yields a more stable result compared to the RMS. The width Γ of this distribution is recorded for each pair and plotted versus the depth of the upper module of the pair. The distribution is shown in figure A.2 In this plot, arrows mark the pairs of OM's whose photo cathodes
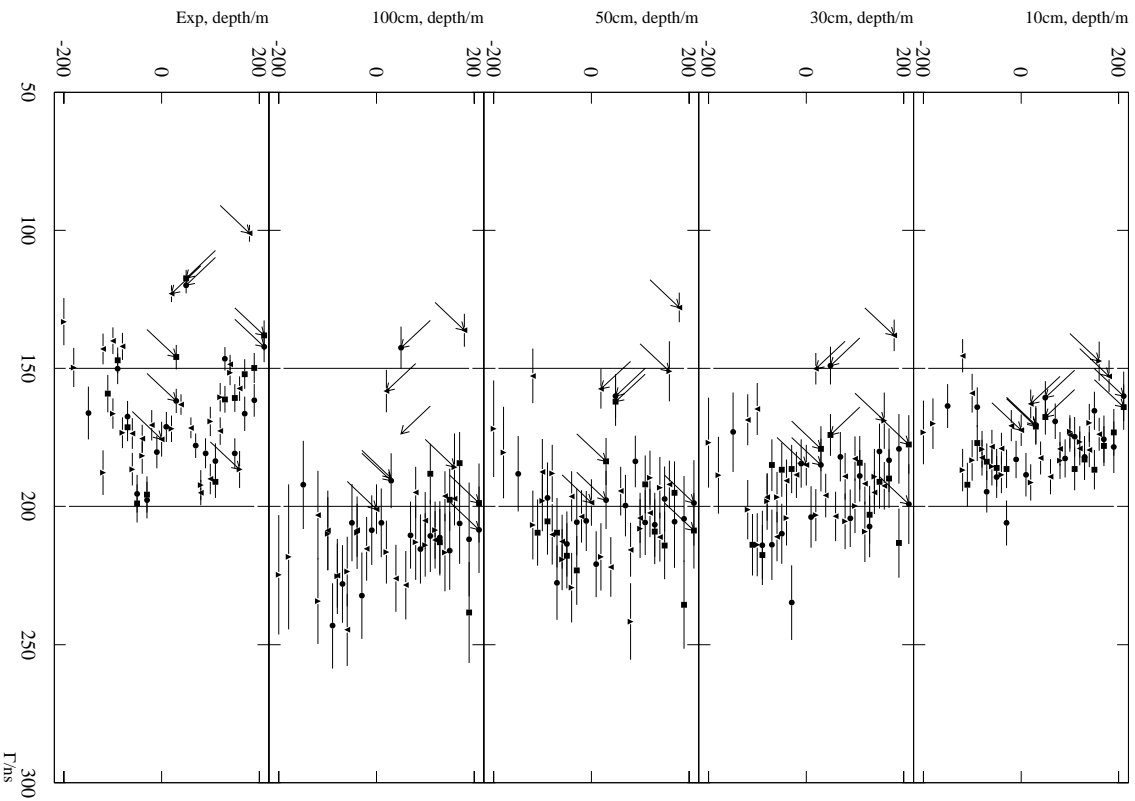
Figure A.2: Breit-Wigner widths Γ for the time differences of all four strings in AMANDA-B4. $\nearrow$ indicates an "up/down" combination, $\searrow$ a "down/up" combination for four values of λ_{bub} and experiment.

face each other ($\searrow$) or look away from each other ($\nearrow$). Generally, the width of the fit increases as λ_{bub} increases. In the 10 cm scenario, the values are spread around 175 ns. Here, the bubbles level out the effect which is caused by the orientation towards each

Combination	$\Gamma_{\mathrm{EXP}}/\mathrm{ns}$	Γ_0/ns	α/ns	$\lambda_{\mathrm{bub}}/\mathrm{cm}$
DD	187.6 ± 0.8	212.1 ± 1.3	17.4 ± 1.5	62.9 ± 15.5
UD	150.1 ± 1.9	181.0 ± 2.9	8.7 ± 3.2	63.2 ± 41.8

Table A.4: Fit results from figure A.3.

other. When comparing this to the experimental data, this nivelling effect is not seen. This indicates that the 10 cm scenario does not hold, it is too extreme. However, as soon as λ_{bub} increases, the module pairs oriented away/towards each other start sticking out from the bulk of only down looking modules. However, at the same time the average value of the Breit-Wigner Γ starts moving above the values observed in experiment. In the simulation, strong fluctuations of Γ are observed, increasing with the value of λ_{bub}. In order to reduce their influence, all OM pairs of the same relative orientation are comprised into a single histogram, yielding one histogram for the up-down combinations, another for the down-up combinations and a third one for the down-down combinations. The result is presented in figure A.3. It shows the dependence of Breit-Wigner fit result Γ in dependence of λ_{bub}. It is seen that there exists a relation

$$\Gamma(\lambda_{\mathrm{bub}}) = \Gamma_0 + \alpha \cdot \ln \left\{ \frac{\lambda_{\mathrm{bub}}}{30\mathrm{cm}} \right\}.$$

As said before, a simple extrapolation of the figures for the down/down combinations would lead to a value of λ_{bub} in the range of 10 cm. However, if one assumes that there is a systematic shift for some reason between Monte Carlo and experiment, which causes the discrepancy between experiment and Monte Carlo in case of the up/down and down/up combination, all the Monte Carlo values had to be lowered by about 37 ns, suggested by the discrepancy of the down/up combinations in Monte Carlo and experiment. The corresponding values of λ_{bub} are given in table A.4. Interestingly, both the down/down and the up/down pairs yield the same value of λ_{bub} within the error. These results were also confirmed by independent measurements ([Woschnagg, , Karle, 1998a, Young, 1998]). In order to check whether the systematic shift is caused by bulk ice, different simulations were run at $\lambda_{\mathrm{bub}} = 50$ cm. The result is that the bulk ice can indeed shift the value of Γ. However, the parameter of bulk ice which is suggested from this, $\lambda_{\mathrm{eff}} = 40m$ is in disagreement with the canonical value of $\lambda_{\mathrm{eff}} = 27$ m.

A.4 Bulk ice effects

As seen in figure A.2, there is a certain variation of the width Γ over the height of the B4 detector. For experimental data, the plot is done once again in figure A.4. The parameter $b_e = 1/\lambda_{\mathrm{eff}}$ was determined by laser measurements [Woschnagg, 1999]. Over the AMANDA-B4 depth between 200 m above and 200 m below the detector centre,

Growth of Spread (BW) int Δt
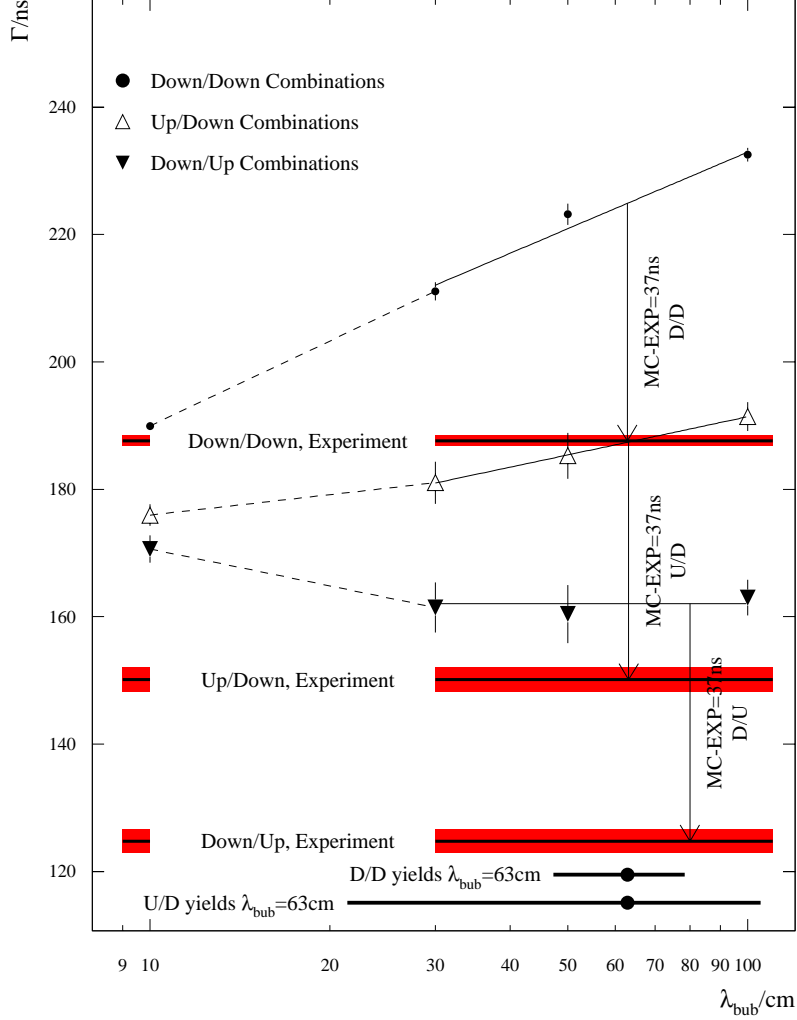
Figure A.3: The width of the time difference distributions between adjacent modules as a function of λ_{bub}. The experimental values are shown as thick solid lines. The errors in Γ given by the fitting program MINUIT are indicated by the width of the shaded bars.

Combination	Γ_{EXP}/ns	Γ_{27m}/ns	Γ_{40m}/ns	Γ_{60m}/ns
DD	187.6 ± 0.8	212.1 ± 1.3	177.4 ± 1.0	144.7 ± 0.7
UD	150.1 ± 1.9	181.0 ± 2.9	151.2 ± 1.9	122.6 ± 1.4
DU	124.8 ± 1.8	160.0 ± 4.5	121.6 ± 2.3	101.3 ± 1.6

Table A.5: Result of the Breit-Wigner fit for $\lambda_{bub} = 50$cm for various values of λ_{eff} indicated by the subscript.
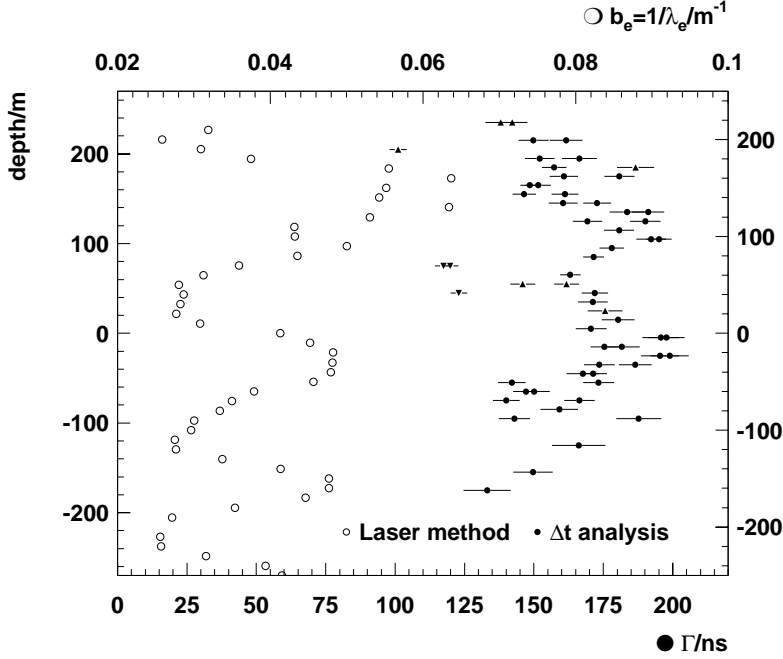
Figure A.4: Breit-Wigner widths ($\bullet$) and inverse of scattering length $b_e = 1/\lambda_e$ ($\circ$).

variations in the 25% regime are observed. There are distinct maxima and minima. The same structure can also be found in the Breit-Wigner widths Γ determined by time difference measurements. This makes it likely that the time differences are also sensitive to bulk ice.

A.5 Effect of bubbles on the channel frequencies

Another observable to look at is the hit frequency of each module. This is shown in figure A.5 for the various bubble parameters and the experiment. String 4 (modules 61 to 80) contains most entries, because it is in the centre of the detector and hit in almost all triggers. Comparing the simulation results to the experiment, it is seen that in simulation, the shape of the distribution within a string is much smoother.

A prominent feature in simulation is the "spiking" of the up-looking modules 10, 30, 70. It increases as the value of λ_{bub} increases. At 10 cm, there is even a dip instead of a spike.
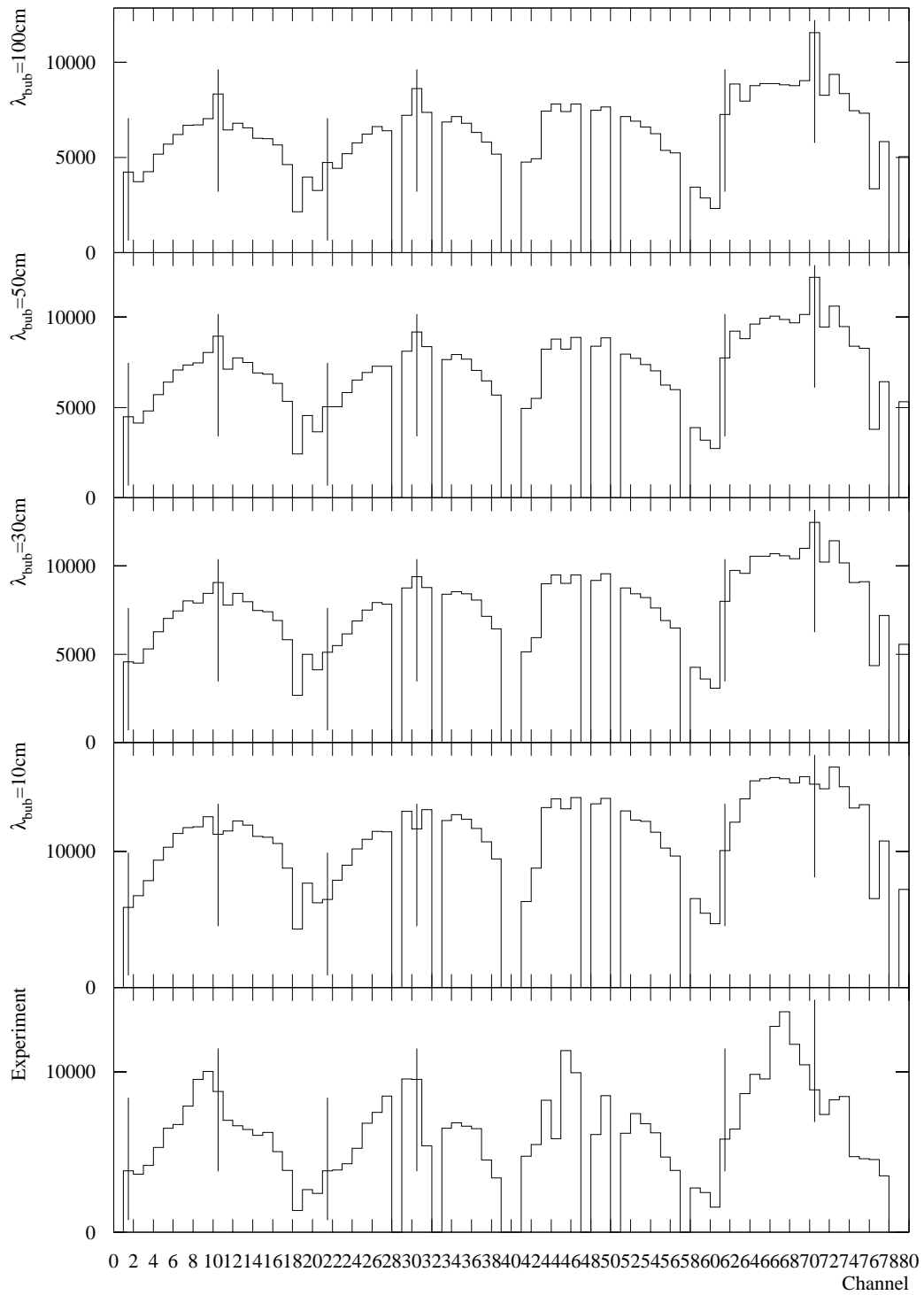
Figure A.5: Hit frequency of channels for the various values of λ_{bub}.

Appendix B

Smoothness of light output along the track

When a muon traverses the Cherenkov medium, it is subject to stochastic processes such as bremsstrahlung and pair production. The secondary particles generated in such reactions also produce Cherenkov light. At a muon energy of 14 PeV, the energy loss becomes comparable to the continuous energy loss of a monopole. However, the stochastic light output from a monopole is smaller by approximately a factor of 100. This motivates the use of an observable called smoothness which would help to discriminate monopoles from other down going signals. The basic idea is sketched in figure B.1. As the particle passes
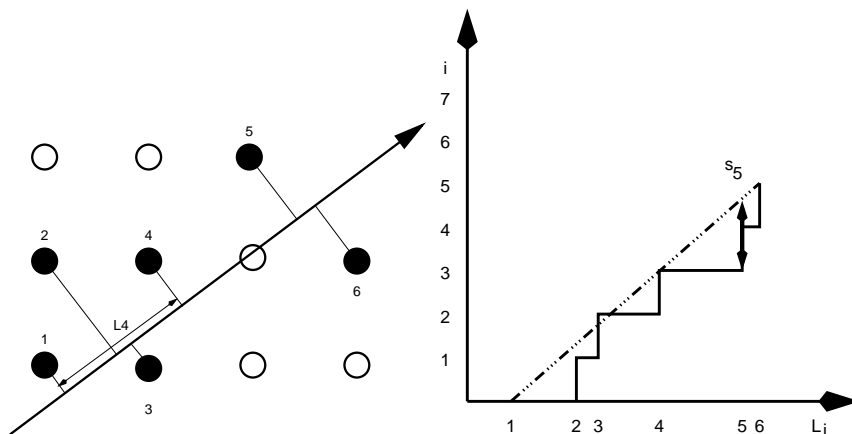
Figure B.1: Left: a particle traversing the array and hitting modules. Right: comparing the light output to a template.

through the detector, the emitted light hits a subset of the modules in the vicinity of the track. If a stochastic process takes place, more modules per unit length are hit in the vicinity of the interaction point. This can be quantised by comparing the number of hit modules to an idealised template which assumes a constant number of hits per unit
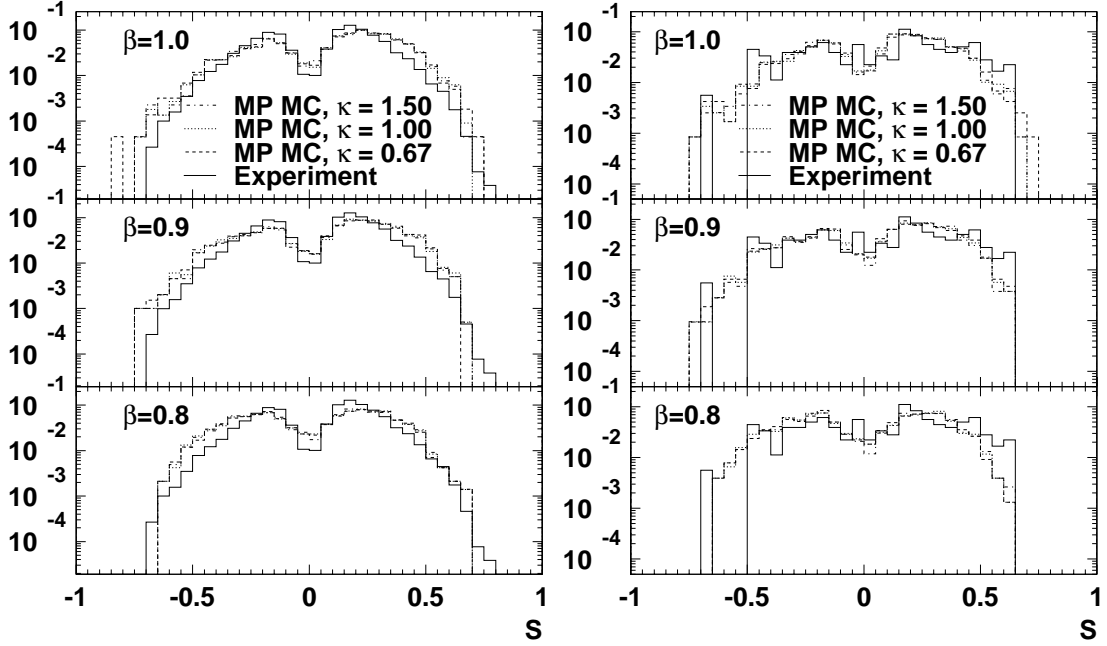
Figure B.2: Distribution of the smoothness observable S in experiment and signal Monte Carlo (MP MC) for three different amplitude calibrations and three different speeds of the monopoles. The curves are normalised to unit area. Left: all events, right: fake events (reconstructed above 90°).

track length. In the right sketch, the template is represented by the dash-dotted line, whereas the actual number of hit modules i after track length L_i is shown by the step like solid line. The smoothness is defined as the maximum distance between the template and the measurement (s_5 in this case). Thus, a lower numerical value indicates a smoother distribution of light output [Gaug et al., 2000].

This concept did work well in the low multiplicity regime of neutrino analysis with average multiplicities around 40. It turned out that no additional selection power is achieved in order to distinguish between monopoles and high multiplicity muon events. This is primarily due to the phenomenon that at the high OM multiplicities dealt with, i.e. above 100 right of which most of the monopole signal is located (cf. figure 8.5), an event is not likely to have several strongly localised clusters of hit modules. Figure B.2 shows the smoothness distribution with respect to fit ID 4. Apparently, the distribution is not well separated for the two kinds of data. One might hope to get a better discrimination for the fake events. The corresponding plot is shown in figure B.2 (right). Here, all experimental events reconstructed as up going are taken into account. From this it is not possible to discriminate mis-reconstructed events from experiment against well reconstructed signal.

Appendix C

Simulations with a cube shaped detector

In order to evaluate the possibilities of the next generation under ice observatory, IceCube, an array of $9^3 = 729$ modules with 10 m and 20 m spacing has been simulated. Figure C.1 shows the acceptance and reconstruction behaviour of this array. The acceptance is very
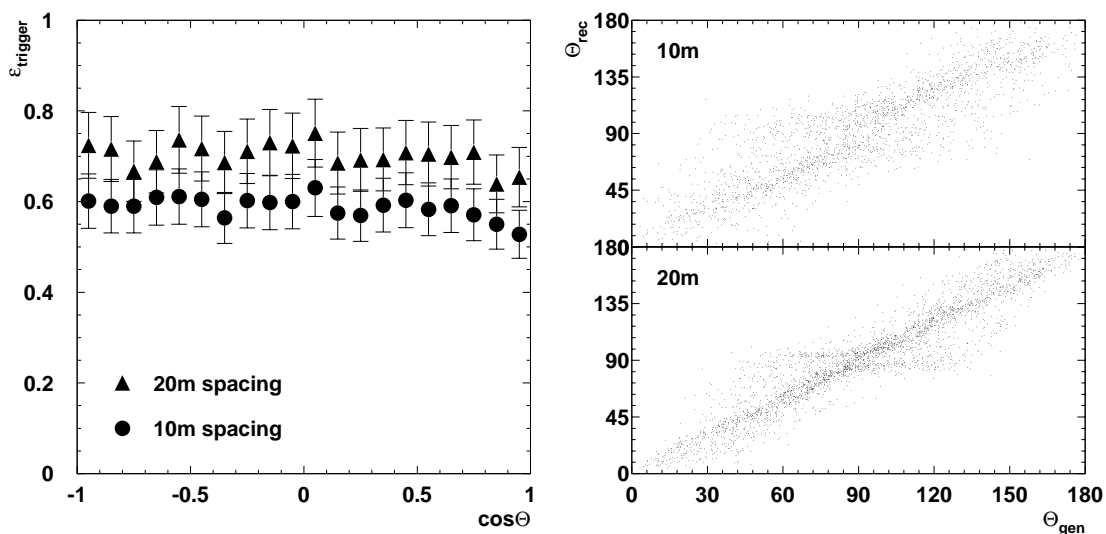
Figure C.1: Left: trigger efficiency for a cubic array with 10 m and 20 m grid. Right: reconstruction accuracy.

even compared with the acceptance of AMANDA, and already without cuts, a weighted line fit gives high accuracy and the distortion towards very small or large zenith angles observed with AMANDA-B10 is absent.

Appendix D

Considerations of detector performance

Here, an analytical method to calculate the fraction of observable events (FOE), η, will be given. Although the approach is different from the one given in [Teich and Cantor, 1975], the result here agrees with it up to the second order of the series expansion. If one assumes that the occurrence of events is Poissonian, η can be calculated in the following way. Consider an event triggering the detector. The detector enters the dead time and is blind for the time τ. If no event follows within this time interval, the efficiency is 100%, see figure D.1. Since the arrival of particles is Poissonian, the probability for this is given
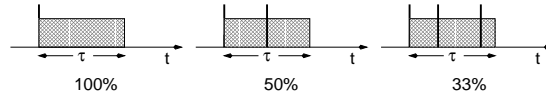
Figure D.1: Distribution of events and subsequent dead time in case of a fraction of detectable events of 100, 50 and 33%.

by

$$P(0, \mu) = \exp\{-\mu\} \tag{D.1}$$

where $\mu = f \times \tau$ is the average number of events within the dead time τ when the rate is f.

As soon as there is one event following within the dead time, the FOE will drop to 50%, because half of the events will be in the dead time and not recorded. The probability for this is given by

$$P(1, \mu) = \frac{\mu^1}{1!} \exp\{-\mu\} \tag{D.2}$$

If there are two events within the dead time, the efficiency drops to 33% and so on. The

FOE can thus be calculated to be

$$
\begin{aligned}
\eta &= P(0,\mu) \times \frac{1}{1} + P(1,\mu) \times \frac{1}{2} + P(2,\mu) \times \frac{1}{3} + \ldots, \sum_{k=0}^{\infty} P(k,\mu) = 1 \qquad \text{(D.3)} \\
&= \sum_{k=0}^{\infty} \frac{1}{k+1} \times \frac{\mu^k}{k!} \exp\{-\mu\} \qquad \text{(D.4)} \\
&= \frac{1}{\mu} \sum_{k=0}^{\infty} \frac{\mu^{k+1}}{(k+1)!} \exp\{-\mu\} \qquad \text{(D.5)} \\
&= \frac{1}{\mu} \times (1 - \exp\{-\mu\}) \qquad \text{(D.6)}
\end{aligned}
$$

This result is in agreement with a more elaborate calculation given by [Teich and Cantor, 1975, DeLotto et al., 1964]. As the dead time τ becomes large, the efficiency should go down, and as the dead time approaches 0, the efficiency should become 1. This behaviour is indeed reproduced by the calculated function. As an example the function is shown in figure D.2
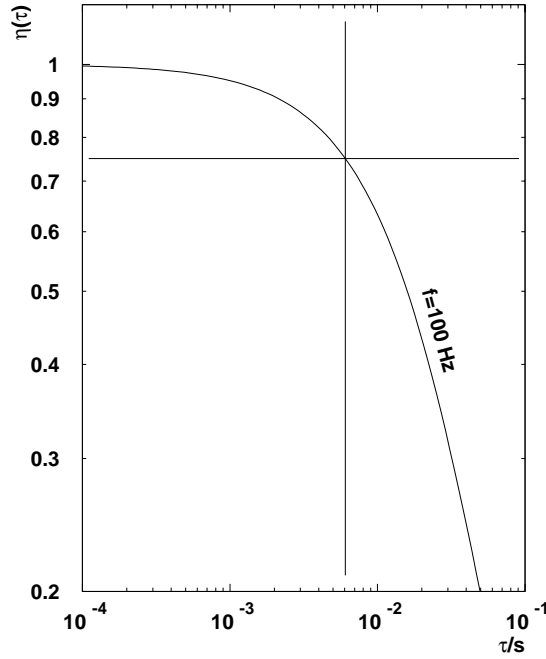
Figure D.2: Left: The fraction of observable events η as a function of τ for particle rates of $f = 100$ Hz (AMANDA B10 muon rate).

Appendix E

Neural Networks

E.1   Introduction

Whereas computers are unbeaten when it comes to highly repetitive tasks such as number crunching, the human brain is unsurpassed in pattern recognition. Here, instead of storing information at known locations in a memory, knowledge is distributed over $\sim 10^{11}$ nerve cells which are connected to each other; signals are processed by passing and receiving signals from neighbouring cells. The storage capacity of the human brain can be estimated to about 10^8 Mbytes [Amendolia, 1993].

E.2   Neurons

At a very low level, this architecture is emulated by means of artificial neural networks (ANN). These consist of an ensemble of units called neurons connected to each other (figure E.1). This basic processing unit accepts several inputs and produces an output, usually in the following way: each input s_j is weighted by a weight w_{ij} and the sum $P_i = \sum_j w_{ij} s_j$ is computed. This sum is fed into an activation function f, which then provides the answer of the neuron. This behaviour is taken from the behaviour of the synapses in the brain in which a certain level of stimulation must be reached before the connected next neuron is activated. Several activation functions are known, such as the step function and the sigmoid $f(P_i) = (1 + \exp\{-P_i\})^{-1}$ (figure E.1, right). In order to make the net recognise some pattern, the weights w_{ij} have to be set in a suitable way; this is the learning process of the net.

E.3   Architecture

Networks are classified by their architecture and their way of learning. Concerning architecture, one distinguishes between feed forward networks (FF-ANN) and recurrent networks (R-ANN) (figure E.2). In a feed forward network, the neurons are organised in
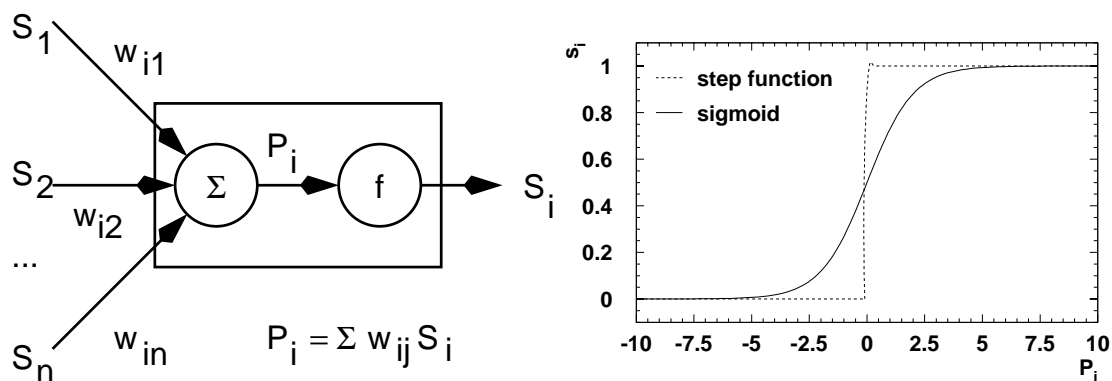
Figure E.1: Left: A neuron. It computes the weighted sum P_i of the input stimuli S_j. The output S_i is generated by applying a threshold function f to P_i. Right: Two activation functions.

layers, the output from a layer is only passed on to the next layer and the neurons in each layer are not connected among themselves. The first layer is the net's input for the patterns it has to recognise, the final layer provides the net's answer. Between the first and the last layer, there can be one or several so called hidden layers. This architecture is also known as multi layer perceptron (MLP). In a recurrent network, it is possible to use the output of a neuron as input to any other neuron.
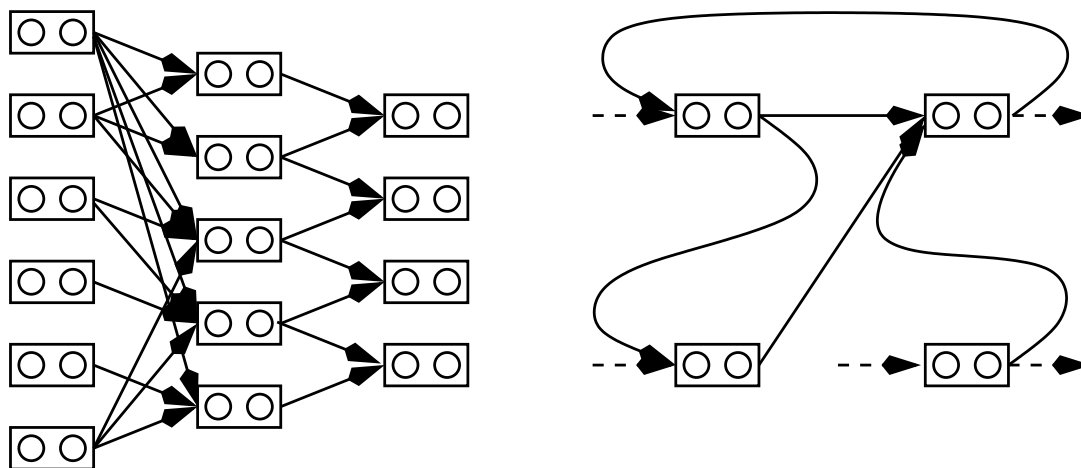
Figure E.2: A feed forward (left) and a recurrent (right) network.

E.4   Learning

Learning is used to teach the net to reproduce the desired output for a given input, e.g. to give an ascii code if a matrix pattern representing a character is put into the net. During this process, the weights w_{ij} at time t are modified:

$$w_{ij}(t) \rightarrow w_{ij}(t+1) = w_{ij}(t) + \Delta w_{ij}.$$

Several methods of weight adjustment are:

- Hebbian learning: More frequently travelled signal paths (i.e. higher stimulated ones) are given a greater weight: $\Delta w_{ij} = \eta s_i(t) s_j(t)$, where s_i, s_j are the activations of the two neurons involved.

- Delta rule learning: The weight is altered into the direction in which the prediction of the net moves toward the desired output: $\Delta w_{ij} = -\eta \partial E / \partial w_{ij}$, where E is called global error of the net, defined as below.

In delta rule learning, a set of input patterns A_p (p denoting the number of patterns available) is provided together with the desired answers T_p. The net's answer to the input is O_p. Every input pattern gives an error

$$E_p = \frac{1}{2} ||O_p - T_p||^2$$

and the global error E of the net is given by

$$E = \sum_p E_p$$

The change of the weights is then given by

$$\Delta w_{ij} = -\eta \sum_p \partial E_p / \partial w_{ij}$$
$$\partial E_p / \partial w_{ij} = \partial E_p / \partial O_p(i) \times \partial O_p(i) / \partial s_p(i) \times \partial s_p(i) / \partial w_{ij}$$

In a network with hidden layers, the output of the neurons in the hidden layer is not the desired one, thus the above expression has to be expanded:

$$\partial E_p / \partial O_p(i) = \sum_k \partial E_p / \partial O_p(k) \times \partial O_p(k) / \partial s_p(k) \times \partial s_p(k) / \partial O_p(i)$$

Here k runs over the nodes in the layer before the layer which i resides in; the errors are thus back-propagated from one layer to the previous ones.

The learning progress should be tested by dividing the data sample into a learning and a test sample. This allows one to check whether the network is being over-trained by feeding too large a set of patterns. This occurs if there are enough neurons and connections to learn the training sample by heart. In this case, the net has lost its ability to distinguish between classes of patterns. If this happens, the network performance on the learning sample will be extremely good, likewise the performance on the test sample will be poor. As a rule of thumb the number of hidden units in an FF-ANN should be chosen as low as possible. The number of training cycles should be a few times the number of weights.

E.5 Using neural nets as a means of extrapolation

It is well known that the strength of a neural net is learning the input pattern and then recognising patterns somehow related to the input. However, neural nets are also used in predicting the unlearned, e.g. tree growth or stock market indices. Here an example will be shown how a network performs in extrapolating a function of two variables. The example chosen is related to the problem posed in the analysis chapter 8, i.e. a function which falls monotonously into all directions. Such a function is given by, e.g.

$$f(x,y) = \exp\{-x^2 - y^2\}$$

which was used to check a neural networks capability in extrapolation. This special function also resembles the shape of the fakes present in the analysis using several cut parameters. As a training sample, 250 points were randomly chosen in the $x - y$ plane bordered by $x = 1$ and $y = 1$. For each random point (x, y) the corresponding function value is calculated. On top of the function value, a ten percent error into both directions was added by uniformly generating a random number between 0.9 and 1.1 and multiplying the function value with it. As a sigmoid function is involved, it is important to keep its input small, so the sigmoid will not enter its saturation. This was achieved by the following transformations:

$$x \rightarrow x_{\mathrm{NN}} = x/2.0 \tag{E.1}$$
$$y \rightarrow y_{\mathrm{NN}} = y/2.0 \tag{E.2}$$
$$f \rightarrow f_{\mathrm{NN}} = log(f)/(-2.0) \tag{E.3}$$

The 250 triplets $(x_{\mathrm{NN}}, y_{\mathrm{NN}}, f_{\mathrm{NN}})$ then were used to train three nets with architecture of 2-6-1, 2-4-1 and 2-8-1 (giving the number of input nodes, hidden layer nodes and output nodes). 500 learning cycles were applied during the weight adjustment. The result are three functions $f_{2-6-1}, f_{2-4-1}, f_{2-8-1}$ accepting two arguments x_{NN} and y_{NN} and calculating the net output f_{NN}. The general structure of these functions is the following:

$$h_k = \sigma(\sum w_{jk} i_k) \tag{E.4}$$
$$o = \sum w_k h_k \tag{E.5}$$

where i_k is the input value at the k-th input node, w_{jk} the weight assigned to the link between input node k and hidden layer node j, $\sigma(x) = 1/(1 - \exp\{-x\})$ the sigmoid function and w_k is the weight of the link between hidden layer node k and the output node o. The result is shown in figure E.3. Contour lines are drawn at levels of 0.1, $0.01, \ldots 10^{-20}$. The function itself is represented as a line, the network prediction presented as dots. In general, the prediction is very accurate. Even for the 2-4-1 network, deviations start only beyond the radius of $x^2 + y^2 > 3.5^2$ and in the other cases, slight deviations occur in the region along the x axis. Considering the comparably small area on which the
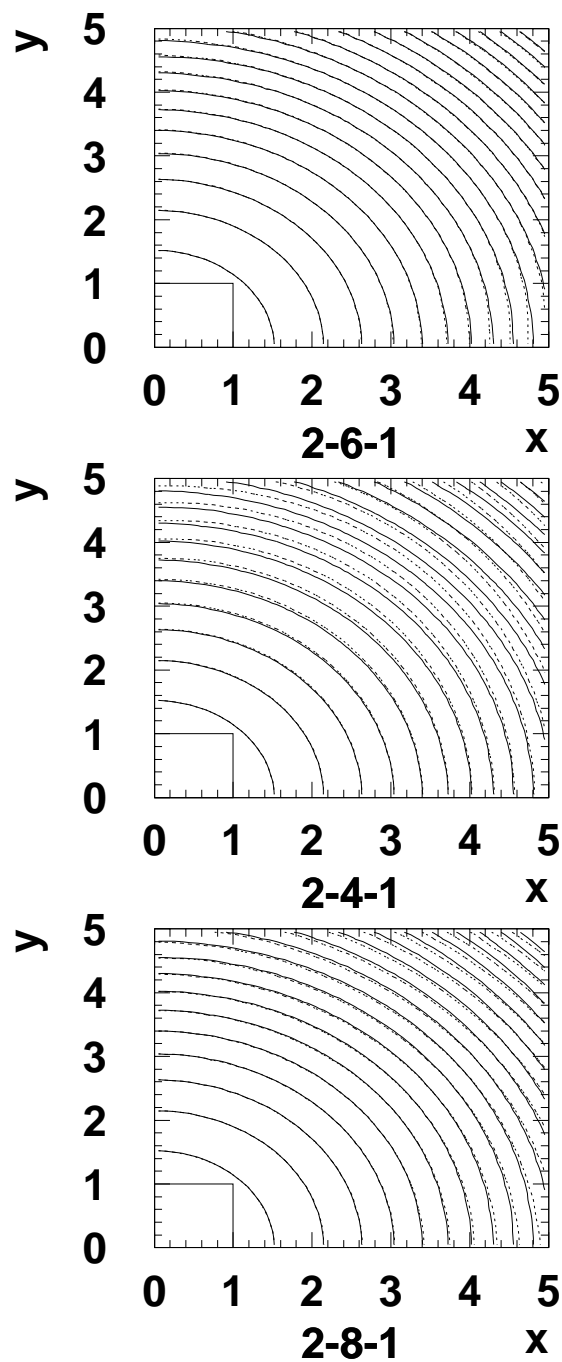
Figure E.3: Results of extrapolation using different architectures. The function values are shown as lines, the network prediction is represented as dots. Learning took place on the boxed area in the lower left corner.

net was trained, one can say that for this shape of function extrapolation using a neural net yields a meaningful result. It was found that this result is transferable to the "real life"application of background/fake estimation.

Appendix F

Programs and commands used for the processing

For the sake of completeness, the order of processing the data is given in this appendix. The whole processing was done using software from the SiEGMuND [Bouchta et al., 2000] package. Especially the programs `soff, deff, amacalib, recoos` and `munt` were used. The following table lists the order of programs and the options given.

F.1   Experimental data

```
HI reader -v -I
HI  soff (1.6.0)  -v -e 001
HI  soff (1.6.0)  -v -O 100
HI  deff (1.6.0)  -v -r28 -r32 -r34 -r39 -r40 -r47 -r50 -r57 -r62
HI -r78 -r96 -r143 -r172 -r195 -r197 -r199 -r227 -r235 -r26 -r83 -r186
HI -r215 -r264 -r81 -r82 -r83 -r84 -r85 -r86 -r188 -r195 -r227
HI -r49 -r167 -r167 -r186 -r190 -r231 -r232 -r233 -r234 -r255 -r259 -r260 -r261
HI  deff (1.6.0)  -v -P 22960:2000:2270
HI  deff (1.6.0)  -v -y a=20:1000000.
HI  amacalib (1.0 -  March 01 1999)\
 -v -T -D amanda.cal.97.data -Aa
HI  deff (1.6.0)  -v -D-19000 -y R=0.:4500
HI  deff (1.6.0)  -v -y a=0.1:1000. -y I=100:500:1 -y b=125:2000 -y i=400.
HI  recoos (2.1.0 -  March 01 1999 )\
 -v -rn -im -p w=0. -X g=f -X s=o -y I=70:500:1 -y A=1 -p t=1:5
HI  recoos (2.1.0 -  March 01 1999 )\
 -v -rn -im -p w=1. -X g=f -X s=o -y I=70:500:1 -y A=1 -p t=1:5
HI  recoos (2.1.0 -  March 01 1999 )\
 -v -rn -im -p w=0. -X g=f -X s=o -y a=1.0:1000. -y I=70:500:1 -y A=1 -p t=1:5
HI  recoos (2.1.0 -  March 01 1999 )\
```

```
 -v -rn -im -p w=1. -X g=f -X s=o -y a=1.0:1000. -y I=70:500:1 -y A=1 -p t=1:5
HI  recoos (2.1.0 -  March 01 1999 )\
 -v -rn -im -p w=2. -X g=f -X s=o -y I=70:500:1 -y A=1 -p t=1:5
HI  recoos (2.1.0 -  March 01 1999 )\
 -v -rn -im -p w=0. -X g=f -X s=o -y a=2.0:1000. -y I=70:500:1 -y A=1 -p t=1:5
```

F.2 Background Monte Carlo

```
HI  soff (1.6.0)  -v -O 100
HI  deff (1.6.0)  -v -r28 -r32 -r34 -r39 -r40 -r47 -r50 -r57 -r62
HI -r78 -r96 -r143 -r172 -r195 -r197 -r199 -r227 -r235 -r26 -r83 -r186
HI -r215 -r264 -r81 -r82 -r83 -r84 -r85 -r86 -r188 -r195 -r227
HI -r49 -r167 -r167 -r186 -r190 -r231 -r232 -r233 -r234 -r255
HI -r259 -r260 -r261
HI  deff (1.6.0)  -v -P 0:2000:2270
HI  deff (1.6.0)  -v -y a=60:1000000.
HI  deff (1.6.0)  -v -T 0:85:2500
HI  deff (1.6.0)  -v -T 86:301:4096
HI  amacalib (1.0 -  March 01 1999 )  -v -G -T -D amanda.cal.97.mc -Aa
HI  deff (1.6.0)  -v -D4000 -y R=0.:4500
HI  deff (1.6.0)  -v -y a=0.1:1000.\
-y I=100:500:1 -y b=125:2000:1:80 -y b=275:2000:81:302 -y i=400.
HI  recoos (2.1.0 -  March 01 1999 )\
 -v -rn -im -p w=0. -X g=f -X s=o -y I=70:500:1 -y A=1 -p t=1:5
HI  recoos (2.1.0 -  March 01 1999 )\
 -v -rn -im -p w=1. -X g=f -X s=o -y I=70:500:1 -y A=1 -p t=1:5
HI  recoos (2.1.0 -  March 01 1999 )\
 -v -rn -im -p w=0. -X g=f -X s=o -y a=0.5:1000. -y I=70:500:1 -y A=1 -p t=1:5
HI  recoos (2.1.0 -  March 01 1999 )\
 -v -rn -im -p w=1. -X g=f -X s=o -y a=0.5:1000. -y I=70:500:1 -y A=1 -p t=1:5
HI  recoos (2.1.0 -  March 01 1999 )\
 -v -rn -im -p w=0. -X g=f -X s=o -y a=1.0:1000. -y I=70:500:1 -y A=1 -p t=1:5
HI  recoos (2.1.0 -  March 01 1999 )\
 -v -rn -im -p w=1. -X g=f -X s=o -y a=1.0:1000. -y I=70:500:1 -y A=1 -p t=1:5
```

F.3 Monopole Monte Carlo

```
HI  soff (1.6.0)  -v -O 100
HI  deff (1.6.0)  -v -r28 -r32 -r34 -r39 -r40 -r47 -r50 -r57 -r62
HI -r78 -r96 -r143 -r172 -r195 -r197 -r199 -r227 -r235 -r26 -r83 -r186
HI -r215 -r264 -r81 -r82 -r83 -r84 -r85 -r86 -r188 -r195 -r227
```

```
HI   -r49 -r167 -r167 -r186 -r190 -r231 -r232 -r233 -r234 -r255 -r259
HI -r260 -r261
HI   deff (1.6.0)   -v -P 0:2000:2270
HI   deff (1.6.0)   -v -y a=60:1000000.
HI   deff (1.6.0)   -v -T 0:85:2500
HI   deff (1.6.0)   -v -T 86:301:4096
HI   amacalib (1.0 -  March 01 1999 )  -v -G -T -p 1.00 -D amanda.cal.97.mc_v1_3 -Aa
HI   deff (1.6.0)   -v -D4000 -y R=0.:4500
HI   deff (1.6.0)   -v -y a=0.1:1000. -y I=100:500:1 -y b=125:2000 -y i=400.
HI   recoos (2.1.0 -  March 01 1999 )\
 -v -rn -im -p w=0. -X g=f -X s=o -y I=70:500:1 -y A=1 -p t=1:5
HI   recoos (2.1.0 -  March 01 1999 )\
 -v -rn -im -p w=1. -X g=f -X s=o -y I=70:500:1 -y A=1 -p t=1:5
HI   recoos (2.1.0 -  March 01 1999 )\
 -v -rn -im -p w=0. -X g=f -X s=o -y a=0.5:1000. -y I=70:500:1 -y A=1 -p t=1:5
HI   recoos (2.1.0 -  March 01 1999 )\
 -v -rn -im -p w=1. -X g=f -X s=o -y a=0.5:1000. -y I=70:500:1 -y A=1 -p t=1:5
HI   recoos (2.1.0 -  March 01 1999 )\
 -v -rn -im -p w=0. -X g=f -X s=o -y a=1.0:1000. -y I=70:500:1 -y A=1 -p t=1:5
HI   recoos (2.1.0 -  March 01 1999 )\
 -v -rn -im -p w=1. -X g=f -X s=o -y a=1.0:1000. -y I=70:500:1 -y A=1 -p t=1:5
```

Appendix G

Overview of runs

The following table gives an overview over the available files.

Run	Day	Events	Duration/s	Rate/Hz	Run	Day	Events	Duration/s	Rate/Hz
500	095	809	1938.35	0.417	541	110	470	1268.37	0.370
501	095	2106	4803.39	0.438	542	110	15292	36262.289	0.421
502	095	1384	3164.291	0.437	543	111	259	571.841	0.452
503	095	3882	8767.25	0.442	544	111	163	396.499	0.411
504	095	18465	41638.99	0.443	545	111	2240	5496.14	0.407
505	096	543	1334.38	0.406	546	111	29	94.893	0.305
506	096	5524	12718.113	0.434	547	111	621	1488.08	0.417
507	096	49526	112570.441	0.439	548	111	333	742.95	0.448
508	097	209	458.7139	0.455	549	111	1560	3607.017	0.432
509	097	30419	69278.682	0.439	550	111	4432	10023.878	0.442
512	098	27085	62085.26	0.436	551	111	105	300.932	0.348
513	099	17481	39757.059	0.439	552	111	159	330.959	0.480
514	100	27885	63809.611	0.437	554	111	1156	3058.4	0.377
515	100	1055	2385.43	0.442	556	111	30359	68042.65	0.446
516	101	24292	57468.86	0.422	557	112	540	1425.75	0.378
517	102	3130	7606.62	0.411	560	112	37	78.7162	0.470
518	102	21777	49474.516	0.440	561	112	76	237.232	0.320
519	103	56230	122235.8	0.460	562	112	486	1054.1	0.461
520	104	729	1758.06	0.414	563	112	12975	29280.85	0.443
521	104	9473	21895.58	0.432	564	113	2453	5605.28	0.437
522	105	5980	13841.83	0.432	565	113	2969	6824.77	0.435
523	105	318	805.309	0.394	566	113	617	1443.87	0.427
524	105	2494	5930.65	0.420	567	113	3305	7650.18	0.432
525	105	257	632.968	0.406	568	113	2094	4812.34	0.435
526	105	404	910.057	0.443	569	113	732	1753.79	0.417
527	105	6523	15447.5	0.422	570	113	1072	2427.79	0.441
528	106	5716	13101.91	0.436	572	113	755	1762.289	0.428
529	106	278	734.803	0.378	573	114	1234	2883.31	0.427
530	106	10096	23640.13	0.427	574	114	739	1668.51	0.442
531	106	3118	7917.518	0.393	575	114	464	996.493	0.465
532	107	1119	2601.33	0.430	576	114	2237	5094.34	0.439
533	107	708	5414.33	0.130	577	114	2872	6613.56	0.434
535	107	23747	56528.59	0.420	578	114	2031	4615.69	0.440
536	108	1797	4311.01	0.416	579	114	8442	19716.81	0.428
537	108	8287	19376.651	0.427	580	114	698	1636.14	0.426
538	108	39212	93352.94	0.420	581	114	2021	4563.949	0.442
539	109	329	727.162	0.452	582	115	858	1988.48	0.431
540	109	24620	57759.58	0.426	583	115	8491	19773.12	0.429

Table G.1: Runs 500-583

Run	Day	Events	Duration/s	Rate/Hz		Run	Day	Events	Duration/s	Rate/Hz
584	115	3263	7585.63	0.430		657	122	1611	3992.817	0.403
585	115	418	1023.47	0.408		658	122	3636	8595.46	0.423
587	115	267	941.083	0.283		659	122	182	476.721	0.381
588	115	255	704.26	0.362		660	122	186	550.978	0.337
589	115	384	892.768	0.430		661	122	110	211.1	0.521
590	115	2150	5051.26	0.425		662	122	301	776.792	0.387
591	115	1947	4621.62	0.421		663	122	2373	5600.15	0.423
592	115	379	834.039	0.454		664	122	14706	34359.596	0.428
593	115	13180	30396.001	0.433		665	123	495	1213.25	0.407
594	116	2091	4834.48	0.432		666	123	4322	10158.18	0.425
596	116	1514	3597.177	0.420		667	123	1241	3014.86	0.411
597	116	5717	13183.083	0.433		668	123	451	1063.3	0.424
598	116	82	264.613	0.309		669	123	3124	7494.91	0.416
599	116	342	925.438	0.369		670	123	6451	15039.159	0.428
600	116	29	74.286	0.390		671	123	12514	28616.425	0.437
601	116	3312	7496.15	0.441		672	124	9590	22727.28	0.421
602	116	359	932.273	0.385		673	124	2258	5922.81	0.381
603	116	2256	5250.05	0.429		674	124	93	213.033	0.436
604	116	4059	9434.907	0.430		675	124	573	1358.37	0.421
605	117	237	529.484	0.447		676	124	1443	3506.593	0.411
606	117	5905	13962.14	0.422		677	124	27121	64321.17	0.421
607	117	457	1066.47	0.428		678	125	6	59.8767	0.100
608	117	718	1795.44	0.399		679	125	2150	4780.13	0.449
609	117	1035	2587.11	0.400		681	125	38178	88612.142	0.430
610	117	481	1168.17	0.411		682	126	809	1919.87	0.421
611	117	492	1133.78	0.433		683	126	46995	109431.89	0.429
612	117	323	841.033	0.384		684	128	33550	79013.65	0.424
613	117	760	1857.07	0.409		685	129	37397	87189.31	0.428
614	117	396	1035.28	0.382		686	130	68953	160609.543	0.429
615	117	430	1097.68	0.391		687	132	50252	111335.8763	0.451
616	117	8677	20110.49	0.431		688	133	64176	145283.16	0.441
617	118	1503	3641.355	0.412		689	135	10453	22921.41	0.456
618	118	79	248.588	0.317		690	135	28556	63941.562	0.446
619	118	272	592.377	0.459		691	136	33931	76773.436	0.441
620	118	424	1104.56	0.383		692	137	3576	8097.11	0.441
621	118	509	1213.1	0.419		696	139	1165	2605.1	0.447
622	118	849	1884.4	0.450		697	139	9649	21798.26	0.442
623	118	4618	10848.68	0.425		699	140	5487	12406.09	0.442
624	118	2148	5020.2	0.427		700	141	29435	66598.392	0.441
625	118	11203	26679.05	0.419		701	142	30305	67814.3044	0.446
626	118	4865	11122.8782	0.437		702	143	4316	10384.64	0.415
627	119	277	612.792	0.452		703	143	56462	126204.03	0.447
628	119	595	1486.58	0.400		704	144	59819	136265.872	0.438
629	119	3577	8406.6	0.425		705	146	42765	96052.311	0.445
630	119	954	2284.23	0.417		706	147	14309	32444.82	0.441
631	119	3775	9066.11	0.416		707	148	2785	6260.6	0.444
632	119	1984	4781.44	0.414		708	148	37881	87921	0.430
633	119	627	1668.32	0.375		709	149	11006	25415.466	0.433
634	119	408	1010.43	0.403		710	149	408	927.636	0.439
635	119	364	857.873	0.424		711	149	255	660.671	0.385
636	119	13862	32175.365	0.430		712	149	2028	4797.12	0.422
637	120	3615	8643.86	0.418		713	149	12890	28990.73	0.444
638	120	3996	9458.58	0.422		714	149	4879	11169.988	0.436
639	120	4141	9824.348	0.421		715	150	39605	90976.474	0.435
640	120	1916	4574.26	0.418		716	151	41511	93965.774	0.441
641	120	303	677.037	0.447		717	152	17029	40061.87	0.425
642	120	2088	5031.63	0.414		718	152	13045	30426.11	0.428
643	120	6464	15291	0.422		719	153	6495	15045.48	0.431
644	120	1808	4098.66	0.441		720	153	17555	40912.65	0.429
645	121	6445	14794.47	0.435		721	153	30591	69734.84	0.438
646	121	4518	10738.74	0.420		722	154	1102	2562.15	0.430
647	121	49	99.7335	0.491		723	155	43	262.667	0.163
648	121	85	228.414	0.372		724	155	4565	10512.53	0.434
649	121	144	450.64	0.319		725	155	49124	113654.85	0.432
650	121	3282	7609.42	0.431		726	156	17029	40064.87	0.425
651	121	255	628.708	0.405		727	157	8416	19827.97	0.424
652	121	12326	28620.79	0.430		728	157	33382	78355.163	0.426
653	122	2774	6741.624	0.411		729	158	5670	12996.23	0.436
654	122	798	1741.39	0.458		730	158	28150	65016.306	0.432
655	122	764	1740.37	0.438		731	159	40391	91868.392	0.439
656	122	683	1581.2	0.431		732	160	5572	12984.15	0.429

Table G.2: Runs 583-732

Run	Day	Events	Duration/s	Rate/Hz	Run	Day	Events	Duration/s	Rate/Hz
733	160	12213	28472.3	0.428	831	212	51644	133280.184	0.387
734	161	4810	11106.19	0.433	832	213	72342	187878.28	0.385
735	161	8107	19156.42829	0.423	833	216	6693	18780.77	0.356
736	161	9801	23439.17	0.418	834	216	106	1624.41	0.065
738	161	11266	26343.76	0.427	835	216	110	1651.74	0.066
739	162	12152	28552.04	0.425	836	216	1058	15162.61	0.069
740	162	29427	69337	0.424	837	216	33	413.501	0.079
741	163	5072	11602.46	0.437	838	216	965	13671.37	0.070
742	163	68316	161723	0.422	839	216	200	2766.92	0.072
743	165	29451	69224.401	0.425	840	216	416	5888.78	0.070
744	166	16044	37363.07	0.429	841	216	183	2085.54	0.087
745	166	29160	69106.701	0.421	843	217	203	857.678	0.236
746	167	59303	138209.505	0.429	844	217	393	3390.41	0.115
747	169	14455	33893.044	0.426	853	217	255	676.9	0.376
748	169	31176	74242.58	0.419	854	217	16435	43107.15	0.381
749	170	27384	65558.06	0.417	855	218	5723	14791.744	0.386
750	171	44620	107230.6278	0.416	856	218	15561	40228.45	0.386
751	172	19063	44996.415	0.423	858	218	17207	44700.464	0.384
752	173	11400	27226.62	0.418	859	219	37189	96844.706	0.384
753	173	14058	33641.06	0.417	860	220	228	577.927	0.394
754	173	7732	18427.21	0.419	861	220	8671	22712.869	0.381
755	174	9510	22647.21	0.419	862	220	5593	15023.35	0.372
756	174	33411	79805.7392	0.418	875	221	6033	15373.13	0.392
757	175	30099	70138.27	0.429	876	221	35410	90421.68	0.391
758	176	2729	6422.26	0.424	877	222	29368	75356.207	0.389
759	176	55687	128047.124	0.434	878	223	26379	67417.089	0.391
763	180	565	42880.48	0.013	879	224	7537	19672.86	0.383
770	189	1758	18173.75	0.096	880	224	7751	19906.132	0.389
771	189	149	5586.14	0.026	881	225	22502	56047.44	0.401
772	189	396	15165.54	0.026	882	225	52141	132892.677	0.392
773	190	7601	29918.6092	0.254	883	227	17169	43078.04	0.398
774	190	33	81.185	0.406	884	227	29054	74821.81	0.388
776	190	6803	17005.924	0.400	886	228	3887	9744.19	0.398
777	190	14927	37337.07	0.399	888	228	4468	11193.05	0.399
778	191	2882	7391.92	0.389	889	229	4617	11956.7	0.386
779	191	67698	167874.875	0.403	890	229	254	680.965	0.373
780	193	2730	7092.26	0.384	891	229	20251	51098.62	0.396
781	193	595	1523.28	0.390	892	229	3881	9786.05	0.396
782	193	23878	59832.397	0.399	893	230	62061	159014.6727	0.390
783	194	37254	93726.7895	0.397	894	231	5655	14622.45	0.386
784	195	1546	3823.45	0.404	895	232	4025	10390.42	0.387
785	195	5076	12760.39	0.397	896	232	24175	61451.87	0.393
790	195	11094	27780.13	0.399	897	233	15251	39078.133	0.390
791	195	5994	15528.74	0.385	898	233	18871	48951.915	0.385
792	196	26258	67086.0351	0.391	899	234	2993	7596.5	0.393
793	196	13090	32904.38	0.397	900	234	2207	5644.798	0.390
794	197	768	2086.29	0.368	901	234	1651	4290.89	0.384
795	197	13377	33664.59	0.397	902	234	23479	59275.69	0.396
797	197	5654	14418.921	0.392	903	235	30462	81889.95	0.371
799	198	11600	29923.955	0.387	904	236	8216	24911.09	0.329
800	198	21909	54529.77	0.401	905	236	1140	3145.43	0.362
801	199	15981	39922.2	0.400	906	236	60662	147378.195	0.411
802	199	9328	23338.71	0.399	907	238	32752	80864.845	0.405
803	200	12856	32758.83	0.392	908	239	10516	25425.398	0.413
804	200	36658	92001.346	0.398	909	239	61930	152918.78	0.404
805	201	56020	139031.552	0.402	910	241	5238	13293.05	0.394
807	203	10928	26921.795	0.405	911	241	12064	30915.76	0.390
808	203	5084	12991.66	0.391	912	242	407	1463.95	0.278
809	203	81	230.795	0.350	915	242	52	135.849	0.382
810	203	15174	37994.942	0.399	916	242	2233	5554.09	0.402
811	204	128184	320102.667	0.400	917	242	11433	28981.62	0.394
812	207	4315	10800.045	0.399	919	242	377	957.627	0.393
813	208	20328	52023.82	0.390	920	242	18308	46892.0283	0.390
814	208	4799	12095.925	0.396	921	243	10712	27318.15	0.392
815	209	644	1585.8	0.406	922	243	438	1156.89	0.378
817	209	11406	29990.07	0.380	923	243	15828	40486.73	0.390
818	209	36324	92078.608	0.394	924	244	4787	12423.21	0.385
819	210	26397	66646.192	0.396	925	244	15544	39981.136	0.388
820	211	16	70.1977	0.227	926	244	11442	29127.77	0.392
829	211	16532	41820.03	0.395	927	245	16032	40668.23	0.394
830	212	641	1821.34	0.351	928	245	5273	13465.88	0.391

Table G.3: Runs 733-928

Run	Day	Events	Duration/s	Rate/Hz	Run	Day	Events	Duration/s	Rate/Hz
930	245	15862	40485.804	0.391	1005	272	32466	79347.096	0.409
931	246	31841	81553.529	0.390	1006	273	17017	41142.79	0.413
932	247	431	1107.59	0.389	1007	273	9639	23226.16	0.415
933	247	5256	13130.23	0.400	1008	273	7574	18009.4	0.420
934	247	3040	7681.37	0.395	1009	274	9886	24072.98	0.410
935	247	7796	19444.75	0.400	1010	274	12	34.5014	0.347
936	247	7693	19919.36	0.386	1011	274	33	108.007	0.305
937	248	12654	32100.52	0.394	1012	274	467	1093.3	0.427
938	248	26	77.9781	0.333	1013	274	5140	12359.92	0.415
939	248	2323	5985.58	0.388	1014	274	71	194.017	0.365
940	248	19	54.4843	0.348	1015	274	6954	16708.558	0.416
941	248	232	593.443	0.390	1016	274	7746	19254.162	0.402
942	248	5003	12734.26	0.392	1017	275	12132	29149.81	0.416
943	248	12158	31024.376	0.391	1018	275	17735	43463.81	0.408
944	249	8800	22719.04	0.387	1019	276	2123	5188.84	0.409
945	249	24486	63023.532	0.388	1020	276	1413	3551.253	0.397
946	250	95404	244493.751	0.390	1021	276	328	756.35	0.433
947	253	24373	61812.39	0.394	1022	276	1071	2473.64	0.432
949	253	20830	51990.1	0.400	1023	276	27	53.9264	0.500
950	254	10662	26807.57	0.397	1025	276	15753	37004.58	0.425
951	254	181	571.913	0.316	1026	276	503	1221.03	0.411
952	255	13332	38177.26	0.349	1028	276	13594	31967.54	0.425
953	255	26292	65994.58	0.398	1029	277	801	1882.47	0.425
954	256	16188	39090.627	0.414	1031	277	15465	36611.85	0.422
955	256	56923	145127.55	0.392	1032	277	7001	16451.1509	0.425
956	258	31661	77756.053	0.407	1033	277	8731	20802.729	0.419
957	259	5530	14004.92	0.394	1034	278	27822	66032.419	0.421
958	259	281	686.294	0.409	1035	278	2758	6685.07	0.412
959	259	2770	7035.889	0.393	1037	279	13485	33299.337	0.404
960	260	32718	82376.897	0.397	1038	279	7006	19614.554	0.357
961	261	471	1266.05	0.372	1039	279	12522	30067.717	0.416
962	261	961	2378.46	0.404	1041	280	28836	68159.509	0.423
963	261	2084	5046.05	0.412	1042	281	18498	44086.36554	0.419
964	261	17443	44241.233	0.394	1043	281	8112	19381.428	0.418
965	261	1697	4326.81	0.392	1044	282	26123	61232.32	0.426
966	261	3426	16057.9	0.213	1045	282	189	565.053	0.334
967	262	993	13312.34	0.074	1046	282	13058	30996.738	0.421
968	262	130	1919.64	0.067	1047	283	24855	57565.337	0.431
969	262	62	851.55	0.072	1048	284	4381	10297.4	0.425
971	262	18	383.391	0.046	1049	284	1235	2983.917	0.413
972	262	145	1823.14	0.079	1050	284	3303	7763.65	0.425
973	262	987	13104.58	0.075	1051	284	16575	38994.595	0.425
974	262	18	172.625	0.104	1052	284	4932	11378.057	0.433
975	262	547	7111.55	0.076	1053	285	3	1.26199	2.377
976	262	793	10841.864	0.073	1054	285	78	167.134	0.466
977	262	215	2467.23	0.087	1055	285	7116	16608.289	0.428
978	262	48	686.218	0.069	1056	285	11251	26229.14	0.428
979	262	91	1283.92	0.070	1057	285	363	788.579	0.460
980	262	355	4673.342	0.075	1058	285	25067	59268.85	0.422
981	263	56	708.98	0.078	1059	286	809	1858.71	0.435
982	263	569	7892.56	0.072	1060	286	3	5321.7	0.000
983	263	201	2852.31	0.070	1061	286	28343	66389.245	0.426
985	263	2	1.08225	1.848	1062	287	14158	32705.79	0.432
986	263	147	1805.77	0.081	1063	287	12624	29024.47	0.434
987	263	762	9624.18	0.079	1064	287	33951	79343.17	0.427
988	263	168	2247.55	0.074	1065	289	1010	2542.31	0.397
989	263	1239	16721.74	0.074	1066	289	9720	22708.839	0.428
990	263	35	365.871	0.095	1067	289	47247	107856.751	0.438
991	263	3940	52798.62	0.074	1068	290	42586	97100.866	0.438
992	264	808	10794.04	0.074	1069	291	8104	18362.734	0.441
993	264	5314	71352.161	0.074	1070	292	4790	10956.308	0.437
994	265	4753	62511.65	0.076	1071	292	18683	42182.71	0.442
995	266	5455	73370.752	0.074	1072	292	11172	25377.35	0.440
996	267	12895	170082.633	0.075	1073	293	26902	61416.2612	0.438
997	269	2146	28184.7773	0.076	1074	293	15411	35829.26	0.430
998	269	4766	61847.608	0.077	1075	294	8598	19874.17	0.432
999	270	4047	54261.8	0.074	1076	294	10892	25112.7	0.433
1000	270	474	6644.715	0.071	1078	294	9843	23300.08	0.422
1001	271	346	4310.3	0.080	1079	295	2538	5805.849	0.437
1003	271	23076	55893.146	0.412	1080	295	21551	49239.491	0.437
1004	271	297	764.435	0.388	1081	295	2729	7011.082	0.389

Table G.4: Runs 928-1081

Run	Day	Events	Duration/s	Rate/Hz
1082	296	453	5370.7	0.084
1083	296	20547	239549.992	0.085
1086	299	24590	56887.869	0.432
1087	299	164	3182.99	0.051
1088	299	6346	14511.35	0.437
1089	300	8713	19790.06	0.440
1090	300	2852	6439.17	0.442
1091	300	24676	55647.07	0.443
1092	301	22375	52488.21	0.426
1093	301	12879	29702.368	0.433
1094	302	52484	119738.3	0.438
1095	303	46874	107997.4681	0.434
1096	304	32771	73854.59	0.443
1097	306	10115	23020.79	0.439
1098	306	788	1607.68	0.490
1099	306	12687	28242.63	0.449
1100	306	48934	108857.5680	0.449
1101	308	4339	9670.89	0.448
1102	308	5599	12347.93	0.453
1103	308	22276	49228.97	0.452
1104	308	45378	98468.03	0.460
1110	311	243	476.603	0.509
1111	311	75525	162625.427	0.464
1112	313	2042	4731.67	0.431
1113	313	7771	16346.82	0.475
1115	314	25414	54741.34	0.464
1116	314	78777	250398.429	0.314
1117	317	45272	96346.781	0.469
1118	319	2884	6178.522	0.466
1119	319	586	1226.23	0.477
1120	319	2523	5264.3	0.479

Table G.5: Runs 1082-1119

Bibliography

[EB1, 1991] (1991). *Encyclopædia Britannica*, volume 18, page 188. Encyclopædia Britannica Inc., Chicago, 15th edition.

[Abbes et al., 1996] Abbes, M. et al. (1996). *Nucl. Instr. Meth.*, 374:164.

[Abbott et al., 1998] Abbott, B. et al. (1998). A Search for heavy Pointlike Dirac Monopoles. Fermilab-Pub-98/095-E.

[Ahlen et al., 1993] Ahlen, S. P. et al. (1993). *Nucl. Instr. Meth.*, 324:337.

[Ambrosio et al., 1997] Ambrosio, M. et al. (1997). *Astrop. Phys.*, 7:109–124.

[Amendolia, 1993] Amendolia, S. R. (1993). Neural networks. In *Proc. CERN School of Computing, L'Aquila, Italy*, pages 1–35.

[Anchorduqui et al., 2000] Anchorduqui, L. A., McCauley, T. P., Reucroft, S., and Swain, J. (2000). Echoes of the fifth dimension? hep-ph/0009319.

[Ashton, 1972] Ashton, W. (1972). *The Logit Transformation*. Charles Griffin&Co.

[Balkanov et al., 1999a] Balkanov, V. A. et al. (1999a). Search for relativistic monopoles with the Baikal neutrino telescope. In *Proc. 26th ICRC, Salt Lake City, USA*, volume 2, page 340.

[Balkanov et al., 1999b] Balkanov, V. A. et al. (1999b). The Lake Baikal Neutrino Telescope NT-200: First year of operation. In *Proc. 26th ICRC, Salt Lake City, USA*, volume 2, pages 217–220.

[Barrett et al., 1952] Barrett, K. et al. (1952). *Rev. Mod. Phys*, 2:133.

[Barton, 1997] Barton, C. E. (1997). International Geomagnetic Reference Field: The Seventh Generation. *J. Geomag. Geoelectr.*, 49:123–148.

[Bauleo et al., 2000] Bauleo, P., Goobar, A., and Martino, J. R. (2000). UV-enhancement of Photomultiplier response; a study of wavelength shifters for the AMANDA/IceCube detector. *Nucl. Instr. Meth. A*, 443:136–147.

[Beck, 1996] Beck, R. (1996). *Ann. Rev. Astron.& Astrophys.*, 34:155.

[Belolaptikov, 1994] Belolaptikov, I. A. (1994). In *Proc. 24th ICRC, Rome, Italy*, volume 1, page 841.

[Bermon et al., 1990] Bermon, S. et al. (1990). *Phys. Rev. Lett.*, 64:839.

[Biron, 1999] Biron, A. (1999). The Zeuthen B-10 MC mass production and mass reconstruction. http://www.ifh.de/~biron/mc/.

[Biron et al., 1997] Biron, A. et al. (1997). Upgrade of AMANDA-B towards AMANDA-II. DESY PRC.

[Biron et al., 1999] Biron, A. et al. (1999). First and Second Level Reconstruction of 97 Muon Data. AMANDA Internal Report 19990701.

[Boerner, 1988] Boerner, G. (1988). *The early universe.* Springer Verlag.

[Bottai, 1999] Bottai, S. (1999). Nestor: a Status Report. In *Proc. 26th ICRC, Salt Lake City, USA*, volume 2, pages 456–459.

[Bouchta, 1999] Bouchta, A. (1999). Seasonal variation of the muon flux seen by AMANDA. In *Proc. 26th ICRC, Salt Lake City, USA*, volume 2, pages 108–111.

[Bouchta et al., 2000] Bouchta, A. et al. (2000). SiEGMuND homepage. http://www.ifh.de/nuastro/software/siegmund/siegmund.html.

[Boziev et al., 1989] Boziev, S. N. et al. (1989). Preprint P-0630, INR.

[Bradner and Isbell, 1959] Bradner, H. and Isbell, W. M. (1959). *Phys. Rev.*, 114:603.

[Braunschweig et al., 1988] Braunschweig, W. et al. (1988). *Z. Physik C*, 38:543.

[Buckland et al., 1990] Buckland, K. N., Masek, G. E., Vernon, W., Knapp, L. M., and Stronski, J. P. (1990). *Phys. Rev. D*, 41(9):2726.

[Burrows et al., 1992] Burrows, A., Klein, D., and Gandhi, R. (1992). The future of supernova neutrino detection. *Phys. Rev. D*, 45(10):3361.

[Cabrera, 1982] Cabrera, B. (1982). First results from a Superconductive Detector for Moving Magnetic Monopoles. *Phys. Rev. Lett.*, 48(20):1378–1381.

[Callan, 1982] Callan, C. (1982). *Phys. Rev. D*, 25:2141.

[Carrigan Jr. et al., 1974] Carrigan Jr., R. A., Nezrick, F. A., and Strauss, B. P. (1974). *Phys. Rev.*, D(10):3867.

[Cei et al., 1998] Cei, F. et al. (1998). Search for Rare Particles with the MACRO Detector. hep-ex/9810012.

[Dalberg, 1999] Dalberg, E. (1999). *A Search for Neutralino Dark Matter with the AMANDA-B10 Detector*. PhD thesis, Stockholm University, Department of Physics.

[DeLotto et al., 1964] DeLotto, I., Manfredi, P. F., and Principi, P. (1964). *Energia Nucleare (Milano)*, 11.

[Derkaoui et al., 1998] Derkaoui, J. et al. (1998). Energy losses of magnetic monopoles and of dyons in the earth. *Astropart. Phys.*, 9:173–183.

[Dickinson et al., 2000] Dickinson, J. E. et al. (2000). *Nucl. Instr. Meth. A*, 440:95.

[Dirac, 1931] Dirac, P. A. M. (1931). Quantised Singularities in the Electromagnetic Field. *Proc. Roy. Soc. A*, 133:60–72.

[Djilkibaev and Spiering, 1998] Djilkibaev, J. and Spiering, C. (1998). Search for magnetic monopoles with the Baikal Underwater Neutrino Telescope.

[Domogatsky and Zheleznykh, 1969] Domogatsky, G. V. and Zheleznykh, I. M. (1969). *Yad. Fiz.*, 10:1238.

[Drell et al., 1983] Drell, S., Kroll, N., Mueller, M., Parke, S., and .Ruderman, M. (1983). *Phys. Rev. Lett.*, 50.

[Elbert and Sommers, 1995] Elbert, J. W. and Sommers, P. (1995). *Astrophys. J.*, 441:151.

[Enßlin et al., 1997] Enßlin, T. A. et al. (1997). *Astrophys. J.*, 477:560–567.

[Fidecaro et al., 1961] Fidecaro, M., Finocchiaro, G., and Giacomelli, G. (1961). *Nuovo Cimento*, 22:657.

[Gaisser et al., 1993] Gaisser, T. K. et al. (1993). *Phy. Rev. D*, 47:1919.

[Gaisser et al., 1995] Gaisser, T. K., Halzen, F., and Stanev, T. (1995). Particle astrophysics with high energy neutrinos. *Phys. Rep.*, 258:175–236.

[Gandhi et al., 1991] Gandhi, R., Quigg, C., Reno, M. H., and Sarcevic, I. (1991). *Phys. Rev. Lett.*, 66:2697.

[Gaug et al., 2000] Gaug, M., Niessen, P., and Wiebusch, C. H. V. (2000). Investigations on Smoothness observables. AMANDA internal report 20000201.

[Greisen, 1966] Greisen, K. (1966). *Phys. Rev. Lett.*, 16:748.

[Grieder et al., 1990] Grieder, P. K. F. et al. (1990). The DUMAND stage II detector and its capabilities. In *Proc. 23rd ICRC, Adelaide, Australia*, volume 4, pages 357–360.

[Groom, 1986] Groom, D. (1986). *Phys. Rep.*, 140:323.

[Gustafsson et al., 1996] Gustafsson, L., Marcinievski, P., and Zernov, A. (1996). MADD – a fast multiplicity trigger system. *Nucl. Inst. and Meth. A*, 379:335–340.

[Guth and Weinberg, 1983] Guth, A. H. and Weinberg, E. (1983). *Nucl. Phys. B*, 212:321.

[Halzen, 1999] Halzen, F. (1999). From the First Neutrino Telescope, the Antarctic Muon and Neutrino Detector Array AMANDA, to the IceCube Observatory. In *Proc. 26th ICRC, Salt Lake City, USA*, volume 2, pages 428–431.

[Halzen and Zas, 1997] Halzen, F. and Zas, E. (1997). Neutrino fluxes from active galaxies: A model independent estimate. astro-ph/9702193.

[Hampel et al., 1996] Hampel, W. et al. (1996). *Phys. Lett. B*, 388:384–396.

[Hanson, 2000] Hanson, K. (2000). Crosstalk in 1997 AMANDA raw data. AMANDA internal report 20000801.

[He and Price, 1998] He, Y. D. and Price, P. B. (1998). *J. Geophys. Res.*, 103:17041.

[Heck et al., 1998] Heck, D. et al. (1998). CORSIKA: A Monte Carlo Code to Simulate Extensive Air Showers. Technical Report 6019, Forschungszentrum Karlsruhe.

[Hubbard, 1999] Hubbard, J. (1999). Status of the Antares Project. In *Proc. 26th ICRC, Salt Lake City, USA*, volume 2, pages 436–439.

[Hundertmark, 1999] Hundertmark, S. (1999). *Simulation und Analyse von Myonereignissen im Amanda-B4-Neutrinoteleskop*. PhD thesis, Humboldt-Universität zu Berlin, Mathematisch-Naturwissenschaftliche Fakultät.

[Hung, 1994] Hung, J. T. (1994). *Nucl. Phys. B (Proc. Suppl.)*, 35:261–263.

[Jackson, 1975] Jackson, J. D. (1975). *Classical Electrodynamics*. John Wiley & Sons, Mew York, London, Sidney, Toronto, second edition.

[Jacob, 1998] Jacob, T. (1998). Analysis of the noise- and trigger-rates 1997. Summer-student writeup.

[Karle, 1998a] Karle, A. (1998a). HOLE ICE - A bubbly simulation . http://alizarin.physics.wisc.edu/karle/hole-ice.

[Karle, 1998b] Karle, A. (1998b). Monte Carlo Simulation of photon transport and detection in deep ice: muons and cascades. In Spiering, C., editor, *Simulation and Analysis Methods for Large Neutrino Telescopes*, page 174. DESY, Zeuthen, Germany, July 6-9 1998. DESY-PROC-1999-01.

[Kazama et al., 1977] Kazama, Y., Yang, C. N., and Goldhaber, A. S. (1977). *Phys. Rev. D.*, (15):2287.

[Kellermann and Pauliny-Toth, 1981] Kellermann, K. I. and Pauliny-Toth, I. I. K. (1981). *Ann. Rev. A&A*, 19:373.

[Kephart and Weiler, 1996] Kephart, T. W. and Weiler, T. J. (1996). Magnetic Monopoles as the highest energy cosmic ray primaries. *Astropart. Phys.*, 4:271–279.

[Kibble, 1980] Kibble, T. W. (1980). *Phys. Rept.*, 67:180.

[Kinoshota et al., 1989] Kinoshota, K. et al. (1989). *Phys. Lett. B*, 228:543.

[Kinoshota et al., 1992] Kinoshota, K. et al. (1992). *Phys. Rev. D*, 46:R881.

[Kolb and Turner, 1990] Kolb, E. W. and Turner, M. S. (1990). *The Early Universe, Frontiers in Physics*, volume 69. Addison Wesley.

[Kolokolov et al., 1999] Kolokolov, I. et al. (1999). Interactions of a massive slow magnetic Monopole with matter. hep-ph/9809420.

[Kowalski, 1999] Kowalski, M. (1999). On the Reconstruction of Cascade like Events in the AMANDA Detector. AMANDA internal report 19990701.

[Kronberg et al., 1981] Kronberg, P. P. et al. (1981). *Astrophys. J.*, 246:751.

[Langacker and Pi, 1980] Langacker, P. and Pi, S.-Y. (1980). *Phys. Rev. Lett.*, 45:1.

[Lazarides et al., 1987] Lazarides, G. et al. (1987). *Phys. Rev. Lett.*, 58:1707.

[Lazarides and Shafi, 1983] Lazarides, G. and Shafi, Q. (1983). *Phys. Lett. B*, 124:26.

[Lazarides and Shafi, 1984] Lazarides, G. and Shafi, Q. (1984). *Phys. Lett. B*, 148:35.

[Leuthold and Wissing, 2000] Leuthold, M. and Wissing, H. (2000). Oral communication.

[Lowder et al., 2000] Lowder, D., Richter, S., Ley, C., Jacobsen, J., et al. (2000). AMANDA optical module/channel database. http://area51.berkeley.edu/~lowder/amanda/omdb/.

[Lowder, 1997] Lowder, D. M. (1997). The AMANDA Neutrino Telescope: Design, Construction, and Performance. In *Proceedings of the A.S.P. Symposium Astrophysics from Antarctica*.

[McLoone et al., 1998] McLoone, S. et al. (1998). A Hybrid Linear / Nonlinear Training Algorithm for Feedforward Neural Networks. *IEEE Transactions on Neural Networks*, 9(4):669.

[Mihalyi et al., 2000] Mihalyi, A., Cowen, D. F., and .Taboada, I. (2000). AMANDA ADC Response to Multiple Photoelectrons. AMANDA internal report 20000601.

[Musset et al., 1983] Musset, P., Price, M., and Lohrmann, E. (1983). *Phys. Lett. B*, 128:333.

[Niessen, 1998] Niessen, P. (1998). Simulated Bubbles and Their Effect on some Observables in AMANDA-B4. AMANDA internal report 19981101.

[Öhrmalm, 1997] Öhrmalm, J. (1997). Effects of the magnetic field on the AMANDA optical module and pulse-height and time-over-threshold distributions of the PMT signal for 1pe, 2pe and 3pe events. Technical Report TSL/ISV-97-0174, Uppsala University.

[Orito et al., 1991] Orito, S. et al. (1991). *Phys. Rev. Lett.*, 66:1951.

[Pinfold et al., 1993] Pinfold, J. L. et al. (1993). *Phys. Lett. B*, 316:407.

[Polyakov, 1974] Polyakov, A. M. (1974). Spektr tschastiz w kwantowoi teorii polya. *Pisma Zhournal ETP*, 20:430–433.

[Preskill, 1979] Preskill, J. P. (1979). Cosmological Production of Superheavy Magnetic Monopoles. *Phys. Rev. Lett.*, 43(19):1365–1368.

[Press et al., 1992] Press, W. H. et al. (1992). *Numerical Recipes in FORTRAN*. Cambridge University Press, Cambridge.

[Price, 1984] Price, P. B. (1984). *Phys. Lett. B*, 140:112.

[Price et al., 1987] Price, P. B., Guoxiao, R., and Kinoshita, K. (1987). *Phys. Rev. Lett.*, 59:2523.

[Purcell et al., 1963] Purcell, E. M. et al. (1963). *Phys. Rev*, 129:2326.

[Rubakov, 1982] Rubakov, V. A. (1982). *Nucl. Phys. B*, 203:311.

[Ryu et al., 1998] Ryu, D., Kang, H., and Biermann, P. L. (1998). astro-ph/9803275.

[Sigl et al., 1994] Sigl, G., Schramm, D. N., and Bhattacharjee, P. (1994). *Astropart. Phys.*, 2:401.

[Smith et al., 1989] Smith, N. J. T. et al. (1989). *Nucl. Instr. Meth. A*, 278:622.

[Stenger, 1990] Stenger, V. (1990). Track fitting for the DUMAND Octogon. Technical Report HDC-1-90, University of Hawaii.

[Teich and Cantor, 1975] Teich, M. C. and Cantor, B. I. (1975). *Journ. Opt. Soc. Am.*, 65(7):786–791.

[Thollander,] Thollander, L. Oral communication.

[Thollander, 1998] Thollander, L. (1998). Oral communication.

['tHooft, 1974] 'tHooft, G. (1974). Magnetic Monopoles in Unified Gauge Theories. *Nucl. Phys. B*, 79:276–284.

[Thron et al., 1989] Thron, J. et al. (1989). *Nucl. Instr. Meth. A*, 283:642.

[Tompkins, 1965] Tompkins, D. R. (1965). Total Energy Loss and Cherenkov Emission from Monopoles. *Phys. Rev. B*, 138(1):248–250.

[Trofimenko, 1992] Trofimenko, I. I. (1992). Preprint INR Russ. Ac. Sci. 765/92.

[Turner et al., 1982] Turner, M. S., Parker, E. N., and Bogdan, T. J. (1982). Magnetic monopoles and the survival of the galactic magnetic fields. *Phys. Rev. D*, 26(6):1296–1305.

[Weiler and Kephart, 1996] Weiler, T. J. and Kephart, T. W. (1996). Magnetic Monopoles as the highest energy cosmic ray primaries. *Nucl. Phys. B (Proc. Suppl.)*, 51:218.

[Wiebusch, 1996] Wiebusch, C. H. V. (1996). Preliminary results on the angular response of the AMANDA optical module. AMANDA internal report 19960301.

[Wiebusch, 1998a] Wiebusch, C. H. V. (1998a). Proceedings of the DESY Zeuthen AMANDA collaboration meeting.

[Wiebusch, 1998b] Wiebusch, C. H. V. (1998b). Muon reconstruction with AMANDA. In Spiering, C., editor, *Simulation and Analysis Methods for Large Neutrino Telescopes*, page 302. DESY, Zeuthen, Germany, July 6-9 1998. DESY-PROC-1999-01.

[Wilkes, 1994] Wilkes, R. J. (1994). DUMAND and AMANDA: high-ergy neutrino astrophysics. In *Proc. 22nd Annual SLAC Summer Institute on Praticle Physics: Particle Physics, Astrophysics and Cosmology*.

[Woschnagg,] Woschnagg, K. Hole Ice Studies with YAG Data/MC . http://alizarin.physics.wisc.edu/karle/hole-ice/yak/.

[Woschnagg, 1999] Woschnagg, K. (1999). Optical Properties of South Pole Ice at Depths from 140 to 2300 Meters. In *Proc. 26th ICRC, Salt Lake City, USA*, volume 2, pages 200–203.

[Young, 1998] Young, S. (1998). Hole and Bulk Ice Analysis using AB Coincidence Data. http://www.ps.uci.edu:80/ youngs/amanda/ab_analysis.html.

[Youssef, 1998] Youssef, S. (1998). Monte Carlo Techniques. *The European Physical Journal C*, 3(1-4):178–179.

[Zatsepin and Kuzmin, 1966] Zatsepin, G. T. and Kuzmin, V. A. (1966). *Pisma Zhournal ETP*, 4:114.

Acknowledgements

Lebenslauf

Persönliche Daten

Name: Peter Nießen
Geburt: 09. 08. 1968 in Neuss
Staatsangehörigkeit: deutsch
Familienstand: ledig
Adresse: Karl-Marx-Platz 15, 12043 Berlin
Telefonnummer: 030/681 77 02, 033762/77-516
e–mail: niessen@ifh.de

Schulausbildung

1975–1979   Görres–Grundschule Neuss
1979–1988   städt. Quirinus–Gymnasium Neuss
7. Juni 1988   Allgemeine Hochschulreife, Endnote „gut"

Praktikum

September 1988 – Oktober 1988   Grundpraktikum für Studenten des Maschinenwesens
                                 JI Case Landmaschinen GmbH, Neuss

Zivildienst

November 1988 – Juni 1990   Malteser–Hilfsdienst Neuss

Universitätsausbildung

Oktober 1990   Rheinisch-Westfälische Technische Hochschule
                                 Aachen im Studiengang Physik

21. September 1992	Vordiplom in Physik, Note „gut", Vertiefung der Richtung Hochenergiephysik
Oktober 1995 – Oktober 1996	Diplomarbeit am III. Physikalischen Institut, Prof. Dr. G. Flügge, „Bau und Test eines Mikrostreifengasdetektors" Endnote „sehr gut"
Juni 1996	Arbeit am Europäischen Labor für Teilchenphysik (CERN)
15.–28. September 1996	Herbstschule 8th Annual graduate school of particle physics Joint Belgian–Dutch–German school in Rolduc, Niederlande

Tätigkeiten als studentische Hilfskraft

SS 1993–WS 1993/94	Betreuung von Studierenden der Mathematik, Physik, Informatik und Betriebswirtschaftslehre im Fach Lineare Algebra
SS 1994	Betreuung von Studierenden des Maschinenwesens im Physikalischen Praktikum am I. Physikalischen Institut
SS 1995	Übungsgruppenleiter in Experimentalphysik IV Atome, Moleküle, Kerne am I. Physikalischen Institut
WS 1995/96	Übungsgruppenleiter in Theor. Mechanik am Lehrstuhl C für Theoretische Physik
SS 1996	Übungsgruppenleiter in Experimentalphysik IV Atome, Moleküle, Kerne am III. Physikalischen Institut

Promotion

130

Januar 1997 – Februar 2001	Promotion am DESY Zeuthen, Dr. C. Spiering, „Search for relativistic magnetic monopoles with the AMANDA detector"
22. Januar 1998 – 14. Februar 1998	Softwarearbeit auf der Amundsen-Scott Südpolstation

Tagungen, Konferenzen

DPG Frühjahrstagung 1998 in München	Vortrag über das Datennahmesystem des Amanda Detektors
15. – 23. 7. 1998	International School of Cosmic Ray Astrophysics Erice, Italien
DPG Frühjahrstagung 1999 in Heidelberg	Vortrag über die Suche nach magnetischen Monopolen mit dem Amanda Detektor
17. – 21. 5. 1999	Sixth Topical Seminar on Neutrino and Astro Particle Physics, San Miniato, Italien

Veröffentlichungen

Beam test results of the CMS Tracker Prototype, CERN CMS TN 96-020

Upgrade of AMANDA-B towards AMANDA-II, DESY PRC 97/05

Simulated bubbles and their effect one some observables in AMANDA-B4,
AMANDA internal report

Search for relativistic monopoles with the AMANDA detector
Proc. of the 26th ICRC, Salt Lake City, USA 1999

Zusätzliche Kenntnisse

UNIX (HP-UX, Linux) und die Anwendungen PAW, Maple, LaTeX,
Mitarbeit bei der Photonpropagations- und Detektorsimulation von AMANDA

Erstellen von shell-scripts, sed, awk
Programmiersprachen: Fortran, C, C++
perl Grundkenntnisse
Neuronale Netze
CAMAC–Auslesesystem

Englisch fließend in Wort und Schrift
Französischgrundkenntnisse

Sonstige Tätigkeiten und Interessen

Mehrere Semester Wohnheim Flursprecher in Aachen
Leitung der Wohnheims Foto–AG

Mitglied im „Amadeus-Chor", Berlin
Betreuung der Internetseite `http://www.amadeus-chor.de`

Berlin, den 25. April 2001
Peter Nießen

Selbständigkeitserklärung

Hiermit erkläre ich, die Dissertation selbstständig und ohne unerlaubte fremde Hilfe angefertigt zu haben. Ich habe mich anderwärts nicht um einen Doktorgrad beworben und besitze einen entsprechenden Doktorgrad nicht. Ich erkläre die Kenntnisnahme der dem Verfahren zugrunde liegenden Promotionsordnung der Mathematisch-Naturwissenschaftlichen Fakultät I der Humboldt-Universität zu Berlin.
  Peter Nießen

24. November 2000